SCIENTIA
BRUNEIANA

This journal consists of papers prepared by staff of Universiti Brunei Darussalam and peer reviewed by local and international referees.

SCIENTIA BRUNEIANA
Vol. 16

Greetings from the Dean of UBD's Faculty of Science.

I am pleased to introduce our first issue for 2017 which again highlight some important and significant findings made by our own researchers in field of natural and applied sciences. This journal is unique as it does not focus solely on fundamental sciences but also applied sciences thus promoting inter- and multi-disciplinarity.

The Faculty has a strong record of ground-breaking research in the biological, physical and mathematical sciences. The papers appearing in this issue demonstrate the ongoing commitment of our research staff to innovative science that contributes to the national interest as well as broadening the knowledge base of the global scientific community. The many outstanding examples of collaborative research showcased here highlight the recognition that quality Bruneian research is now receiving across the world.

I am also pleased to note contribution from leading scientists in this issue. In our pursuit of international excellence and global recognition, we are certain this trend will continue.

I would like to thank my colleagues at Faculty of Science particularly authors, associate and subject editors for their continuous support.

Yours Sincerely
Abby Tan Chee Hong
Chief Editor
Scientia Bruneiana

SCIENTIA BRUNEIANA

A journal of science and science-related matters published twice a year by the Faculty of Science, Universiti Brunei Darussalam. Contributions are welcome in any area of science, mathematics, medicine or technology. Authors are invited to submit manuscripts to the editor or any other member of the Editorial Board. Further information including instructions for authors can be found in the notes to contributors section (final four pages at the end).

EDITORIAL BOARD

SCIENTIA BRUNEIANA

Publication Ethics Policy

The Editorial Board of *Scientia Bruneiana* is committed to implementing and maintaining the publication standards of a high-quality peer-reviewed scientific journal.

Each manuscript submitted to *Scientia Bruneiana* is examined by a referee with recognised expertise in the manuscript's subject area, and all communications between the referee and the author(s) pass must first through the Editorial Board, so that the identity of the referee remains confidential.

No one will be appointed as the referee of a manuscript if he or she is known to have a potentially compromising relationship with one or more of the authors of the manuscript, as for example in being related through blood or marriage to an author, or in being the research supervisor or research student of an author.

The Editorial Board of *Scientia Bruneiana* makes every effort to ensure that each paper published in the journal is free of plagiarism, redundant or recycled text, and fabricated or misrepresented data. Where possible, plagiarism detection software will be used to check for plagiarised or recycled text.

Provided that a manuscript is free of the ethical lapses described in the previous paragraph, the decision to publish it in *Scientia Bruneiana* is based entirely on its scientific or academic merit, as judged by the referee. The referee's assessment of the merit of the manuscript is final. While a full statement of the reasons behind the referee's decision will be passed on to the author(s), no appeals from the author(s) will be entertained.

Under no circumstances will the referee of a paper published in *Scientia Bruneiana* be credited as one of the authors of the paper, and other papers that have been authored or co-authored by the referee will be admitted to the paper's list of references only after an independent third party with expertise in the area has been consulted to ensure that the citation is of central relevance to the paper.

If a member of the Editorial Board of *Scientia Bruneiana* is listed as an author of a manuscript submitted to *Scientia Bruneiana*, that Board member will play no part whatsoever in the processing of the manuscript.

Where necessary, any corrections or retractions of papers previously published in *Scientia Bruneiana* will be printed in the earliest possible edition of the journal, once the need for a correction or retraction has been drawn to the attention of the Editorial Board.

SCIENTIA BRUNEIANA VOL. 16

2017

Table of Contents   **Page Numbers**

Perovskite solar cells

Piyasiri Ekanayake[1]*, Lim Chee Ming[2], Toby Meyer[3] and Mohammad Khaja Nazeeruddin[4]

[1]Physical and Geological Sciences, Faculty of Science, Universiti Brunei Darussalam, Jalan Tungku Link, Gadong, BE 1410, Brunei Darussalam
[2]Centre for Advanced Materials and Energy Sciences, Universiti Brunei Darussalam, Jalan Tungku Link, Gadong BE 1410, Brunei Darussalam
[3]Solaronix S. A. Rue de l'Ouriette 129, 1170 Aubonne, Switzerland
[4]Group for Molecular Engineering of Functional Materials (GMF), Institute of Chemical Sciences and Engineering, Swiss Federal Institute of Technology (EPFL), CH-1951 Sion, Switzerland

*corresponding author email: piyasiri.ekanayake@ubd.edu.bn

Presently, over 85% of world energy requirements are satisfied by finite fossil fuels, which are inexpensive but with the concealed cost of detrimental consequences on health and environment[1]. On the other hand, solar power is infinite. Therefore, photovoltaic technologies are ideal to supply green and grid-free energy. The first generation silicon solar cells yield 25.6% laboratory efficiency, and 15 to 20% module efficiency depending on the manufacturer[2]. The second generation of thin-film technologies based on microcrystalline silicon, CdTe, and CIGS (copper indium gallium selenide) yields power conversion efficiency over 12 to 15%[2]. The third generation, based on dye-sensitized solar cells (DSC) and organic solar cells, has an efficiency in the range of 10 to 12%[3]. In the DSC, the functionalized sensitizers, shown in Figure 1a, anchors onto TiO_2 nanoparticles, and absorbs visible light to form excitons. At the interface between the sensitizer and the TiO_2 nanoparticles, excitons split into charges that are then collected at the electrodes. Modification of the light-absorbing sensitizer from a trinuclear[4] to a mononuclear ruthenium dye increased power conversion efficiency from 7% to 11%[5]. A molecularly engineered donor–chromophore–acceptor porphyrin-based sensitizer produced power conversion efficiency over 13%[6]. The three landmark sensitizers and the operating mechanism of the DSC are shown in Figures 1a and 1b, respectively. The DSC reported is based on a liquid electrolyte with iodine/iodide and cobalt redox mediators. The liquid electrolyte may be replaced by an organic or inorganic hole transporting material to form solid-state DSCs. The power conversion efficiency of the solid-state DSC is half of the liquid DSC due to issues with the infiltration of the hole transporting material caused by the pore size of the TiO_2.

Perovskite solar cells are considered to be the most promising photovoltaic technology because of their favorable power conversion efficiency of 22%, addressing the increasing energy demand, greenhouse gasses, and depleting fossil fuels[7]. The Perovskite solar cell (PSC) configuration is similar to the solid-state DSC where the sensitizer is replaced by the perovskite pigment[7]. The Perovskite, named after the Russian mineralogist L.A. Perovski, has a specific crystal structure with the ABX_3 formula. Where A is the organic cation situated at the eight corners of the unit cell, B is the metal cation located at the body center, and X represents the halide anion in the six face centers (see ***Figure 1***)[8]. The perovskite ABX_3 materials have significant advantages compared to other photovoltaic materials such as inexpensive precursors, high absorption coefficient, ambipolar charge transport properties, long carrier diffusion lengths, extremely low exciton binding energy. The band gap tunability by substituting "A" cations and "X" halides from I^- to Cl^-, and simple fabrication methods such as one step, sequential deposition and dual source sublimation as shown in ***Figure 2***.
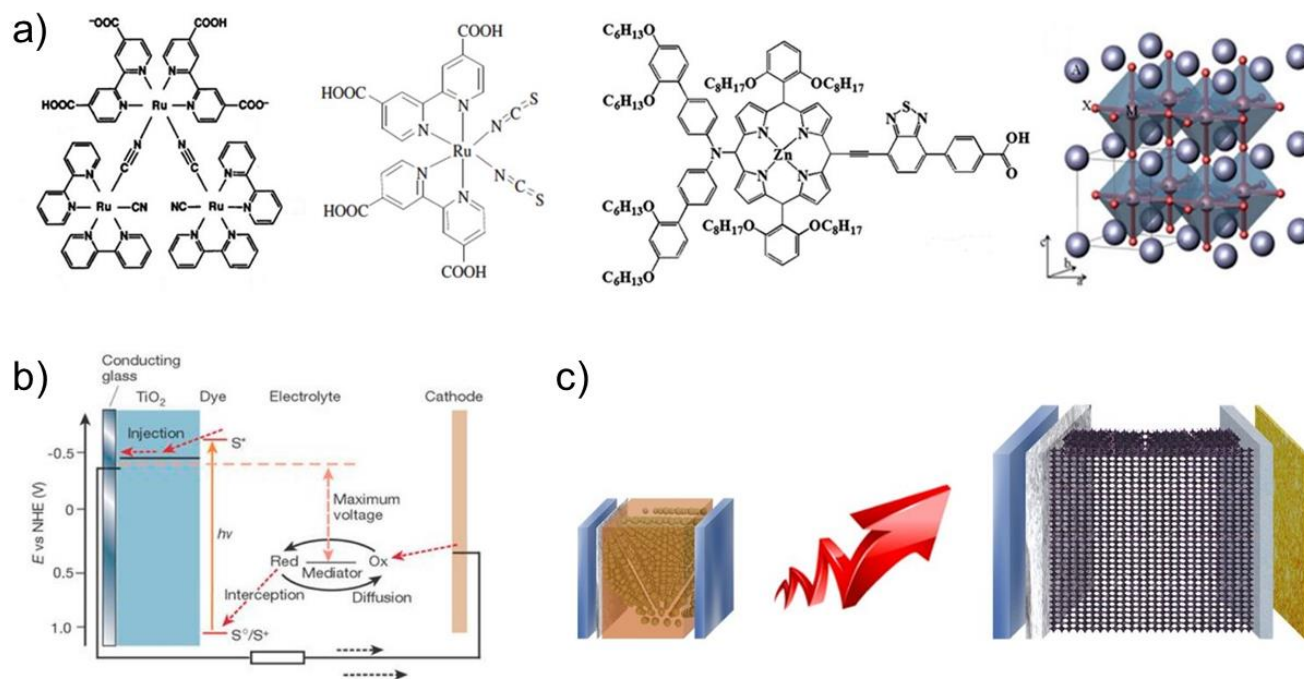
Figure 1. a) Chemical structures of landmark sensitizers and cubic perovskite of general formula, ABX_3; b) working principle of dye-sensitized solar cells (DSC); c) Now and then, showing an evolution of Perovskite solar cell (PSC) from DSC.
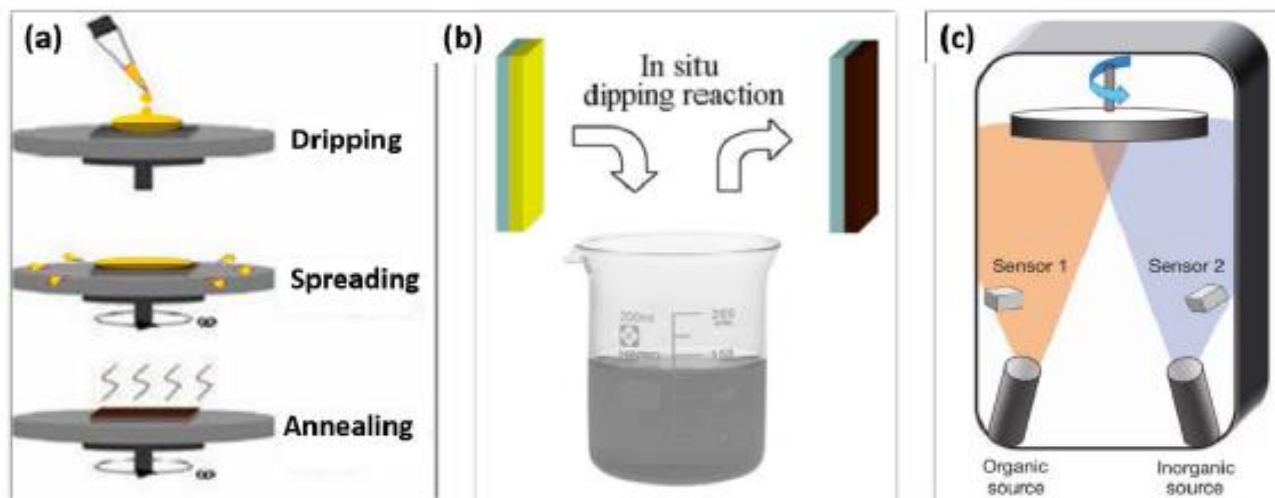
Figure 2. Three general methods for deposition of active perovskite layer. (a) one step, (b) sequential and (c) dual source sublimation.

Typical PSC configurations are n-i-p mesoscopic or planar and inverted p-i-n architecture. The configuration n-i-p devices composed of an electron transporting material TiO_2 (ETM), infiltrated with the perovskite absorbing material and coated with a hole transporting material (HTM), which plays an important role to facilitate the holes from perovskite to the gold as a back contact. The highest reported efficiency over 22% is based on n-i-p structure, where the perovskite is an intrinsic semiconductor, TiO_2 acts as an electron acceptor material (n-type layer), and poly tertiary aryl amine polymer (PTAA) as the hole transporter (p-type layer)[9-10]. Such a high PCE is achieved due to the relatively large open-circuit voltage (V_{OC}) of PSC, generally over 1.0 V, which is outstanding compared to other photovoltaic technologies such as organic- or silicon-based
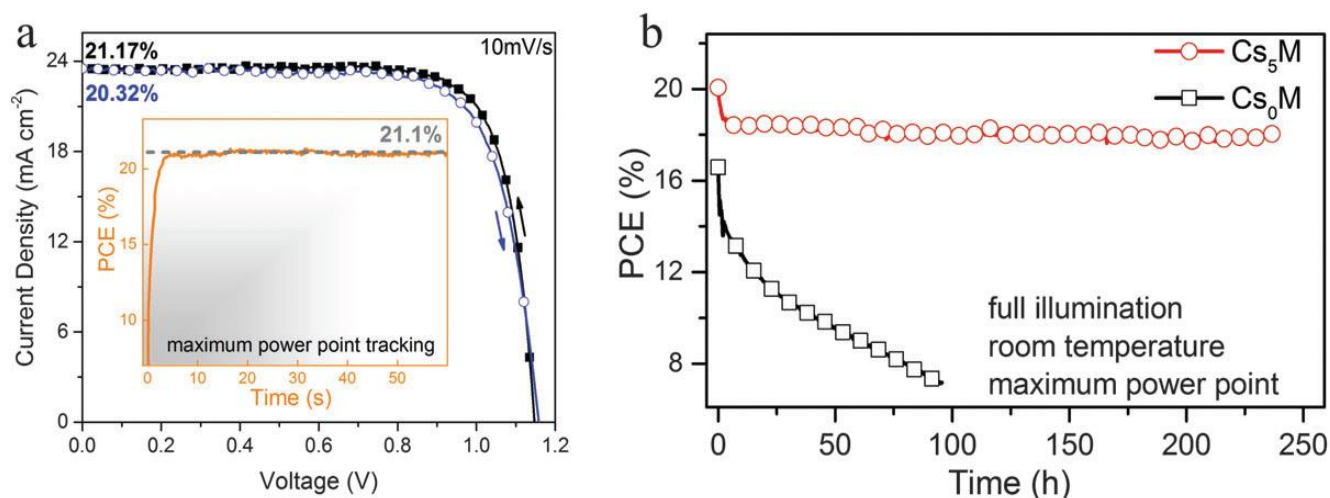
Figure 3. (a) Current–voltage scans for the best performing Cs_5M device showing PCEs exceeding 21% with little hysteresis. (b) Aging for 250 h of a high performance Cs_5M and Cs_0M devices in a nitrogen atmosphere held at room temperature under constant illumination and maximum power point tracking.
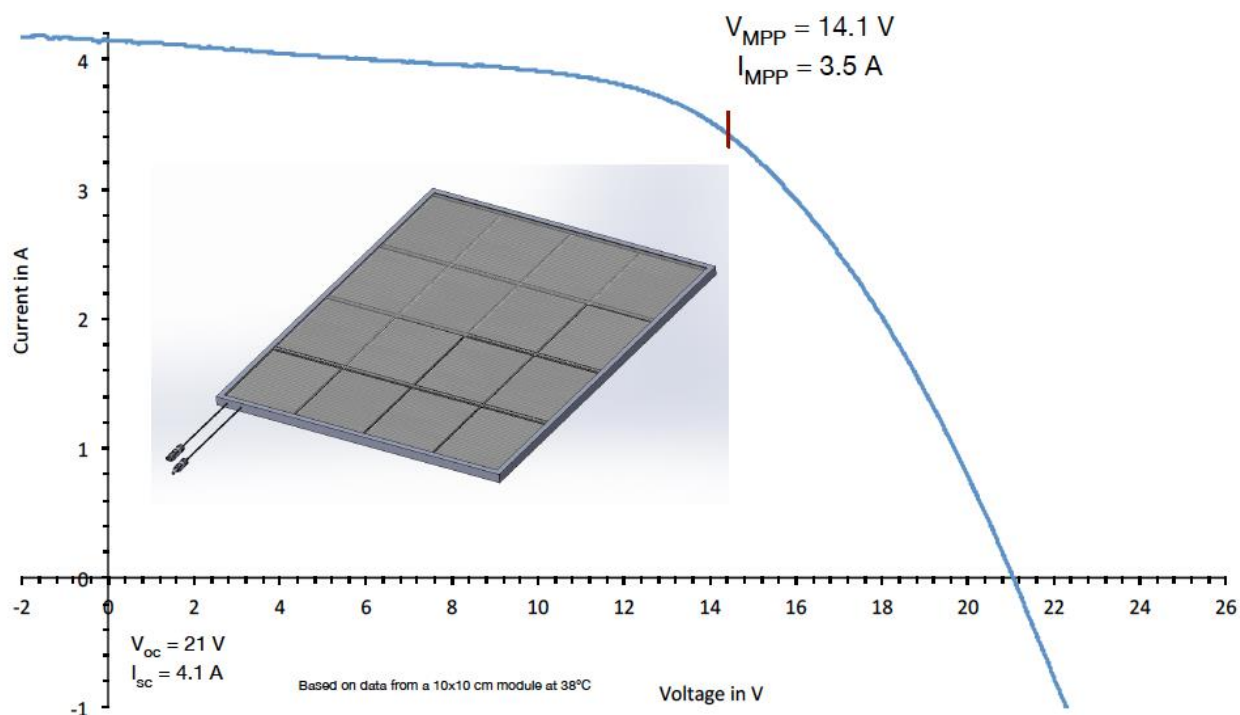
Figure 4. Solaronix large-area photovoltaic module characterization: IV characteristics of perovskite photovoltaic panel 0.85 m^2 measured under 1000 W/m^2 Sunlight. The stability data obtained at Solaronix over 8900 hours of light soaking and the projected cost will be <20 cents/Wp. The *I–V* plot of the perovskite panel is computed by extrapolation from a 10×10 cm mini-module.

solar cells. The energy loss ratio of V_{OC} to the bandgap energy (E_g) in PSC is lower than that of silicon solar cells; therefore the power conversion efficiency of PSC competes with the performance of silicon solar cells. The perovskite materials have a potential to reach over 25% power conversion efficiency, and the PSC is recognized by The World Economic Forum (2016) as one of the top 10 new technologies[11].

Nevertheless, the drawback of perovskite solar cells are several: i) poor material stability under heat and light soaking conditions; ii) reduced control over device operation, i.e. hysteresis in the

current-voltage characteristic, still poorly understood;[12] iii) material toxicity due to the presence of lead, and iv) device instability. To improve the stability, efforts in the optimization of pure $CH_3NH_3PbI_3$ by compositional engineering of cations, e.g., the substitution of the methyl ammonium (MA) cation by formamidinium (FA), and anions, e.g., introducing a small amount of Br, are needed. The addition of excess lead iodide has indeed induced a breakthrough in device efficiency and reproducibility. A large variety of perovskite compositions, particularly the mixed cation/mixed halide $(FAPbI_3)_{0.85}(MAPbBr_3)_{0.15}$ have been investigated, and recent developments even include triple cation structures containing cesium, MA, and FA to enhance the stability shown in *Figure 3*. A further advance in PSCs through significant innovation steps in material science, chemistry and device technology all combined could lead to a "paradigm shift" in the near-future energy sector. Perovskite solar cell using the hole conductor free configuration where the HTM layer is replaced by carbon, which acts as a contact electrode (see *Figure 4*)**.** The *J–V* characteristic data computed from extrapolation from 10×10 cm mini-module perovskite panel is shown in *Figure 4*. Since this configuration holds the promise to be at present the cheapest and the most attractive solution among the perovskite photovoltaic architectures. The future is bright for perovskite materials with a demonstrated power conversion efficiency of 22%; PSCs could lead a revolution in power generation, storage, and consumption through truly green grid-free energy.

References

[1] Sustainable Energy for All, http://www.se4all.org/

[2] M. A.. Green, K. Emery, Y. Hishikawa, W. Warta and E. D. Dunlop, *Prog. Photovoltaic Res. Appl.*, **2015**, 23, 1-9.

[3] U. Maxence, M. Gratzel, M.K. Nazeeruddin, T. Torres, *Chem. Rev. (Washington, DC, United States)*, **2014**, 114(24), 12330-12396.

[4] B. O'Regan, M. Grätzel, *Nature*, **1991**, 353, 737–740.

[5] M. K. Nazeeruddin, A. Kay, I. Rodicio, R. Humphry-Baker, E. Müller, P. Liska, N. Vlachopoulos and M. Grätzel, *J. Am. Chem. Soc.*, **1993**, 115, 6382-6390.

[6] S. Mathew, A. Yella, P. Gao, R. Humphry-Baker, F. E. CurchodBasile, N. Ashari-Astani, I. Tavernelli, U. Rothlisberger, M. K. Nazeeruddin and M. Gratzel, *Nat. Chem.*, **2014**, 6, 242.

[7] A. Kojima, K. Teshima, Y. Shirai and T. Miyasaka, *J. Am. Chem. Soc.*, **2009**, 131, 6050-6051.

[8] M. D. Graef and M. McHenry, "Structure of materials: an introduction to crystallography, diffraction and symmetry," *Cambridge University Press*, **2007**.

[9] M. M. Lee, J. Teuscher, T. Miyasaka , T. N. Murakami and H. Snaith, *J. Science*, **2012** 338, 643.

[10] "National Renewable Energy Laboratory Best Research-Cell Efficiencies," http://www.nrel.gov/ncpv/images/efficiency_chart.jpg

[11] "Top 10 emerging technologies of 2016. World Economic Forum," https://www.weforum.org/agenda/2016/06/top-10-emerging-technologies-2016/

[12] S. Meloni, T. Moehl, W. Tress, M. Franckevicius, M Saliba, Y. H. P.Gao, M. K. Nazeeruddin, S. M. Zakeeruddin, U. Rothlisberger and M. Graetzel, *Nat. Commun.*, **2016**, 7, 10334.

Recent Progress in the Development of Soft Robots

Feifei Chen[1], Hongying Zhang[1], Tao Wang[2] and Michael Yu Wang[3,4]*

[1]*Department of Mechanical Engineering, National University of Singapore, Singapore*
[2]*State Key Laboratory for Manufacturing System Engineering, Xi'an Jiaotong University, Xi'an 710049, People's Republic of China*
[3]*Department of Mechanical and Aerospace Engineering, Hong Kong University of Science and Technology, Clear Water Bay, Kowloon, Hong Kong*
[4]*Department of Electronic and Computer Engineering, Hong Kong University of Science and Technology, Clear Water Bay, Kowloon, Hong Kong*

*corresponding author email: mywang@ust.hk

Abstract

Soft robots, are mobile machines largely constructed from soft materials and have received much attention recently because they are opening new perspectives for robot design and control. This paper reports recent progress in the development of soft robots, more precisely, soft actuators and soft sensors. Soft actuators play an important role in functionalities of soft robots, and dielectric elastomers have shown great promise because of their considerable voltage-induced deformation. We developed soft inflated dielectric elastomer actuators and their networks, with the advantages to be highly deformable and continuously controllable. When it comes to control of soft robots, soft sensors are of great importance. We proposed a methodology to design, analyze, and fabricate a multi-axis soft sensor, made of dielectric elastomer, capable of detecting and decoupling compressive and shear loads with high sensitivity, linearity and stability.

Index Terms: soft robots, soft actuators, soft sensors, dielectric elastomer

1. Introduction

Soft robotics has become a hot research field in the past decade. Rigid robots often encounter difficulties operating in unstructured and highly congested environments. On the contrary, the use of soft materials in robotics, driven not only by new scientific paradigms but also by many applications, is going to overcome these basic assumptions and makes the well-known theories poorly applicable, opening new perspectives for robot design and control.[1] Rather than relying on sliding or rolling motion as in traditional mechanics, soft robots produce their mobility based on the deformation of elastic members. This enables the integration of multiple functions into simple topologies, by embedding soft actuators and soft sensors to build fully functional and distributed structures capable of complex tasks.

Generally, a soft robot system includes soft bodies that may consist of elastic and/or rigid parts, soft actuators and soft sensors. A basic requirement of a soft robot is to generate large enough deformation, especially when the interaction with the environment is involved. The current examples of soft robots offer some solutions for actuation and control, though very first steps.[2] The biggest challenges in soft robotics currently are the design and fabrication of soft bodies, development of robust soft actuators capable of withstanding large deformations and delivering considerable stiffness, and soft sensors applicable to complex loading conditions with a large detection range, etc.

This paper will briefly report our recent progress in the development of soft actuators and soft sensors. Specifically, dielectric elastomer balloon-

like actuators are developed, showing to be highly deformable and continuously controllable. Also, a multi-axis soft sensor is developed, made of dielectric elastomer, with the capability of detecting both compression and shear loads.

2. Soft actuators

Soft robots are able to operate with several different modes of actuation (say, pneumatic, electrical, etc). Dielectric elastomers, capable of deforming in response to an external electric field, have shown great promise for soft actuators due to their large voltage-induced deformation. Here we focus on dielectric elastomer actuators.[3,4]

2.1. Networked dielectric elastomers actuators

Balloon-like dielectric elastomer actuators have received much attention since the inside air of high pressure can provide prestretch to greatly improve the actuation performance.[5] The deformation of dielectric elastomers, however, is strictly restricted because of material failures such as loss of tension and electric breakdown. With these regards, we developed networked dielectric elastomer balloon actuators, coated with compliant electrodes and interconnected via a rigid chamber, as shown in *Figure 1*. For the networked system, the input voltages are independently applied to the balloons, resulting in the output deformations of the balloons. The networked design is able to greatly postpone the occurrence of material failures and thus remarkably enlarge the actuation range.[6]
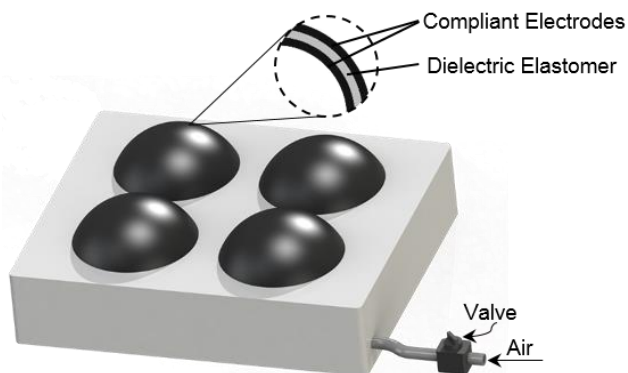
Figure 1. Illustration of networked soft inflated actuators, interconnected via a chamber. Each actuator, coated with compliant electrodes on its surfaces, is independently connected to a high voltage.

Figure 2 shows the overview of the experimental setup, and some experimental results. Initially the balloons are pumped until the net pressure reaches 2kPa. Thereafter, the system is sealed and then voltages are applied. When only one balloon is activated, the activated balloon deforms largely (say, about 3 times the volume of the prestretched state), the inside pressure drops accordingly, and the others shrink (*Figure. 2b*). The underlying reason for large deformation is that the three passive chambers effectively slow down the drop of inside pressure, sustain the mechanical stresses of the actuated membrane, and thus postpone the occurrence of material failures. When three balloons are activated, the inner pressure drops and the unactivated balloon to shrinks greatly (almost flat, see *Figure 2c*). This actuation mode typically explores the minimum volume of the balloon.
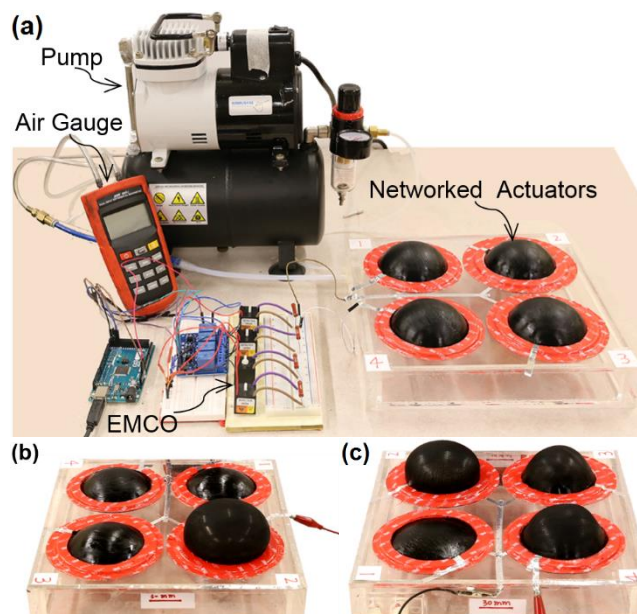
Figure 2. Experimental results: (a) system setup; (b) one balloon is activated; (c) three balloons are activated.

2.2. Dielectric elastomer actuators for soft WaveHandling systems

We developed a soft handling system, aiming to offer a soft solution to delicately transport and sort fragile items like fruits, vegetables, biological tissues in food and biological industries. The system consists of an array of hydrostatically coupled dielectric elastomer actuators. *Figure 3*

conceptually shows one 'unit' of the system, where one active dielectric elastomer and one passive membrane are coupled together via an air mass. When the dielectric film is activated by an external electric field, the passive membrane will deform accordingly, due to the variation of the internal pressure. The assembly of such 'unit' constitutes the WaveHandling system and the controls of multiple active membranes enable movements of the system (see ***Figure 4***).
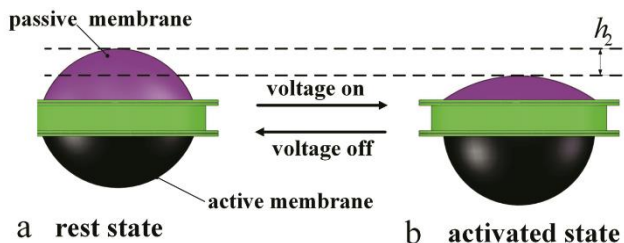
Figure 3. Hydrostatically coupled dielectric elastomer actuators: (a) rest state and (b) activated state.
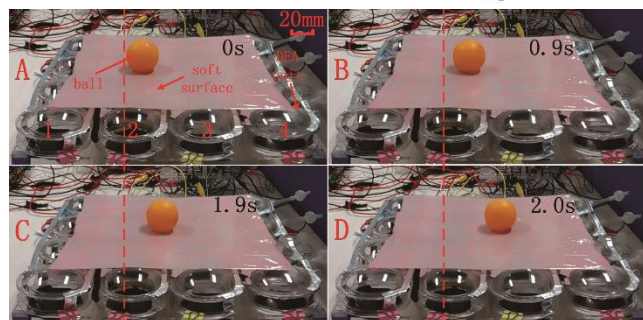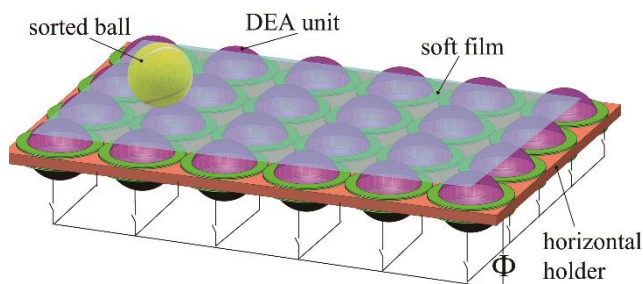
Figure 4. A soft handling system transfers a ball from one location to another location.

As a proof of design concept, a simply made prototype of the handling system is controlled to generate a parallel moving wave to manipulate a ball. The electric control, simple structure, lightweight and low cost of the soft handling system show great potential to move from laboratory to practical applications.[7]

3. Soft sensors

Soft sensors play an important role in control of soft robots, by providing feedbacks of deformations, forces, etc. There are mainly two popular avenues to convert the induced deformation to electrical signals: converting to resistance changes or converting to capacitance changes. The capacitance-based soft sensors show better performance in terms of accuracy and repeatability, and thus are adopted in this paper.

To overcome the limitations of existing soft sensor designs—rigid electrodes, low sensitivity, limited detection range, and inability in decoupling multi-axis loads, we proposed a methodology to design, analyze, and fabricate multi-axis soft sensor. The soft sensors each consist of four capacitor modules aligned in a 2×2 array. An isolated air chamber is embedded into each module to amplify the deformation (***Figure 5a***), resulting in an enhancement in the sensitivity. We investigated a compressive sensor[8] (***Figure 5b***) and two types of multi-axis sensor, i.e. the circular type and rectangular type (***Figures 5c*** and ***5d***)[9]. ***Figure 6*** shows the fabrication process and the prototypes, where the compressive sensor is made of Eco-Flex 30 (Smooth-On), while the multi-axis soft sensors are composed of polydimethylsiloxane (PDMS).
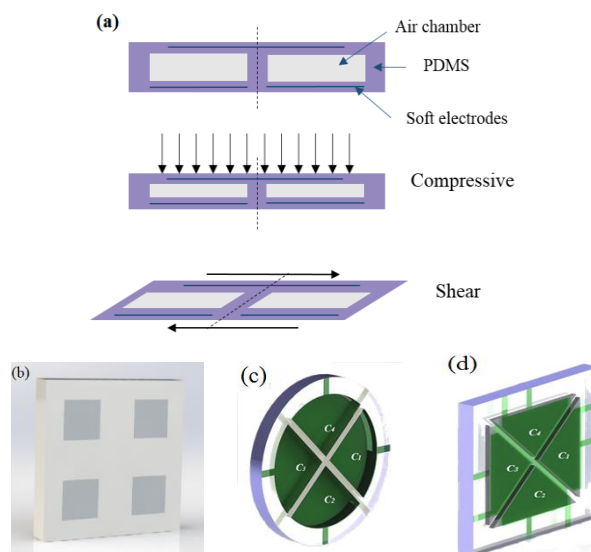
Figure 5. Soft sensor prototypes. (a) Loading conditions. (b) Compressive sensor. Multi-axis soft sensor of (b) circular prototype and (c) rectangular prototype.
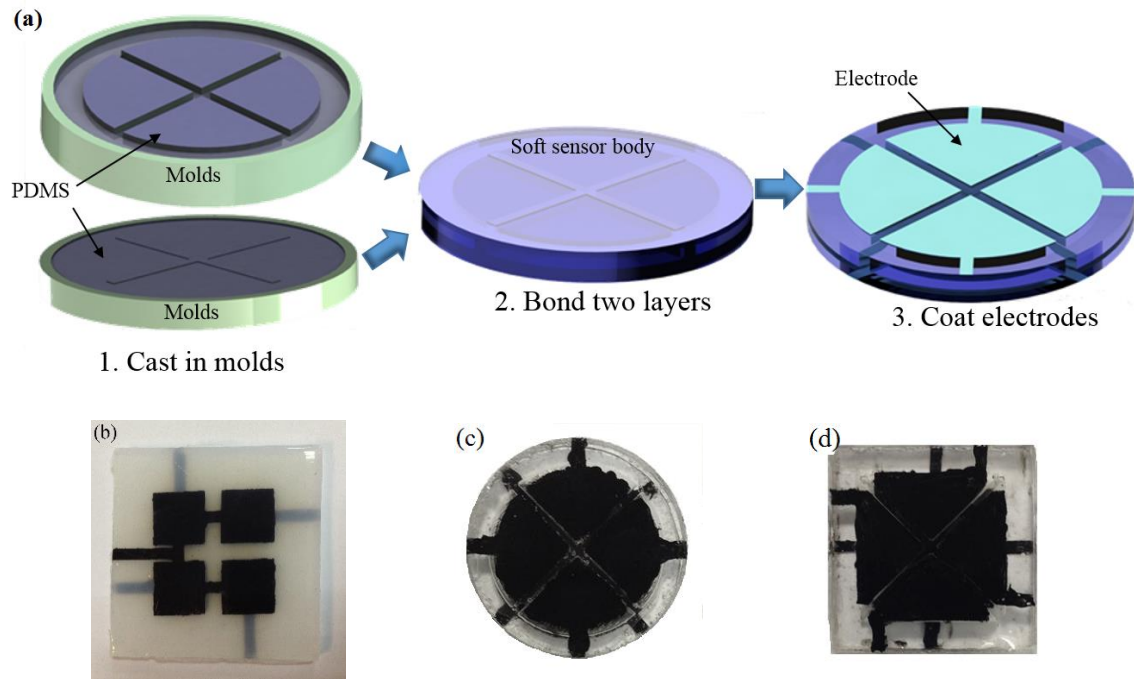
Figure 6. Fabrication process and samples. (a) Fabrication process of circular prototype. (b) Circular prototype. (c) Rectangular prototype.
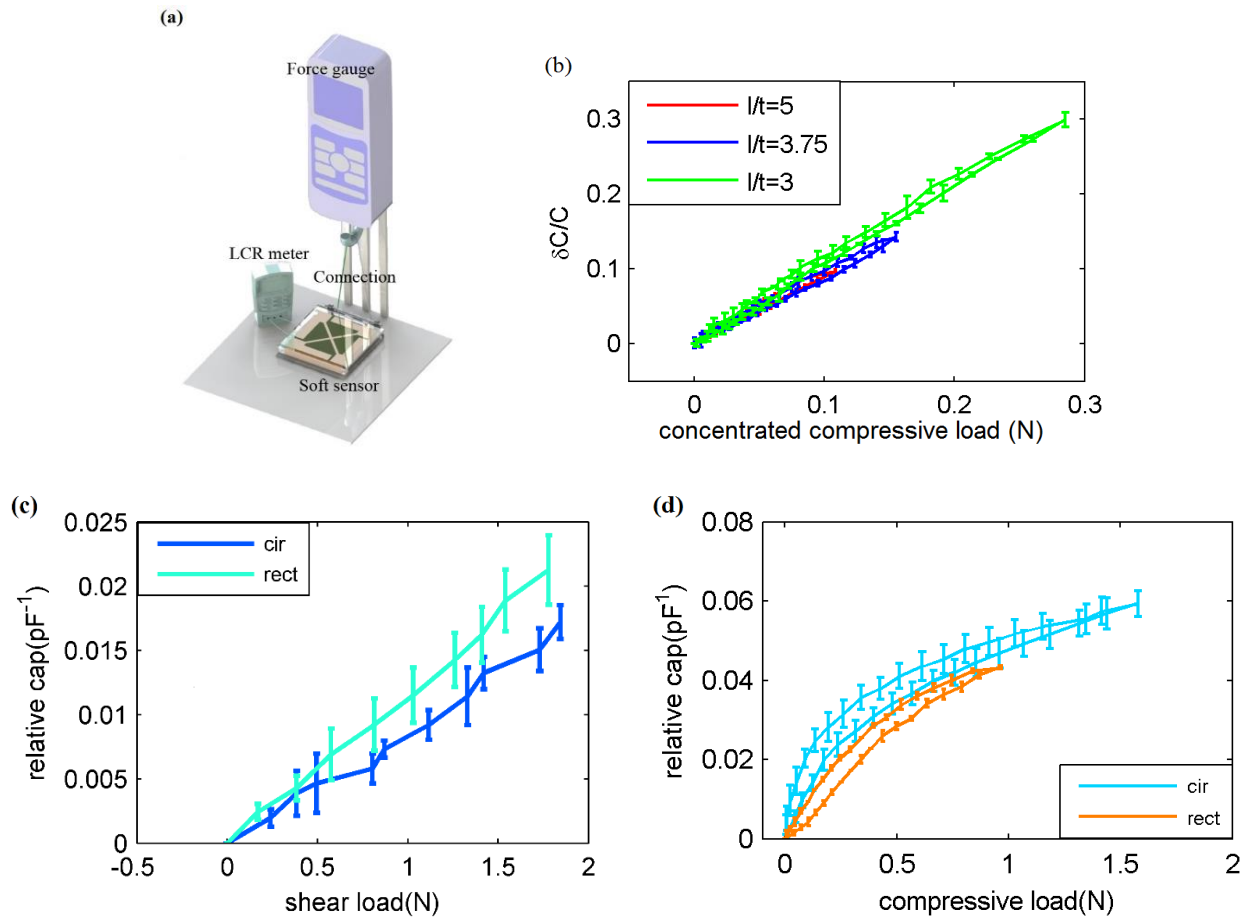
Figure 7. Experimental setup (a) and results for compression sensor (b), and multi-axis sensor under shear (c) and compression (d).

The experiments are carried out on the Mark-10 testing system. Specifically, the concentrated compression loading condition is applied via a conical punch and the shear loading is applied via two plates wherein the sensor is sandwiched. *Figure 7a* shows an overview of the experimental setup, where the force gauge can measure the applied force (in forms of either compression or shear), and the LCR meter measures the capacitance of the soft sensor that keeps increasing with the applied force.

Figures 7b-7d show the responses of the compressive sensor under compression and the multi-axis sensor under both compression and shear loading, where the circle design is denoted by 'cir', the rectangle design is denoted by 'rect', and *l/t* denotes the aspect ratio of the soft sensor and its value is determined empirically. It is specially noticed that the capacitance increases monotonously with the loading and shows good repeatability within a large enough detection range.

4. Conclusion

This paper has briefly reported our recent progress regarding soft robots, from the networked dielectric elastomer actuators and Wavehandling system driven by soft actuators, to soft sensors capable of detecting both compressive and shearing loadings. These advancements basically represent a further step toward the development of soft robots. In the future work, we hope to integrate the soft actuators and sensors into soft bodies to build soft robots in terms of specific functionalities, such as a soft gripper.

References

[1] C. Laschi and M. Cianchetti, *Front. Bioeng. Biotechnol.*, **2014**, 2, 3.

[2] D. Rus and M. T. Tolley, *Nature*, **2015**, 521(7553), 467-475.

[3] R. Pelrine, R. Kornbluh, Q. Pei and J. Joseph, *Science*, **2000**, 287(5454), 836-839.

[4] Z. Suo, *Acta Mechanica Solida Sinica*, **2010**, 23(6), 549-578.

[5] F. Chen and M. Y. Wang, *IEEE Robotics and Automation Letters*, **2016**, 1(1), 221-226.

[6] F. Chen, J. Cao, L. Zhang, H. Zhang, M. Y. Wang, J. Zhu and Y. F. Zhang, "Networked soft actuators with large deformations," *ICRA*, **2017** (submitted).

[7] T. Wang, J. Zhang, J. Hong and M. Y. Wang, "Dielectric elastomer actuators for soft WaveHandling systems," *Soft Robotics* (in press).

[8] H. Zhang, M. Y. Wang, J. Li and J. Zhu, *Smart Materials and Structures*, **2016**, 25(3), 035045.

[9] H. Zhang and M. Y. Wang, *Soft Robotics*, **2016**, 3(1), 3-12.

Is pull-apart basin tectonic model feasible for the formation of Kashmir basin, NW Himalaya?

A. A. Shah[*], Mohammad Noor Firdhaus bin Yassin and Muhammad Izzat Izzuddin bin Haji Irwan

Physical and Geological Sciences, Faculty of Science, Universiti Brunei Darussalam, Jalan Tungku Link, Gadong, BE 1410, Brunei Darussalam

*corresponding author email: afroz.shah @gmail.com

Abstract

An oval shaped Kashmir Basin in NW Himalaya largely reflects the typical characteristics of Neogene-Quaternary piggyback basin that was formed as a result of the continent-continent collision of Indian and Eurasian plates. However, a new model shows that the basin was formed by a major dextral strike-slip fault (Central Kashmir Fault) that runs through the Kashmir basin. This model is not only unlikely but also structurally unrealistic, and poses problems with the geomorphology, geology, and tectonic setting of the Kashmir basin. Although Shah (2016) has clearly demonstrated that such a model is not feasible for Kashmir basin, however in this article initial works have been further strengthened, and we demonstrate through various evidence, which includes a structural analogue modeling work, that a pull apart basin formation through strike-slip faulting is impractical for Kashmir basin. Further we show that Central Kashmir Fault, a proposed major dextral strike-slip fault, could not possibly exist.

Index Terms: pull-apart basin, Kashmir basin, NW Himalaya, Strike-slip fault

1. Introduction

Kashmir basin of NW Himalaya (***Figure 1***) is located ~100 km away from the Main Frontal thrust (MFT) fault, which is one of the major active south-verging fault systems in the region. The Zanskar shear zone (ZSZ), a major normal fault, lies to the northeast of the basin, whereas the Main Central thrust (MCT), the Main Boundary thrust (MBT), and the Raisi thrust (RT) systems respectively lie on its southwest[1-2]. This structural skeleton of the basin largely fits a piggyback-deformation model because a series of thrusts lies to the south of the young Kashmir basin that sits on top of these faults[3-4]. Sedimentation in Kashmir basin has possibly commenced by ca. 4 Ma and resulted in deposition of >1300 m of sediments (known as Karewas) at inferred average rates of ~16–64 cm/1000 yr[3,5]. These sediments are dominantly of fluvio-lacustrine and glacial origin[6-8] and were deposited on basement rocks composed of Pennsylvanian–Permian Panjal volcanic series[9] and Triassic limestone[10].

The Holocene sediments in Kashmir basin are recently broken, this is shown by a number of ~SE dipping faults, and this makes it a classic example of an out-of-sequence faulting in NW Himalaya[11-14]. Although a piggy-back basin model seems to largely fit the tectonic evolution of Kashmir basin however Alam et al.[15-16] have introduced a pull-apart basin tectonic model where they suggest that Kashmir basin was formed as a result of a large dextral-strike-slip fault that runs ~ through the center of the basin. Such a model, however, is structurally impractical[4] and the present work further shows why Kashmir basin could not fit a pull-apart basin tectonic setting as suggested by Alam et al.[15].

2. Tectonic and geological background

The location of the basin is north of the MFT fault zone, the megathrust structure that accommodates a larger portion of the regional convergence between the Indian and Eurasian plates[17,1], and is considered actively growing[18-20].
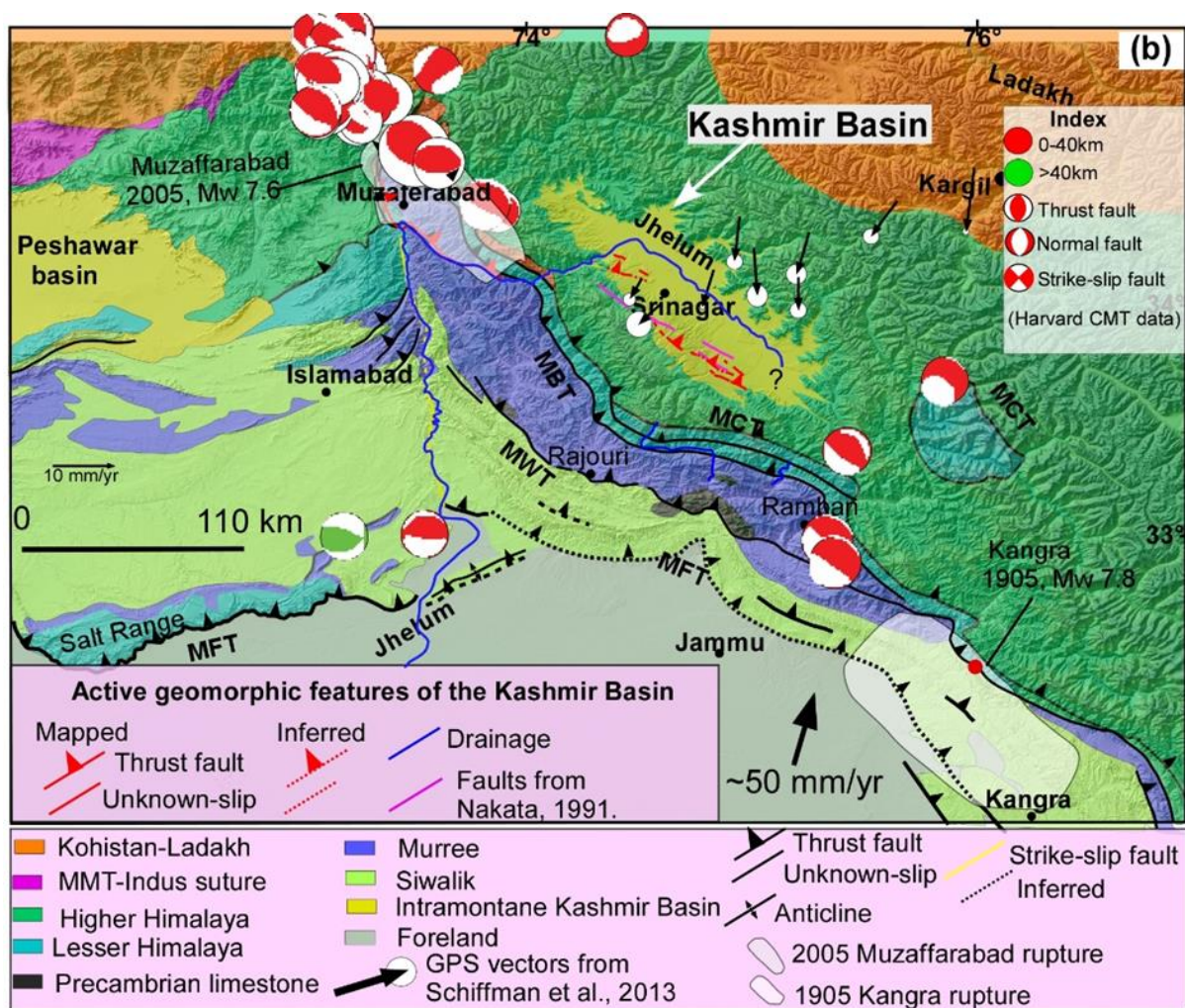
Figure 1. Regional tectonic setting of Kashmir basin, NW Himalaya (after Shah, 2016[14]). MCT—Main Central thrust, MBT—Main Boundary thrust, MWT—Medlicott–Wadia thrust, and MFT—Main Frontal thrust. CMT—centroid moment tensor; GPS—global positioning system.

Until now the surficial trace of the MFT has not been mapped in any part of the Jammu and Kashmir region, and thus it is assumed as a blind tectonic structure under Jammu [1, 14]. Schiffman et al.[17] have demonstrated that MFT fault is presently locked under the Kashmir region, and a major earthquake is anticipated in the future but the timing remain uncertain. A major active fault (Raisi fault) that runs under Raisi *(Figure 1)* is also considered to host a major earthquake[1] in the future. And a third major fault runs approximately through the middle of the Kashmir valley *(Figure 1),* which also has the potential to host a major earthquake, very similar to the Muzaferabad earthquake of 2005[13]. Since most of the faults are ~S-SW verging and Kashmir basin sits on these structures thus such a structural setting can be

explained by a piggyback basin tectonic mode[18] because a young basin sits on older faults.

Moreover, the geological map (*Figure 1*) of Kashmir basin shows Upper Carboniferous-Permian Panjal Volcanic Series and Triassic limestone are the foundation rocks on which ~1,300-m thick sequence of Plio-Pleistocene fluvio-glacial sediments are deposited[10].

These sediments are mostly unconsolidated clays, sands, and conglomerates with lignite beds unconformably lying on the bedrock with a cover of recent river alluvium[6,8]. The bedrock geology indicates a deep marine depositional setting, where limestone could form, and later such a depositional environment was closed, faulted, and
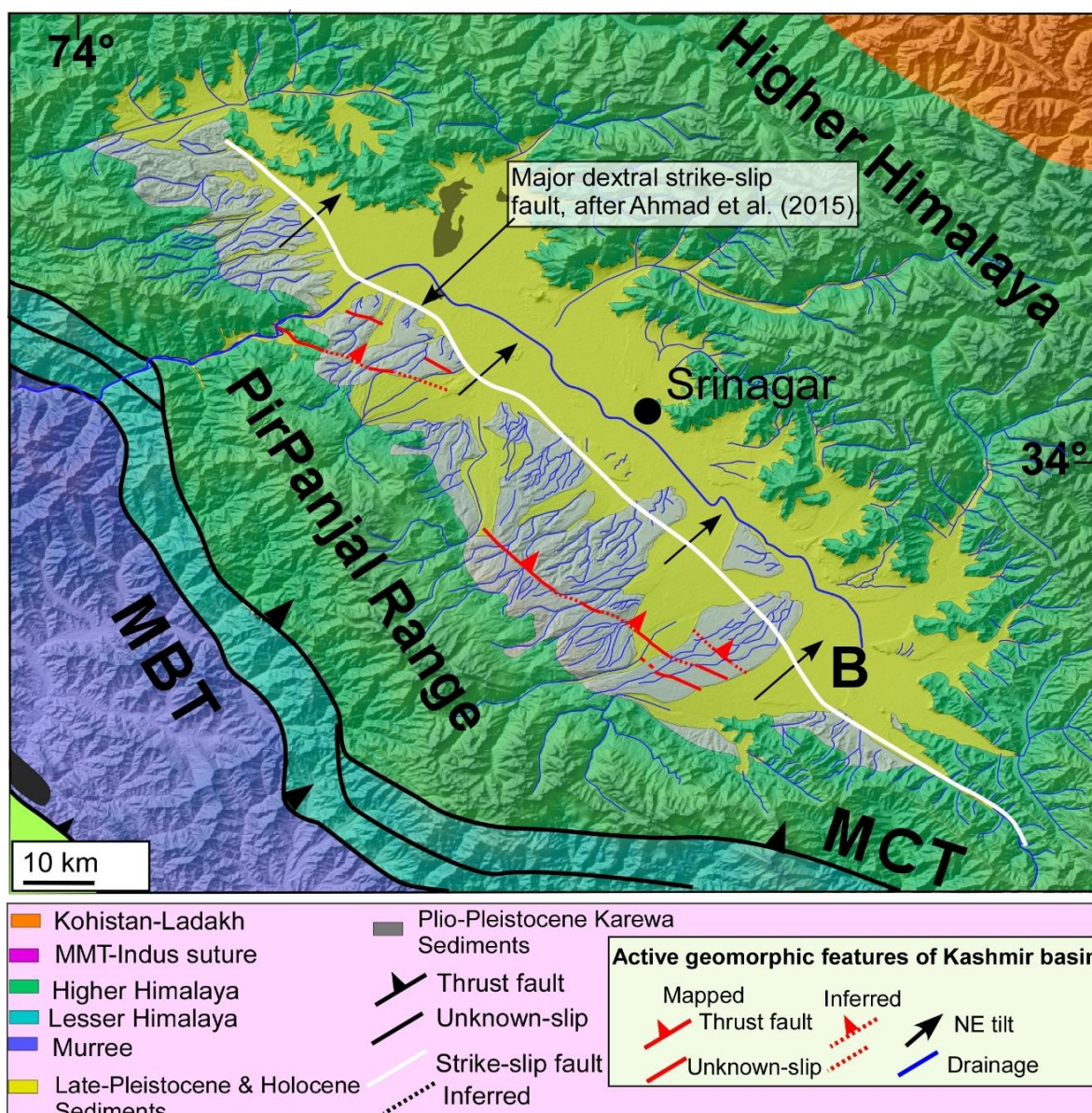
Figure 2. Simplified geology, and structural map of Kashmir basin, NW Himalaya showing the major extent of the major dextral fault (Modified from Thakur et al., 2010, and Shah, 2013a, 2015a), MCT=Main Central Thrust, MBT =Main Boundary Thrust. The Central Kashmir fault (CKF) of Ahmad et al. [15] runs through the basin.

uplifted. The formation of Kashmir basin followed the closure of such a setting, and later it was filled in with Plio-Pleistocene fluvio-glacial sediments are deposited[8]. A typical feature of a piggyback basin.

3. Is pull-apart basin tectonic model possible for Kashmir basin?

3.1. Structural evidence
Central Kashmir Fault (CKF), a proposed major dextral fault of Alam et al.[15], is argued to have

formed the Kashmir basin through a pull-apart tectonic style.

The strike-length of Kashmir basin is ~150 km, and the mapped length of the dextral strike-slip fault is ~165 km, which runs through the center of the basin - this however, is structurally unlikely (***Figure 2***). This is because if a major strike-slip fault produces a pull-apart basin, then the trace of that fault should not run through the middle of the basin; it will mostly likely run through the margins of the basin and always away from its center.
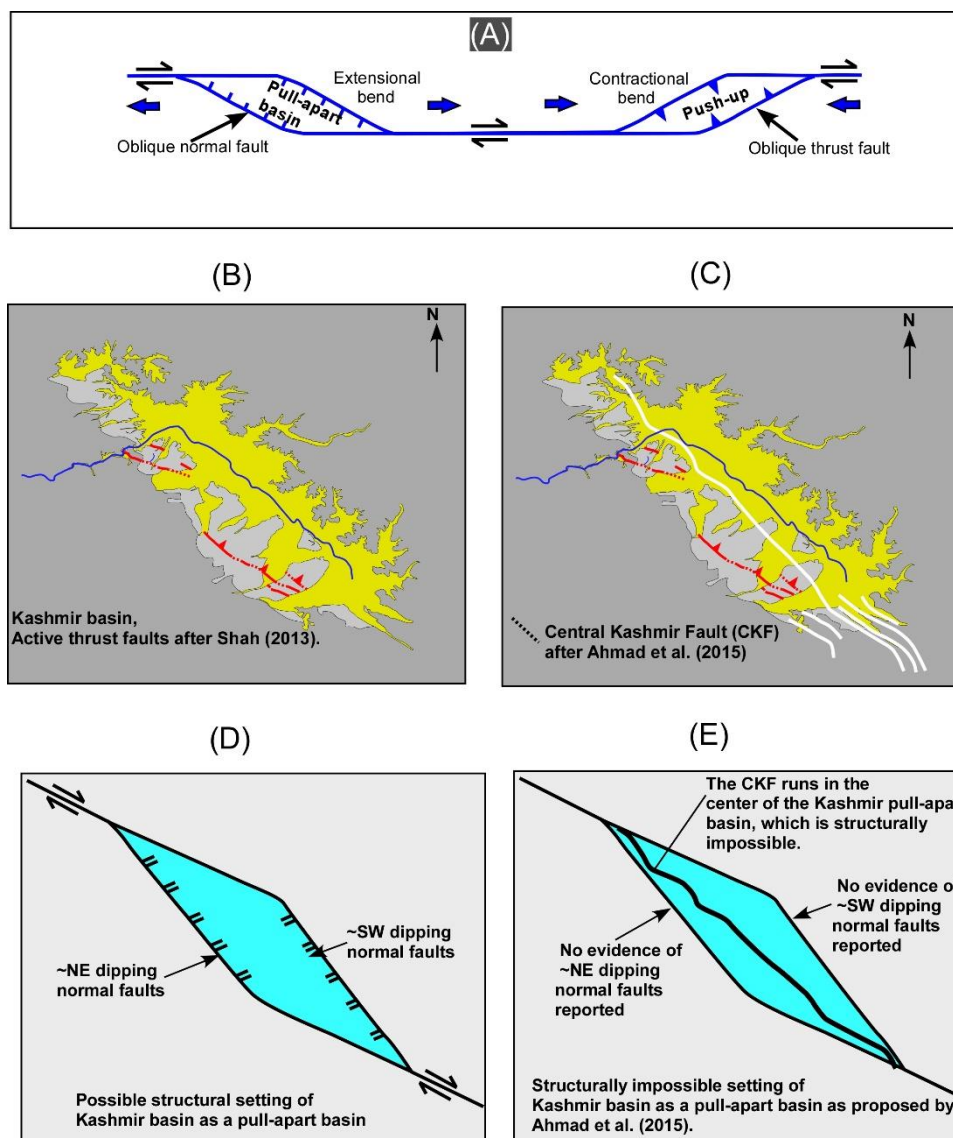
Figure 3. (A) Structures associated with a typical pull-apart basin setting. (B) Kashmir basin with mapped traces of active thrust faults (after Shah, 2013a[12]). (C) Shows the mapped trace of Central Kashmir Fault (CKF) and the associated horsetail structures. (D) A typical example of a dextral strike-slip fault system and a series of normal, oppositely verging faults that accompany such deformation pattern. (E) The mapped trace of the CKF which runs in the middle of the Kashmir basin - a proposed pull-apart basin, which is structurally not practical.

Therefore, the proposed location of the major trace of the CKF through the center of the Kashmir basin (a pull-apart product of CKF) is thus unlikely.

In addition to this, to form a ~165 km long basin usually- a series of ~SW, and ~NE dipping normal faults are required *(Figure 3)* in symmetrical extension. However, should the extension be asymmetrical, the normal faults would be expected to have either a ~SW or ~NE dipping fault planes or both. Typically, pull-apart tectonic movements will break the crust, extending it and later forming a series of normal faults. No evidence of such structures are reported in Kashmir basin in the expected orientation. And such structural setup will usually have a unique skeleton that could dominate the observed topography and geomorphology in an area with oppositely dipping normal faults. This, however, has not been reported in the Kashmir basin. Furthermore, the strike-length of the major dextral-strike slip faults is ~planar and contiguous; such geometry cannot cause extension
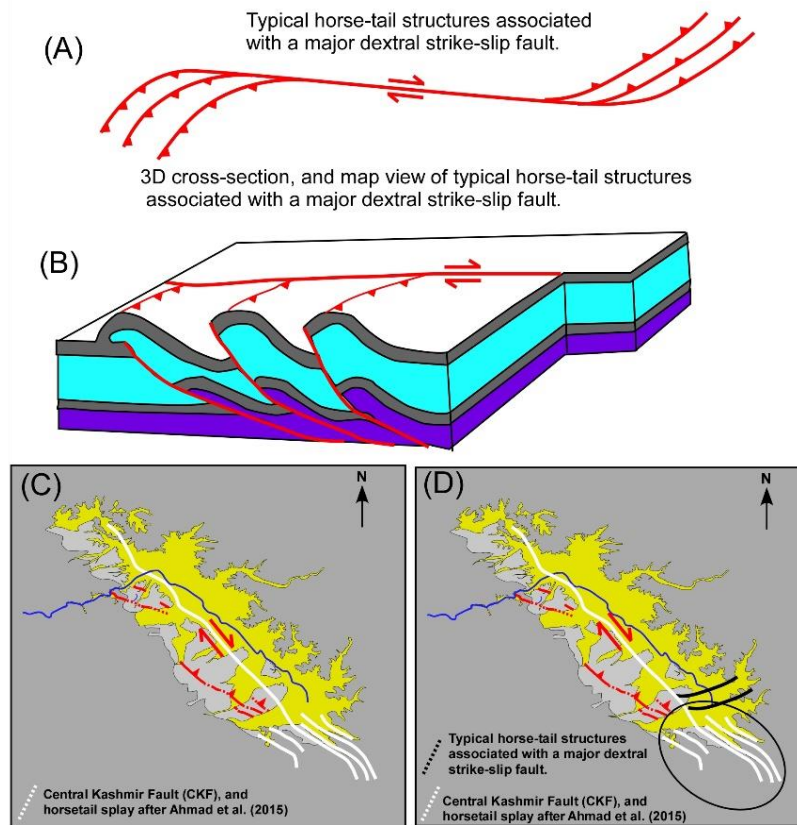
Figure 4. (A) An example of a typical dextral strike-slip fault system and the associated horsetail structures, (B) 3D view of what is shown in (A), (C) Kashmir basin with mapped traces of active thrust faults (after Shah, 2013a)[22] and the major dextral strike slip fault of Ahmad et al. [15]. (D) The orientation of horsetail structures of Ahmad et al.[15] is unlikely for a major dextral-strike slip fault system that has ~ NW-SE strike (horsetails should be at angles to the fault).

to form a pull-apart basin and on the contrary such basins are typical features of step-overs and linkage fault geometries[21,4] (***Figure 3***).

3.2. Horsetail splay faults

When a major strike-slip fault zone terminates in brittle crust, the displacement is usually absorbed along small branching faults. These curve away from the strike of the main fault, and form an open, imbricate fan called a horsetail splay[21]. In a classic dextral strike-slip fault system such faults could be of certain restricted orientation with respect to the trace of the main fault (***Figures 2*** and ***4***). The orientation of the major strike-slip fault of Kashmir basin is reported to be ~NW-SE[15, 16], and the horsetail faults, which appears as imbricate fans, are shown to be of the same orientation as the major fault (~NW-SE). This is not structurally possible (***Figure 4***) and it conflicts with the basic style of such faulting.). Technically, with the

~NW-SE strike of the major fault, the imbricate fans will either have a SW strike with a NW tectonic transport, or NE strike with a SE tectonic transport (***Figure 4c*** and ***Figure 4d***).

3.3. Geologic and geomorphic evidence

The bedrock geology of Kashmir basin shows Upper Carboniferous-Permian Panjal Volcanic Series and Triassic limestone are covered by Plio-Pleistocene fluvio-glacial sediments[10]. There is no evidence of a large scale topographic, or lithology offset which is typically associated with a major dextral strike-slip fault system. Shah[12] mapped dextral offset of streams on the SE of Kashmir basin, however, minor (~20 to ~40 m) offset of these channels are interpreted to have resulted from the regional oblique convergence between India and Eurasia, and it does not suggest or approve of a major dextral strike slip fault system as reported by Alam et al.[15].

3.4. Geodetic evidence
Shah[22] mapped the eastern extent of the KBF fault and argued for a clear right-lateral strike-slip motion for a distance of ~1km which was shown by the deflection of young stream channels. The lateral offset was shown to vary from ~20 to ~40 m. This was suggested to be a classical example of oblique convergence where thrusting is associated with a small component of dextral strike-slip motion.

The recently acquired GPS data from Kashmir Himalaya[17] confirms these observations, and further suggests an oblique faulting pattern wherein a range-normal convergence of 11 ± 1 mm/y is associated with a dextral-shear slip of 5 ± 1 mm/y (***Figure 1***). They also suggest that obliquity is more towards the eastern portion of the valley. This clearly suggests that the regional stress average vector is oblique in Kashmir Himalaya and, thus, the deformation is mainly absorbed by range-normal components, and less so by shear components—a typical feature of oblique convergence. Furthermore, in the case where the existence of Kashmir Central Fault is considered, the GPS data resolve on it show the dominance of normal convergence and not shearing parallel to the strike of this fault.

The reason for there being more dextral slip towards SE of Kashmir basin is possibly because of the regional escape tectonics where India acts like an indenter and, hence, the crustal flow is mostly along the huge strike-slip faults[23]. It could possibly also mean that there might be some large-scale unknown strike-slip faults in NW Himalaya.

3.5. Paper model
A map of Kashmir basin with the actual trace of the CKF[15] shows that any strike-slip movement on it would produce a range of small sized pull-apart basins (***Figure 5***). Such basins are not visible in any portion of Kashmir basin along its strike length (***Figure 1***).

Thus it is now established that a pull-apart genesis of Kashmir basin is unlikely because such a fault cannot pass through the basin; it ought to be at the margins. The paper model shows the possibility of

at least 5 small pull-apart basins along the proposed trace of CKF and even at those regions the fault is not shown to cut through the basins but lie at their margins (***Figure 5b***). Such is what should be expected for a typical pull-apart basin.

4. Discussion
The present geological and structural architecture of Kashmir basin is largely consistent with a piggy-back model[8] as Kashmir basin is riding on a number of ~SW verging thrust faults[1,2] (***Figure 1***). Presently, three major fault systems are considered active[12, 13, 14], and from south these are Main Frontal Thrust (MFT), Medlicott-Wadie Thrust (MWT), and Kashmir Basin Fault (KBF).

The new model of Alam et al.[15] proposes a pull-apart tectonic model where a major dextral strike-slip fault (Central Kashmir Fault; CKF) is suggested to have formed the Kashmir basin through pull-apart movement (***Figure 2***). The ~150 km long Kashmir Basin is cut through by the proposed dextral strike-slip fault for ~165 km. And, the fault is proposed to run though the center of the basin, which is unlikely (***Figure 2***). This has also been demonstrated by the paper model that shows a range of small pull-apart basins when CKF moves. The fault that produces the basin lies at its margins and does not cut through the basin (***Figure 5b***). Thus, it poses a strong structural problem for the pull-apart model.

Furthermore, it is problematic to create the present structural skeleton of Kashmir basin by a major dextral strike-slip fault, even if it has an oblique slip component (***Figures 3*** and ***4***). This is because if a major dextral- slip is associated with a normal dip-slip component, which is shown by the pull-apart model[15], then the overall topography and geomorphology should ~ suggest subsidence on hanging-wall portions and relative uplift on foot-wall portions. This requires two scenarios: a) the major fault must be dipping SSW or 2) NNE. The pull-apart model[15] shows topographic depression on the right side of the major fault (NNE side), which requires a NNE dipping fault with a normal faulting component. However, the entire Kashmir basin tilts ~NE (***Figure 1***) and there is no evidence of regional normal faulting. Moreover, there is no
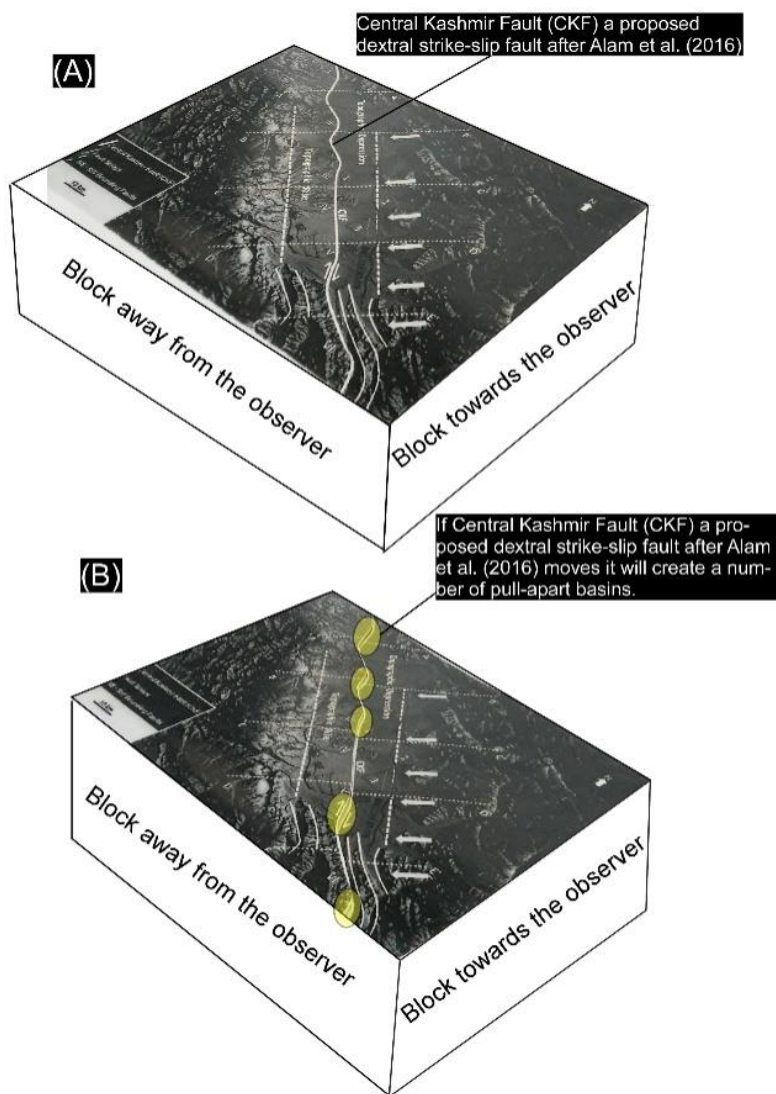
Figure 5. (A) The actual trace of CKF after (Alam et al., 20150[15]. (B) A range of small pull-apart basins expected to form if CKF moves.

reported topographic break or offset with a sufficient amount of slip required relative to the width and length of the Kashmir basin. There is also no evidence of a large scale strike-slip displacement of bedrock units[3].

The horsetail thrust structures (actually imbricate fans) of Alam et al.[15] run parallel with the trend of the main fault trace (**Figure 4**) while they should be at angles to it if the fault was a dextral-slip fault. It is kinematically unlikely to have them on both sides of a major fault tip (**Figure 4**). It is equally unreasonable to have the trace of a major strike-slip fault in the middle of a pull-apart basin (**Figure 2**). The structures mapped by Alam et al.[15] are inconsistent with the orientation of a

major dextral-strike-slip fault system and the associated imbricate fans cannot be possible with the proposed orientation of the CKF (**Figure 3** and **Figure 4**).

The examination of GPS data in Kashmir Himalaya[17] shows an oblique faulting pattern, wherein a range-normal convergence of 11±1 mm/y is associated with a dextral-shear slip of 5±1 mm/y (**Figure 1**). When GPS data is resolved on the proposed CKF of Alam et al.[15] it shows dominant normal convergence and no shearing parallel to the strike of this fault. This clearly suggests that such a structure cannot be an active major strike-slip fault (**Figure 1**). The structural architecture and the evidences presented above

suggest that Kashmir basin does not require a major strike-slip fault. The structures that have been shown in the pull-apart paper model indicate that such a big structure is not possible in Kashmir basin. Thus, the geological and tectonic setting of Kashmir basin is largely consistent with a piggy-back model [8].

Acknowledgements

References

[1] R. Vassallo, J.L. Mugnier, V. Vignon, M.A. Malik, M. R. Jayangondaperumal, and P. Srivastava, *J., Earth Planet. Sc. Lett.,* **2015**, 411, 241-252.

[2] V.C. Thakur, R. Jayangondaperumal, and M.A. Malik, *Tectonophysics*, **2010**, 489, 29–42.

[3] D.W. Burbank and G.D. Johnson, *Palaeogeogr. Palaeoclimatol. Palaeoecol.,* **1983**, 43, 205-235.

[4] A. A. Shah, *Geomorphology*, **2016**, 253, 553-557.

[5] N. Basavaiah, E. Appel, B.V. Lakshmi, K. Deenadayalan, K.V.V. Satyanarayana, S. Misra, N. Juyal, and M. A. Malik, 2010. *Journal of Geophysical Research*, **2010**, 115(B8)

[6] D.K. Bhatt, *Himal. Geol.*, **1979**, 6, 197-208.

[7] D.K. Bhatt, *Geological Survey of India,* 1976, 24,188–204.

[8] D.W. Burbank and G.D. Johnson, G.D, *Nature,* **1982,** 298, 432-436.

[9] C.S. Middlemiss, *Geol. Surv. India.*, **1910,** 40, 206–260.

[10] I.A. Farooqi, and R.N. Desai, *J. Geol. Surv. India.*, **1974,** 15, 299-305.

[11] A. Shabir, and M.I. Bhat, M.I, *Himal. Geol.*, **2012**, 33,162-172.

[12] A. A. Shah, *Int. J. Earth. Sci.*, **2013a**, 102, 7, 1957-1966.

[13] A.A. Shah, *Inte Int. J. Earth. Sci.*, **2015a,** 104, 1901-1906.

[14] A.A. Shah, *Geol. Soc. Amer. Spl. Papers.*, **2016,** 520, 520-28.

[15] A. Alam, S, Ahmad, M.S. Bhat, and B. Ahmad, *Geomorphology*, **2015**, 239, 114-126.

[16] A. Alam, S, Ahmad, M.S. Bhat, and B. Ahmad, *Geomorphology*, **2016**, 253, 558-563.

[17] C. Schiffman, Bikram Singh Bali, Walter Szeliga, and Roger Bilham., *Geophy. Res. Lett*., **2013**, 40, 5642-5645.

[18] L. Bollinger, S.N. Sapkota, P. Tapponnier, Y. Klinger, M. Rizza, J. Van der Woerd, and S Bes de Berc., *J. Geophys. Res*, **2014**, 119, 7123-7163.

[19] J.N. Malik, A. A. Shah, S.P. Naik, S. Sahoo, K. Okumura and N.R. Patra, *Current Science*, **2014**, 106, 229.

[20] J.N. Malik, A.A. Shah, A. Sahoo, K., Puhan, B., Banerjee, C., Shinde, D. P., and Rath, T*ectonophysics*, **2010,** 483, 327-343.

[21] A.G. Sylvester, *Geol. Soc. Am. Bull.*, **1988**, 100, 1666–1703.

[22] A.A. Shah, *PATA days*, **2013b,** 5, 112.

[23] P. Tapponnier, and P. Molnar, *Nature,* **1976**, 264, 319-324.

Heat transfer detraction for conjugate effect of Joule heating and magneto-hydrodynamics on mixed convection in a lid-driven cavity along with a heated hollow circular plate

S.K. Farid[1], Uddin M. Sharif[2], M.M. Rahman[3]* and Yeo Wee Ping[3]

[1]Mirpur Girls Ideal Laboratory Institute, Mirpur-10, Dhaka-1216, Bangladesh
[2]Department of Mathematics, Jahangirnagar University, Savar, Dhaka, Bangladesh
[3]Mathematical and Computing Sciences Group, Faculty of Science, Universiti Brunei Darussalam, Jalan Tungku Link, Gadong, BE 1410, Brunei Darussalam

*corresponding author email: mustafizur.rahman@ubd.edu.bn

Abstract

In this paper, the influence of Joule heating and magneto-hydrodynamics on mixed convection in a lid-driven cavity along with a heated hollow circular plate placed at the centre of the square cavity is investigated. The governing equations which are derived by considering the effects of both Joule heating and magneto-hydrodynamics are solved via the penalty finite-element method with the Galerkin-weighted residual technique. The effects of the Richardson number and Hartmann number arising from the MHD and Joule heating on the flow and heat transfer characteristics have been examined. The results show that the flow behavior, temperature distribution and heat transfer inside the cavity are strongly affected by the presence of the magnetic field. On the other hand, only the temperature distribution and heat transfer inside the cavity are strongly affected by the Joule heating parameter. The results also show that if the Hartmann number is increased from 5 to 100 then the heat transfer detraction is 20%, and if the Joule heating parameter is increased from 1 to 5 then the heat transfer detraction is 58%. In addition, multiple regressions among the various parameters are obtained.

Index Terms: mixed convection, finite element method, lid-driven cavity, circular hollow plate, heat transfer detraction

1. Introduction

Mixed convection in a closed enclosure is a topic that has been studied extensively by researchers, especially those concerned with lid-driven cavity problems. This is because the topic has many applications in engineering and natural phenomena such as solar energy storage, growth of crystals, heat exchangers, cooling of electronic devices, food processing, atmospheric flows and drying technologies[1-5]. There are many research papers concerned with mixed convection in a lid-driven cavity, and some of them are described in what follows. Oztop and Dagtekin[6] numerically investigated mixed convection in a two-sided lid-driven differentially heated square enclosure. Moallemi and Jang[7] carried out a numerical investigation on the effects of Prandtl number on laminar mixed convection in a lid-driven cavity. Prasad and Koseff[8] experimentally investigated mixed convection in a deep lid-driven cavity. Khanafer and Chamkha[9] analyzed mixed convection in a lid-driven cavity that is filled with a fluid-saturated porous medium. Ji et al.[10] conducted a numerical and experimental investigation of mixed convection in a sliding lid-driven cavity. Sharif[11] studied mixed convection in shallow inclined driven enclosure with a top-heated moving lid and cooled from below. Oztop et al.[12] investigated mixed convection in lid-driven cavities with a solid vertical partition. Basak et al.[13] investigated mixed convection between linearly heated side walls in a lid-driven porous

Nomenclature

B_0	magnetic induction ()		V	dimensionless vertical velocity component
c_p	specific heat (J kg^{-1} k^{-1})		V_0	lid velocity(ms^{-1})
D	diameter of the inner plate		x	horizontal coordinate (m)
g	gravitational acceleration (ms^{-2})		X	dimensionless horizontal coordinate
Gr	Grashof number		y	vertical coordinate (m)
H	enclosure height (m)		Y	dimensionless vertical coordinate
Ha	Hartmann number			
k	thermal conductivity (Wm^{-1} k^{-1})		*Greek symbols*	
K	solid fluid thermal conductivity ratio		α	thermal diffusivity (m^{2}s^{-1})
J	Joule heating parameter		β	thermal expansion coefficient (K^{-1})
L	length of the enclosure (m)		μ	dynamic viscosity (kg m^{-1} s^{-1})
Nu	Nusselt number		v	kinematic viscosity (m^2 s^{-1})
p	dimensional pressure (kg m^{-1} s^{-2})		θ	non-dimensional temperature
P	dimensionless pressure		ψ	streamfunction
Pr	Prandtl number		ρ	fluid density (kg m^{-3})
Re	Reynolds number		*Subscripts*	
Ri	Richardson number		av	average
T	fluid temperature (K)		h	heat source
u	horizontal velocity component (ms^{-1})		c	cold
U	dimensionless horizontal velocity component		f	fluid
v	vertical velocity component (ms^{-1})		s	solid

square enclosure. Sivasankaran et al.[14] performed a numerical investigation of mixed convection in a lid-driven enclosure with non-uniform heating on both sidewalls. Kalteh et al.[15] carried out a numerical investigation of steady laminar mixed convection in a nanofluid-filled lid-driven square enclosure with a triangular heat source. They revealed that the average Nusselt number can be increased by increasing the value of Reynolds number and decreasing the height of the heat source. Ismael et al.[16] numerically studied steady laminar mixed convection in a water-filled square enclosure. They observed that convection was reduced at the critical values obtained for the partial slip parameter. In addition, the partial slip parameter had an insignificant effect on convection in the enclosure.

Magneto-hydrodynamics (MHD) is nowadays an important field of study that is widely known for its usage in industrial applications such as metal casting, microelectronic devices, liquid metal cooling blankets for fusion reactors, turbulence control, crystal growth and heat and mass transfers control[4,17]. Some of the literature reviews concerned with MHD are as follows. Chamkha[1] performed a numerical investigation of hydromagnetic mixed convection with internal heat generation or absorption in a vertical lid-driven enclosure. Al-Salem et al.[4] numerically studied the effects of the moving top wall direction on MHD mixed convection in a square enclosure with a linearly heated bottom wall. They found out that when the magnetic field is increased, it reduces the heat transfer and the flow

intensity inside the cavity. Ahmed et al.[5] performed a numerical investigation of laminar MHD mixed convection in an inclined lid-driven square enclosure with an opposing thermal buoyancy force and sinusoidal temperature distributions on both vertical walls. They observed that increasing the Hartmann number resulted in an increasing heat transfer rate along the heated walls as well. Piazza and Ciofalo[18] numerically investigated MHD natural convection in a liquid-metal filled cubic cavity. Sankar et al.[19] carried out an investigation of natural convection in the presence of a magnetic field in a vertical cylindrical annulus. Kahveci and Oztuna[20] performed an investigation of MHD natural convection in a cavity in the presence of a heated partition. Sarries et al.[21] conducted a numerical investigation of MHD free convection in a laterally and volumetrically heated square enclosure. Oztop et al.[22] numerically studied MHD buoyancy-induced flow in a non-isothermally heated square cavity. Rahman et al.[23] carried out a numerical investigation of the conjugate effect of Joule heating and MHD mixed convection in an obstructed lid-driven square enclosure. They found that the strength of the magnetic field determines the heat transfer and fluid flow in the enclosure. Rahman et al.[24] numerically investigated the conjugate effect of Joule heating and MHD on double-diffusive mixed convection in a horizontal channel with an open enclosure. They observed that the Hartmann number has a considerable effect on the streamlines, isothermal lines, concentration and density contours. In addition, increasing the Hartmann number resulted in a decrease in the average Nusselt number at the heat source. Oztop et al.[25] conducted a numerical investigation of MHD laminar mixed convection in a lid-driven square enclosure with a corner heater. They revealed that increasing the Hartmann number resulted in a decrease in the heat transfer. This means that the magnetic field is an important parameter that controls the heat transfer and fluid flow in the enclosure. Sivasankaran et al.[26] carried out a numerical study of the effects of the sinusoidal boundary temperatures at the sidewalls on mixed convection in a lid-driven square enclosure in the presence of a magnetic field. They

observed that the presence of the magnetic field largely determined the heat transfer and fluid flow in the enclosure. Farid et al.[27] numerically investigated MHD mixed convection in a lid-driven enclosure with a heated circular hollow cylinder placed at the centre. They discovered that increasing the Hartmann number caused the velocity of the flow to decrease thus resulting in decreases in the heat transfer and fluid flow intensity as well. Rahman et al.[28] conducted a numerical study of MHD mixed convection in an open channel with a fully or partially heated square enclosure. Selimefendigil and Oztop[29] performed a numerical investigation of MHD mixed convection in a partially heated right-angled triangular cavity, with an insulated rotating cylinder and filled with Cu-water nanofluid. They observed that the magnetic field caused the convection heat transfer to slow down and increasing the Hartmann number caused both the total entropy generation and the local and averaged heat transfer to decrease. Selimefendigil and Oztop[30] numerically investigated MHD mixed convection in a lid-driven square cavity filled with nanofluid in a presence of a rotating cylinder. They found that the convective heat transfer and velocity field were slowed down by the magnetic field. Thus, increasing the Hartmann number caused the average heat transfer to decrease. In addition, the magnetic field acted as a parameter controlling the local heat transfer.

The Joule heating parameter has received a considerable amount of attention lately, in particular in relation to MHD problems. Rahman et al.[23] carried out a numerical investigation of the conjugate effect of Joule heating and MHD mixed convection in an obstructed lid-driven square enclosure. They discovered that the Joule heating parameter has considerable influence on the streamlines and isotherms. Rahman et al.[24] numerically investigated the conjugate effect of Joule heating and MHD on double-diffusive mixed convection in a horizontal channel with an open enclosure. They observed that the Joule heating parameter has an insignificant influence on the streamlines and concentration contours, but has considerable influence on the isotherms and density contours. Barletta and Celli[31] analyzed the

effects of Joule heating and viscous dissipation on MHD mixed convection in a vertical channel. Mao et al.[32] carried out an investigation of Joule heating in MHD flows in channels with thin conducting walls. Parvin and Hossain[33] studied the conjugate effect of Joule heating and a magnetic field on mixed convection in a lid-driven enclosure with an undulated bottom surface. Ray and Chatterjee[34] conducted a numerical investigation of MHD mixed convection in a horizontal lid-driven square enclosure with a circular solid object located at the centre and corner heaters with Joule heating. They found out that the Joule heating parameter only has a minor effect on the overall flow field inside the enclosure. Azad et al.[35] performed a numerical investigation of the effects of Joule heating on the magnetic field and mixed convection inside a channel along with a cavity. Their results indicated that a higher Joule heating parameter resulted in reduced heat transfer. In addition, enhancing the Joule heating parameter caused the exit temperature to increase. Raju et al.[36] investigated MHD convective flow through a porous medium in a horizontal channel with an insulated and impermeable bottom wall in the presence of viscous dissipation and Joule heating.

The main purpose of the present investigation is to examine the heat transfer detraction for conjugate effect of Joule heating and magneto-hydrodynamics on mixed convection in a lid-driven cavity along with a heated circular plate placed at the centre of the square enclosure for different values of the Hartmann number, Richardson number and Joule heating parameter.

2. Problem Formulation
2.1. Physical Modeling
Figure 1 shows the computational domain of the enclosure considered in the study and the associated coordinate system. Here L and H represent the width and height of the enclosure respectively. The aspect ratio of the length to its height of the enclosure is unity, representing a square enclosure. In addition, D represents the diameter of the inner plate ($D = 0.2L$) and it is located at the center of the enclosure. The hollow plate is kept at a constant high temperature T_h. The

vertical walls of the enclosure are kept in a constant low temperature T_c, while the horizontal walls are adiabatic. The right vertical wall of the enclosure is moving upwards with constant velocity V_0 in its own plane. A uniform magnetic field with constant magnitude B_0 is applied horizontally, normal to the y-axis. Joule heating is also applied to the enclosure. The radiation, pressure work and viscous dissipation are all negligible. A no-slip boundary condition is imposed on all the walls of the enclosure and the plate surface.
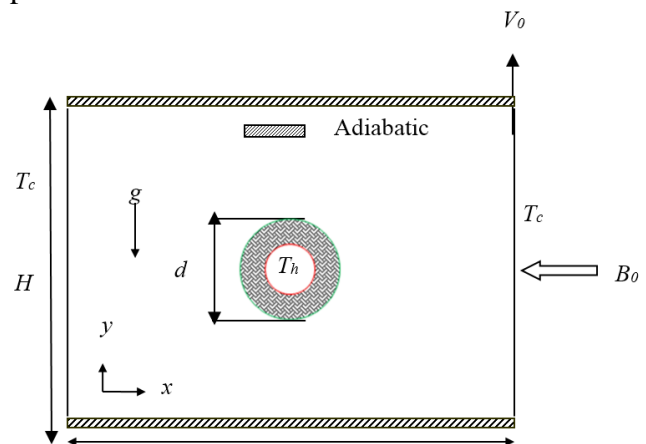
Figure 1. Schematic diagram of the physical model

2.2. Mathematical Formulation
With the following dimensionless variables:

$$X = \frac{x}{L}, \ Y = \frac{y}{L}, \ U = \frac{u}{V_0}, \ P = \frac{p}{\rho V_0{}^2},$$
$$\theta = \frac{(T - T_c)}{(T_h - T_c)}, \ \theta_s = \frac{(T_s - T_c)}{(T_h - T_c)}$$

the dimensionless forms of the governing equations for laminar, steady mixed convection based on the standard laws of conservation of mass, momentum and energy in the presence of hydromagnetic effects and Joule heating are given as:

$$\frac{\partial U}{\partial X} + \frac{\partial V}{\partial Y} = 0 \tag{1}$$

$$U \frac{\partial U}{\partial X} + V \frac{\partial U}{\partial Y} = -\frac{\partial P}{\partial X} + \frac{1}{Re}\left(\frac{\partial^2 U}{\partial X^2} + \frac{\partial^2 U}{\partial Y^2}\right) \tag{2}$$

$$U \frac{\partial V}{\partial X} + V \frac{\partial V}{\partial Y} = -\frac{\partial P}{\partial Y} + \frac{1}{Re}\left(\frac{\partial^2 V}{\partial X^2} + \frac{\partial^2 V}{\partial Y^2}\right) + Ri\,\theta - \frac{Ha^2}{Re}V \tag{3}$$

$$U \frac{\partial \theta}{\partial X} + V \frac{\partial \theta}{\partial Y} = \frac{1}{Re\,Pr}\left(\frac{\partial^2 \theta}{\partial X^2} + \frac{\partial^2 \theta}{\partial Y^2}\right) + J V^2 \tag{4}$$

For the solid region: $\dfrac{\partial^2 \theta_s}{\partial X^2} + \dfrac{\partial^2 \theta_s}{\partial Y^2} = 0$ (5)

where

$$Re = V_0 L/\upsilon, Gr = g\beta\Delta T L^3/\upsilon^2, \ Ha^2 = \sigma B_0^2 L^2/\mu,$$

$$Pr = v/\alpha, Ri = Gr/Re^2, J = \sigma B_0^2 L V_0/\rho C_p \Delta T$$

(here $\Delta T = T_h - T_c$ and $\alpha = k/\rho C_p$ are   the temperature difference and thermal diffusivity respectively) are the Reynolds number, Grashof number, Hartmann number, Prandtl number, Richardson number, and Joule heating parameter respectively.

The dimensionless boundary conditions for the problem under consideration can be written as follows:

At the left wall: $U = 0, V = 0, \ \theta = 0$

At the right vertical wall: $U = 0, V = 1, \theta = 0$

At the top and bottom walls: $U = 0, \ V = 0, \ \dfrac{\partial \theta}{\partial N} = 0$

At the inner surface of the hollow cylinder: $U = 0, V = 0, \theta = 1$

At the outer surface of the hollow cylinder: $\left(\dfrac{\partial \theta}{\partial N}\right)_{fluid} = K\left(\dfrac{\partial \theta_s}{\partial N}\right)_{solid}$

where N is the non-dimensional distance in either the X or Y direction acting normal to the surface, and $K = k_s/k_f$ is the thermal conductivity ratio.

The average Nusselt number at the heated hollow cylinder in the cavity, based on the conduction contribution, may be expressed as

$$Nu_{av} = -\dfrac{2}{\pi}\int_0^\pi \dfrac{\partial \theta}{\partial N} d\phi$$

And the average temperature in the cavity is defined as $\theta_{av} = \int \theta \, d\bar{V}/\bar{V}$, where $\bar{V}$ is the cavity volume.

The fluid motion is displayed using the stream function (ψ) obtained from velocity components U and V. The relationship between the stream function and the velocity components for a two-dimensional flow can be expressed as:

$$U = \dfrac{\partial \psi}{\partial Y}, \ V = -\dfrac{\partial \psi}{\partial X}$$

(6)

3. Numerical Scheme
3.1. Numerical Procedure
The solutions of the governing equations along with boundary conditions are solved through the Galerkin finite-element formulation[24]. The continuum domain is divided into a set of non-overlapping regions called elements. Six node triangular elements with quadratic interpolation functions for velocity as well as temperature and linear interpolation functions for pressure are utilized to discretize the physical domain. Moreover, interpolation functions in terms of local normalized element coordinates are employed to approximate the dependent variables within each element. Substitution of the obtained approximations into the system of the governing equations and boundary conditions yields a residual for each of the conservation equations. These residuals are reduced to zero in a weighted sense over each element volume using the Galerkin method. The resultant finite-element equations are nonlinear. These nonlinear algebraic equations are solved employing the Newton-Raphson iteration technique.

3.2. Grid Independency Test and Code Validation
To establish the appropriate grid size, several grid size sensitivity tests were conducted in this geometry to determine the sufficiency of the mesh scheme and to make sure that the solutions are grid independent. The grid independent test are conducted for $Ri = 1$, $Ha = 10$ and $J = 0.5$ in the square lid-driven enclosure. Five different non-uniform grid systems with the following numbers of elements within the resolution field – 4032, 5794, 6116, 7270 and 8599 – are examined. In order to develop an understanding of the effects of the grid fineness, the average Nusselt number was calculated for each grid system as shown in *Figure 2*. The size of Nu_{av} for 8599 elements shows little difference from the results obtained for the other elements. However, the grid independency test showed that a grid of 8599 elements is enough for the desired accuracy of the results.
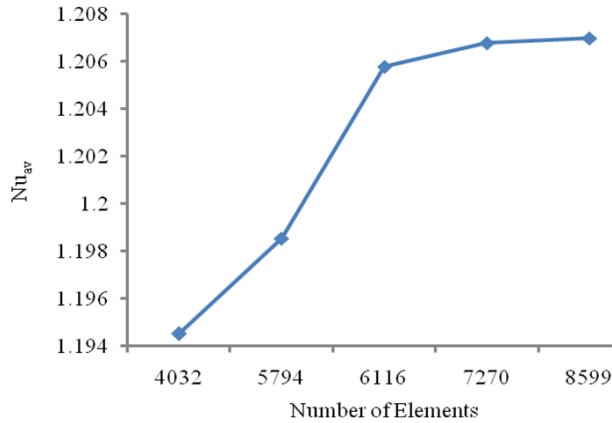
Figure 2. Grid independency study for average Nusselt number with $Ha = 10$, $J = 0.5$ and $Ri = 1$.

Table 1. Comparison of the present data with of Chamkha[1] for Ha

Parameter	Present study	Chamkha[1]
Ha	Nu	Nu
0.0	2.206915	2.2692
10.0	2.113196	2.1050
20.0	1.820612	1.6472
50.0	1.18616	0.9164

To verify the accuracy of the numerical results and the validity of the mathematical model obtained in the present study, comparisons with the previously published results are necessary. But owing to the lack of availability of experimental data on the particular problem with its associated boundary conditions investigated here, validation of the predictions could not be done against experiment. However, the present numerical model can be compared with the documented numerical study of Chamkha[1]. The present numerical code was validated against the problem of mixed convection in a lid-driven enclosure studied by Chamkha[1], which was investigated using a finite volume approach. The left wall moved upward with a fixed velocity and maintained in a cooled state. The right wall was heated whereas the two horizontal walls are adiabatic. We use the same boundary condition and wall temperatures on the horizontal walls of the cavity. We compared the results for average Nusselt number (at the hot

wall) between the outcomes of the present code as shown in **Table 1**. From the comparison it can be observed that the results of present simulation agree well with the results of Chamkha[1].

4. Results and Discussion
In this paper, a numerical investigation has been carried out to study the conjugate effect of Joule heating and magneto hydrodynamics on mixed convection in a lid-driven square cavity along with a heated hollow plate. The governing parameters used are the Hartmann number ranging from $5 \leq Ha \leq 100$, the Richardson number ranging from $0.1 \leq Ri \leq 5$ and the Joule heating parameter ranging from $1 \leq J \leq 5$. The Reynolds number, the solid fluid thermal conductivity ratio and the Prandtl number are fixed at $Re = 100$, $K = 5$ and $Pr = 0.71$. The numerical results are shown in the forms of streamlines, isotherms, average Nusselt number and average fluid temperature.

4.1. Effects of the Hartmann number
Figure 3 shows the effect of the Hartmann number on streamlines for $J = 0.5$ at different values of the Richardson number. In the forced convection dominated region at $Ri = 0.1$ and pure mixed convection dominated region at $Ri = 1$, the flow pattern and the flow strength are almost similar for all Ha values. In the forced and pure mixed convection dominated region for lower Ha values (= 5 and 20), a counter rotating cell appeared at the right corner which is generated by the moving right wall and as Ha increases to 50, the cell divided into two parts at which the cells then located near the top and bottom corner of the right wall. Both cells rotate in the same direction and have equal flow strength. When the Ha value increases to 100, the flow strength of the two cells decreases slightly from 0.02 to 0.01 in both forced and pure mixed convection dominated region. In the free convection dominated region at $Ri = 5$, the flow pattern changes dramatically for all Ha values. For the highest Ha value ($Ha = 100$), the two cells located at the right wall disappeared and four new cells are formed at the centre. All four cells rotate in the same direction. As Ha decreases to 50, two of the cells disappeared. The other two
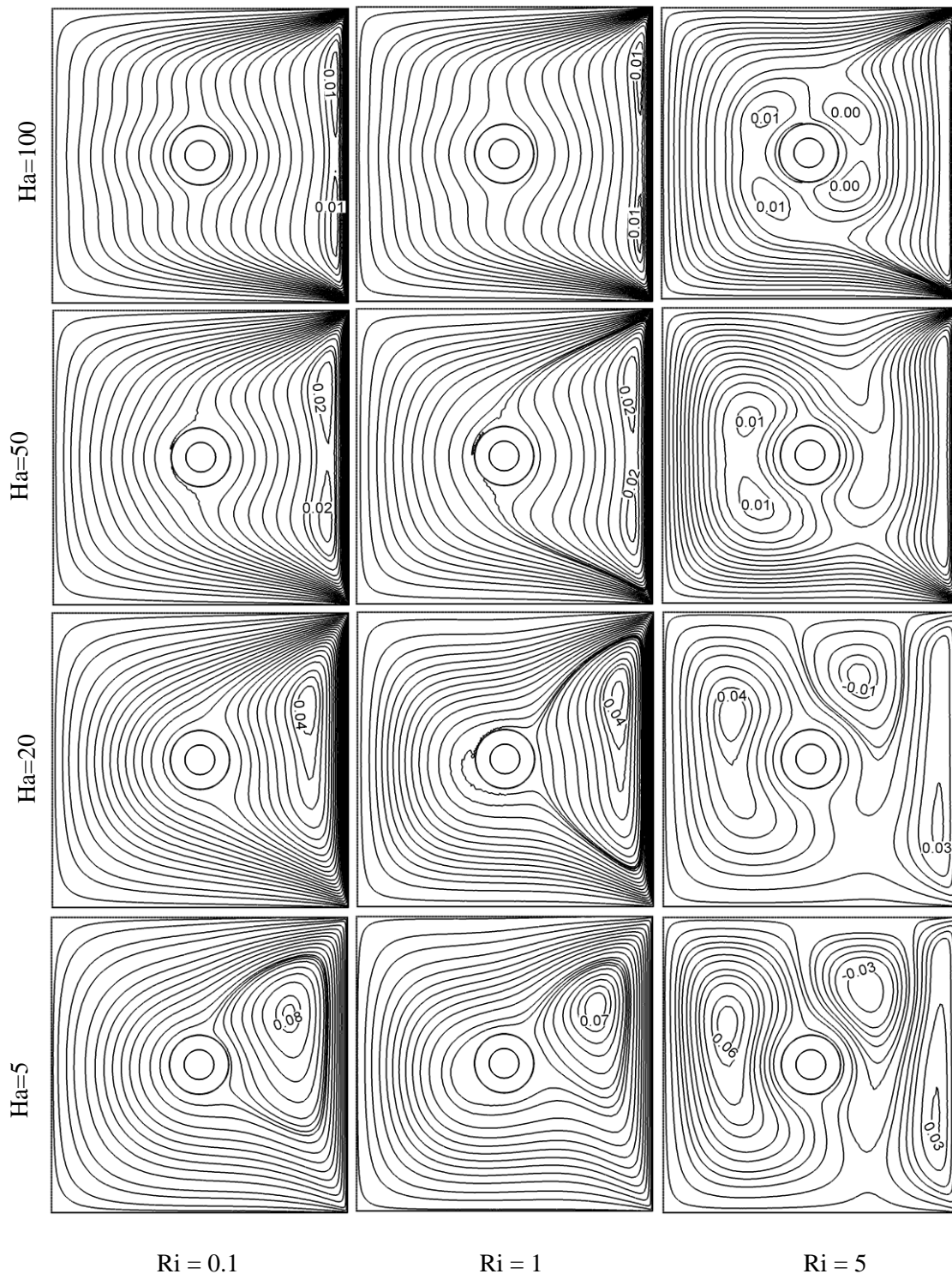
Figure 3. Effects of Hartman number and Richardson number on streamlines for $J = 0.5$.

cells which rotate counter clockwise remains at the centre near the left wall with equal flow strength. As *Ha* decreases to 20, multiple cells are formed. The two cells merge into one big cell which rotates counter clockwise and it is located near the left wall. Meanwhile, one cell is formed near the bottom corner of right wall which rotates counter clockwise and another cell is formed near the top right corner which rotates clockwise. At the lowest *Ha* value (*Ha* = 5), the pattern is more or less the same but with slightly higher flow strength.
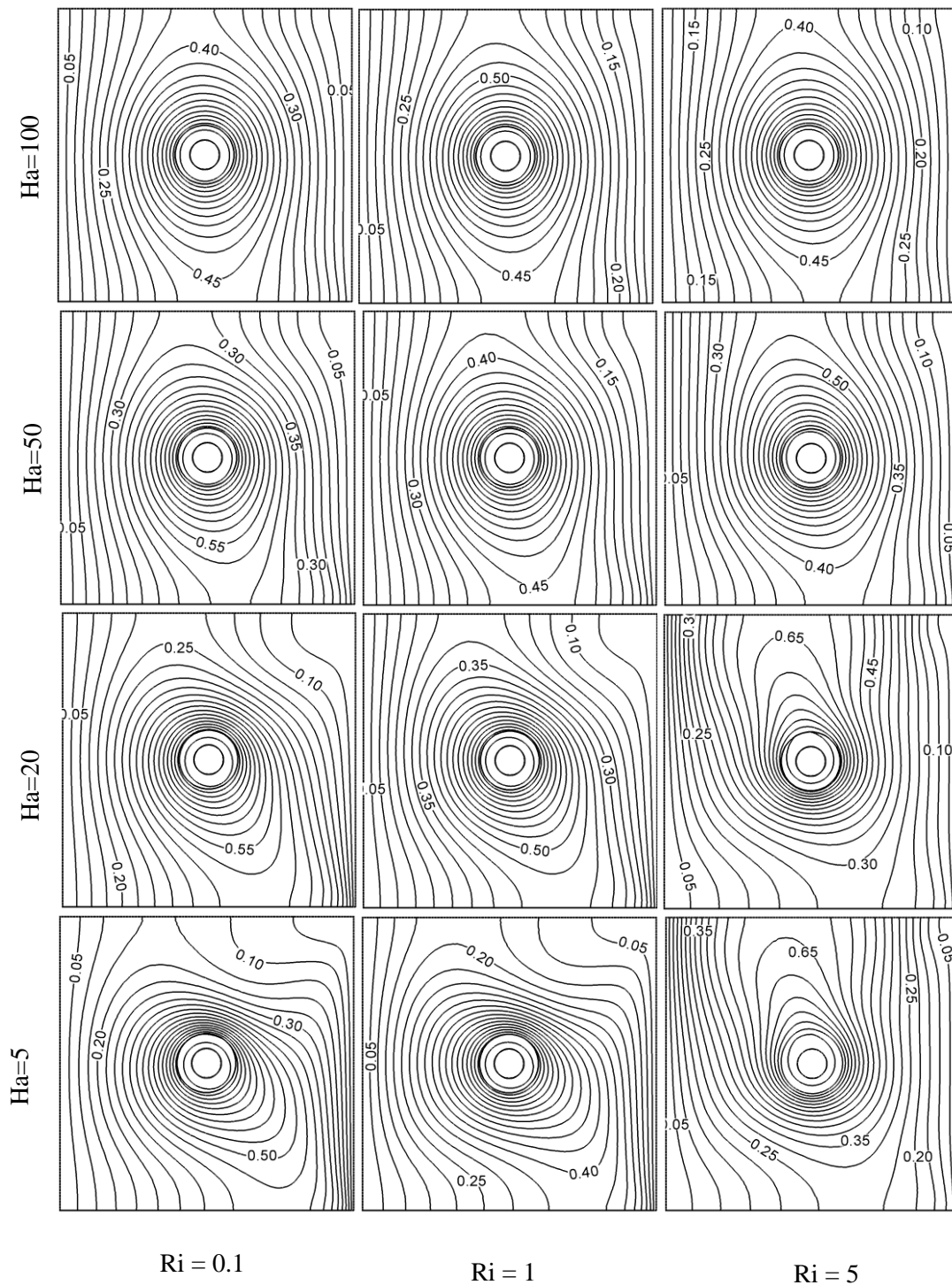
Figure 4. Effects of Hartman number and Richardson number on isothermal lines for $J = 0.5$.

The effect of Hartmann number on isotherms for $J = 0.5$ at different values of Richardson number is shown in ***Figure 4***. When $Ha = 50$ and 100, it can be seen that the isothermal lines is almost parallel to the vertical walls for all Ri values. This means that conduction heat transfer is the most active here. The isothermal lines near the vertical walls are almost similar at $Ri = 0.1$ and 1 for lower values of Ha (= 5 and 20) where convective distortion of isothermal lines takes place. Meanwhile for $Ri = 5$, although the isothermal lines are almost parallel to the vertical walls for higher Ha values (= 50 and 100), the isotherms changes as Ha decreases. The isothermal lines are

accumulated towards the upper left wall for lower *Ha* values (= 5 and 20) indicating a dominant influence of the convective heat transfer at *Ri* = 5. Another interesting change in the isotherms is found with the increase of the Hartmann number around the plate.

The effects of the Hartmann number on the average Nusselt number (Nu_{av}) at the hot surface with the Richardson number is presented in *Figure 5*. The average Nusselt number at first decreases as the *Ri* value increases in the forced convection dominated region for lower *Ha* values (= 5, 20 and 50), then around *Ri* = 2 it starts to increase slowly for *Ha* = 20 and 50 and very rapidly for *Ha* = 5. But for *Ha* = 100, the average Nusselt number keeps decreasing steadily as *Ri* increases. In addition, the highest average Nusselt number is achieved at the lowest *Ha* value (= 5).
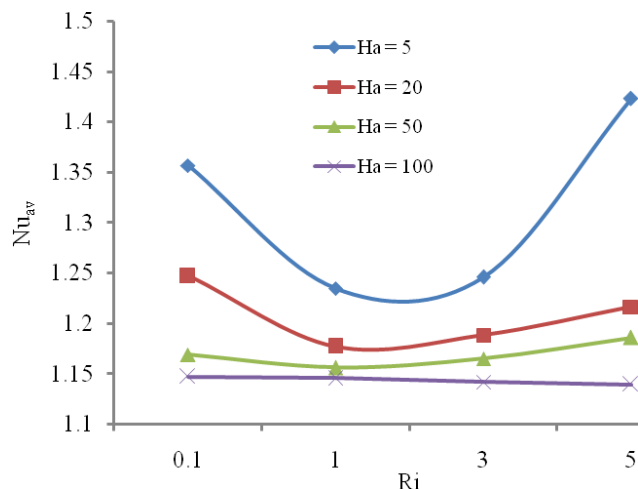
Figure 5. Effects of Hartman number and Richardson number on average Nusselt number for *J* = 0.5.

The effects of the Hartmann number on the average fluid temperature (θ_{av}) in the square enclosure with the Richardson number is presented in *Figure 6*. For *Ha* = 20 and 50, the average fluid temperature is almost constant in the forced convection dominated region with increasing *Ri* but in the natural convection dominated region , it increases slowly with increasing *Ri* and as it reaches *Ri* = 3, it starts to increase quickly. Meanwhile for *Ha* = 5, the average fluid temperature initially decrease in the forced convection dominated region as *Ri*

increases but at *Ri* = 1, it starts to goes up rapidly with increasing *Ri*. For *Ha* = 100, as *Ri* increases, the average fluid temperature is unstable as it keeps increasing then decreasing at some point before it starts to increase again. In addition, the following multiple regression for the average Nusselt number in terms of the Richardson number and the Hartmann number was obtained:

$$Nu_{av} = 0.0047Ri - 0.0014Ha + 1.2641$$
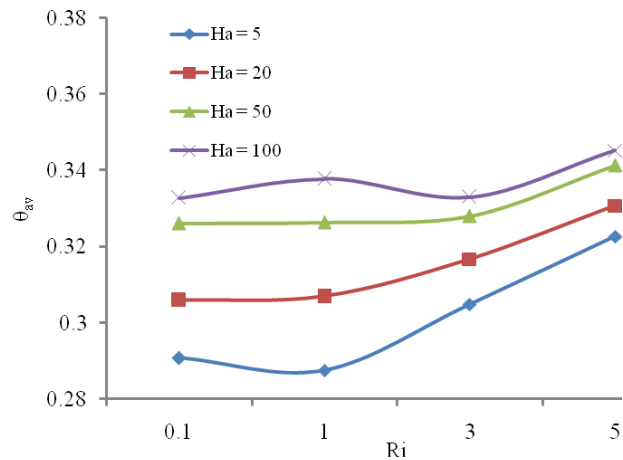
Figure 6. Effects of Hartman number and Richardson number on average fluid temperature for *J* = 0.5.

4.2. Effect of the Joule heating parameter

The effect of the Joule heating parameter on streamlines for *Ha* = 10 at different values of the Richardson number is shown in *Figure 7*. In the forced convection dominated region at *Ri* = 0.1 and pure mixed convection dominated region at *Ri* = 1, a counter rotating cell appeared at the right corner which is generated by the moving right wall for different *J* values In the forced and pure mixed convection dominated region, the flow pattern and the flow strength are almost similar for all values of *J* except that the cell near the right wall becomes much smaller in size in the pure mixed convection dominated region compared to the forced-convection dominated region. In the natural-convection dominated region at *Ri* = 5 for *J* = 1, the flow pattern is distorted. The previous cell is pushed towards the right wall and two new cells are formed. One counter-rotating cell is formed near the left wall which is the largest cell and another cell is formed near the top right corner which rotates clockwise. The flow pattern does
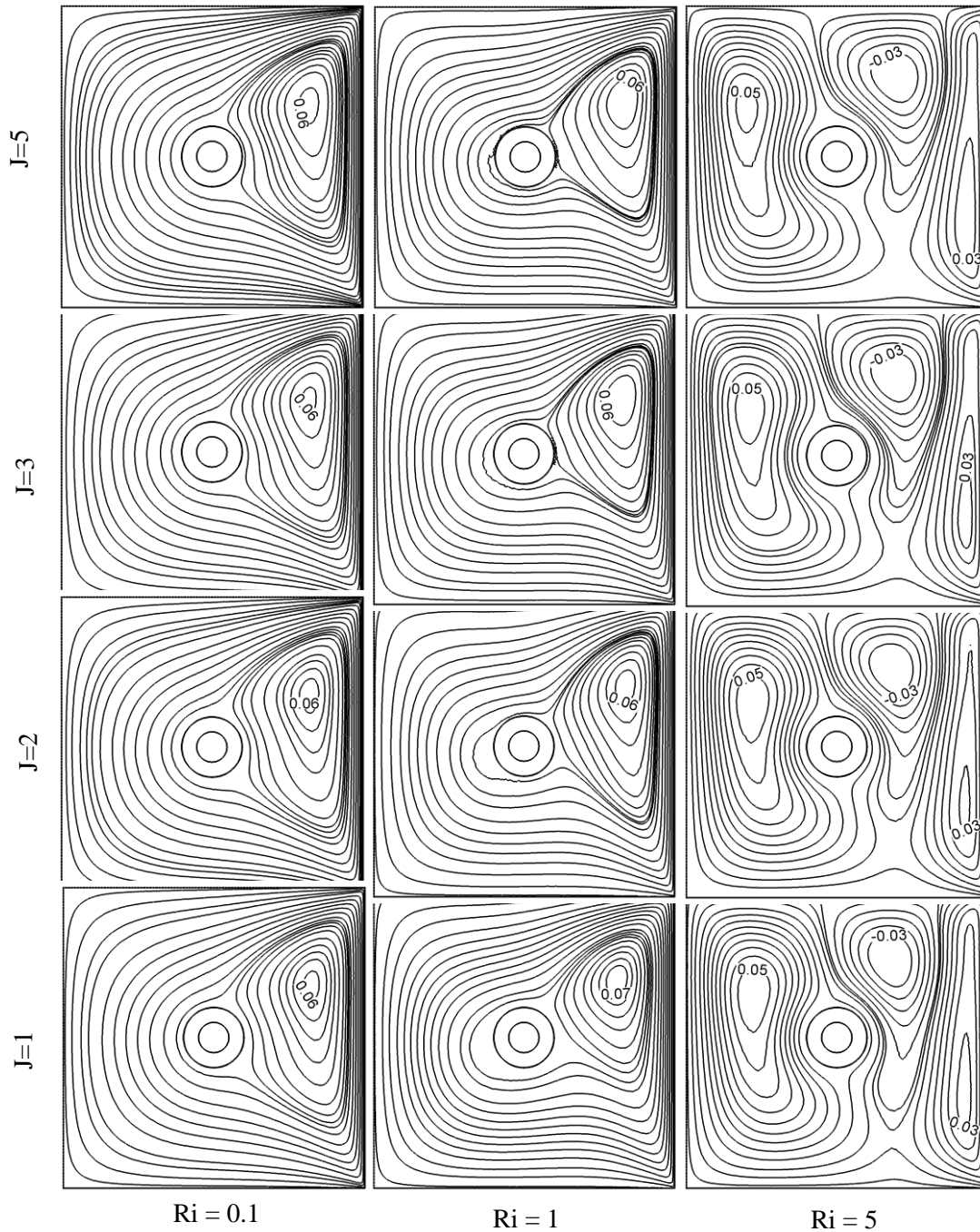
Figure 7. Effects of Joule heating parameter and Richardson number on streamlines for *Ha* = 10

not change much as the *J* values increase (*J* = 2, 3 and 5). Overall, this means that the Joule heating parameter has an insignificant effect on the streamlines.

Figure 8 shows the effect of Joule heating parameter on isotherms for *Ha* = 10 at different values of the Richardson number. In the forced

convection dominated region at *Ri* = 0.1 for lower values of *J* (=1 and 2), the isothermal lines reveals a convective distortion pattern, while for higher *J* values (=3 and 5) it can be seen that the isothermal lines are almost parallel to the vertical walls which means conductive heat transfer is active. In the pure mixed-convection dominated region at *Ri* = 1 and *J* = 1, conductive distortion of the isothermal
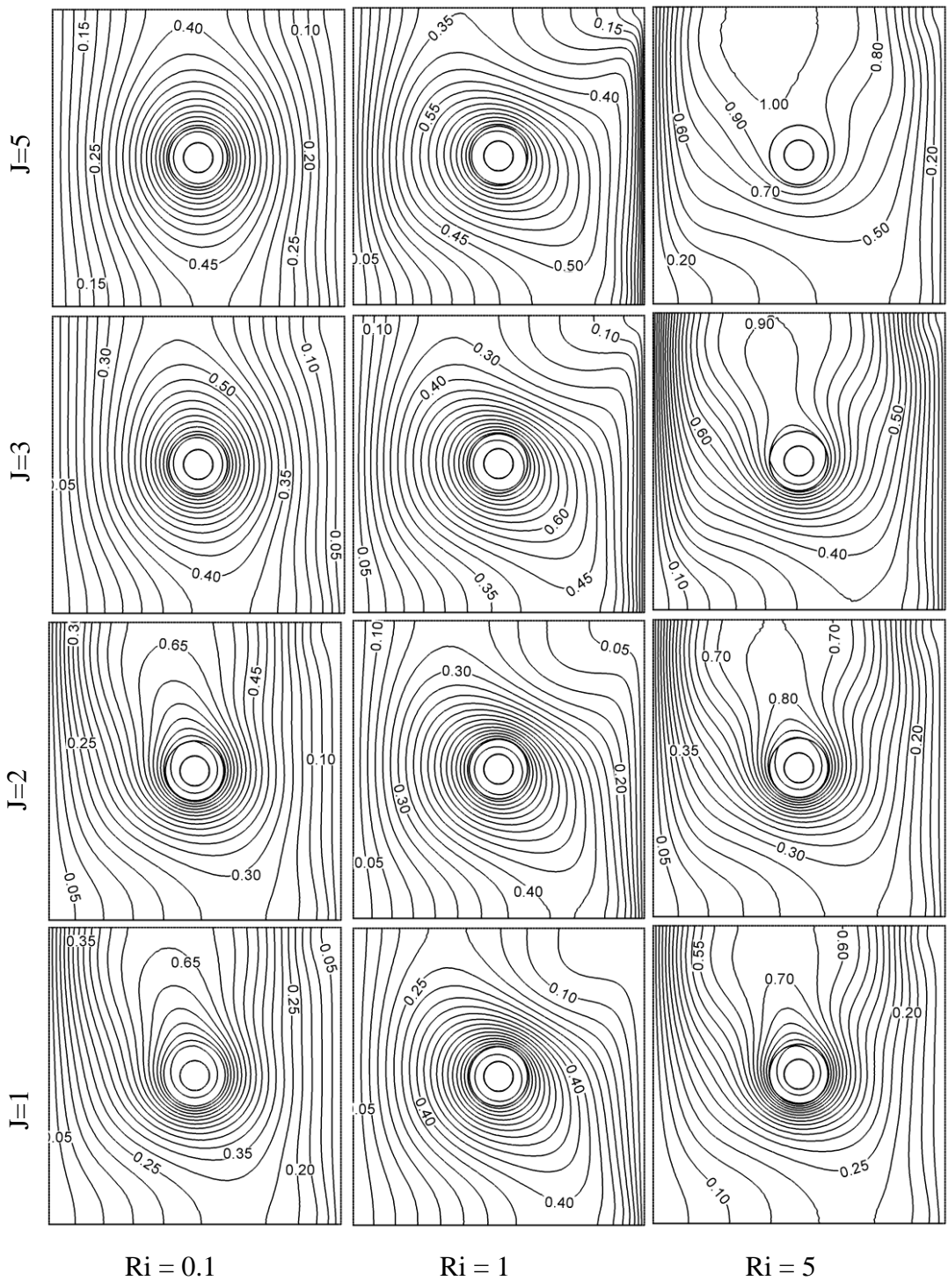
Figure 8: Effects of Joule heating parameter and Richardson number on isothermal lines for *Ha* = 10.

lines starts to appear near the top right corner. But it starts to disappear as the *J* values increase (for *J* = 2, 3 and 5) and the convective current becomes active. In the natural-convection dominated region at *Ri* = 5, the isothermal lines accumulate towards the upper left wall for all values of *J*, indicating the dominant influence of convective heat transfer.

The effects of the Joule heating parameter on the average Nusselt number (Nu_{av}) at the hot surface with the Richardson number are presented in

Figure 9. For higher *J* values (= 3 and 5), the average Nusselt number continuously decreases as *Ri* increases. On the other hand, the average Nusselt number initially decreases with increasing *Ri*, and when it reaches *Ri* = 3 it starts to go up faster for *J* = 1, but for *J* = 2 it increases more slowly. In addition, the highest average Nusselt number is achieved at the lowest *J* value (= 1) and the lowest average Nusselt number occurred at the highest *J* value (= 5).
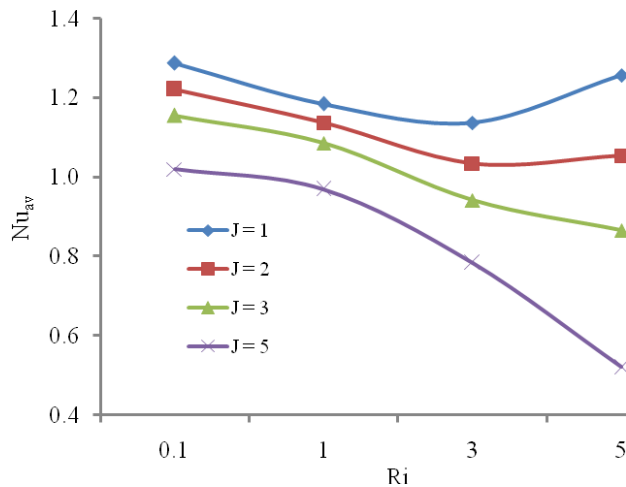
Figure 9. Effects of Joule heating parameters and Richardson number on average Nusselt number for *Ha* = 10

Figure 10 presents the effects of the Joule heating parameter on the average fluid temperature (θ_{av}) in the square enclosure with the Richardson number. The average fluid temperature decreases very slightly with increasing *Ri* for all *J* values in the forced-convection dominated region, whereas in the natural-convection dominated region it increases very rapidly with increasing *Ri* for all values of *J*. The highest average fluid temperature is obtained at the highest *J* value (= 5). In addition, the following multiple regression for the average Nusselt number in terms of the Richardson number and Joule heating parameter was obtained:

$$Nu_{av} = -0.0554Ri - 0.0999J + 1.4396$$
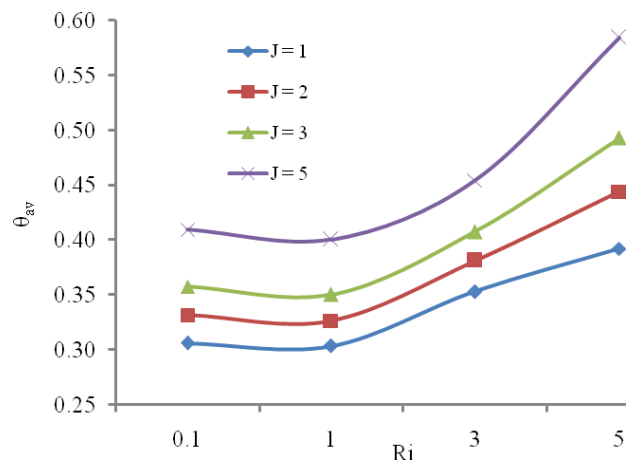
Figure 10. Effects of Joule heating parameters and Richardson number on average temperature for *Ha* = 10

5. Conclusion

MHD mixed convection in a lid-driven cavity with Joule heating and a heated hollow circular plate which is located at the centre of a square cavity has been numerically investigated over a wide ranges of various parameters such as the Hartmann number ($5 \leq Ha \leq 100$), Richardson number ($0.1 \leq Ri \leq 5$) and Joule heating parameter ($1 \leq J \leq 5$). From the investigation, the following conclusions can be made:

- The magnetic parameter (the Hartmann number) has a significant effect on reducing the size and strength of the inner vortex in the flow field for all values of *Ri*.
- A remarkable change in the isotherms around the plate is seen due as the Hartmann number increases for all *Ri*.
- The average Nusselt number declines and the average fluid temperature increases as the Hartmann number increases.
- The flow field is not influenced by the Joule heating parameter, but the isotherms near the plate are strongly influenced by *J* for all *Ri*.
- The average Nusselt number decreases and the average fluid temperature increases as the Joule heating parameter increases for all *Ri*.

References

[1] A. J. Chamkha, *Num. Heat Transfer*, **2002**, A 41, 529-546.

[2] U. Ghia, K. N. Ghia and C. T. Shin, *J. Comput. Phys.*, **1982**, 48, 387-411.

[3] M. C. Thompson and J. H. Ferziger, *J.Comput. Phys.*, **1989**, 82, 94-121.

[4] K. Al-Salem, H. F. Oztop, I. Pop and Y. Varol, *Int. J. Heat Mass Transfer*, **2002**, 55, 1103–1112.

[5] S. E. Ahmed, M. A. Mansour and A. Mahdy, *Nuclear Engineering Design*, **2013**, 265, 938-948.

[6] H. F. Oztop and I. Dagtekin, *Int. J. Heat Mass Transfer*, **2004**, 47, 1761-1769.

[7] M. K. Moallemi and K. S. Jang, *Int. J. Heat Mass Transfer*, **1992**, 35, 1881-1892.

[8] A. K. Prasad and J. R. Koseff, *Int. J. Heat Mass Fluid Flow*, **1996**, 17, 460-467.

[9] K. Khanafer and A. J. Chamkha, *Int. J. Heat Mass Transfer*, **1999**, 42, 2465-2481.

[10] T. H. Ji, S. Y. Kim and J. M. Hyun, *Int. J. Heat Mass Transfer*, **2007**, 43, 629-638.

[11] M.A.R. Sharif, *Appl. Therm. Eng.*, **2007**, 27, 1036-1042.

[12] H. F. Oztop, Z. Zhao and B. Yu, *Int. Comm. Heat Mass Transfer*, **2009**, 36, 661-668.

[13] T. Basak, S. Roy, S. K. Singh and I. Pop, *Int. J. Heat Mass Transfer*, **2010**, 53, 1819-1840.

[14] S. Sivasankaran, V. Sivakumar and P. Prakash, *Int. J. Heat Mass Transfer*, **2010**, 53, 4304-4315.

[15] M. Kalteh, K. Javaherdeh and T. Azarbarzin, *Powder Tech.*, **2014**, 253, 780-788.

[16] M. A. Ismael, I. Pop and A. J. Chamkha, *Int. J. Thermal Sciences*, **2014**, 82, 47-61.

[17] Z. Mehraz, A. E. Cafsi, A. Belghith and P. L. Quere, *J. Magnetism Magnetic Materials*, **2015**, 374, 214-224.

[18] I. D. Piazza and M. Ciofalo, *Int. J. Heat Mass Transfer*, **2002**, 45, 1477-1492.

[19] M. Sankar, M. Venkatachalappa and I. S. Shivakumara, *Int. J. Eng. Sci.*, **2006**, 44, 1556-1570.

[20] K. Kahveci and S. Oztuna, *Eur. J. Mech. B/Fluids*, **2009**, 28, 744-752.

[21] I. E. Sarries, S. C. Kakarantzas, A. P. Grecos and N. S. Vlachos, *Int. J. Heat Mass Transfer*, **2005**, 48, 3443-3453.

[22] H. F. Oztop, M. Oztop and Y. Varol, *Commun. Nonlinear Sci. Numer. Simul.*, **2009**, 14, 770-778.

[23] M. M. Rahman, M. A. Alim and M. M. A. Sarker, *Int. Comm. Heat Mass Transfer*, **2010**, 37, 524-534.

[24] M. M. Rahman, R. Saidur and N. A. Rahim, *Int. J. Heat Mass Transfer*, **2011**, 54, 3201-3213.

[25] H. F. Oztop, K. Al-Salem and I. Pop, *Int. J. Heat Mass Transfer*, **2011**, 54, 3494-3504.

[26] S. Sivasankaran, A. Malleswaran, J. Lee and P. Sundar, *Int. J. Heat Mass Transfer*, **2011**, 54, 512-525.

[27] S. K. Farid, M. M. Billah, M. M. Rahman and U. M. Sharif, *Procedia Eng.*, **2013**, 56, 474-479.

[28] M. M. Rahman, H. F. Oztop, R. Saidur, S. Mekhilef and K. Al-Salem, *Comp. Fluids*, **2013**, 79, 53-64.

[29] F. Selimefendigil and H. F. Oztop, *J. Taiwan Institute Chem. Eng.*, **2014**, 45, 2150-2162.

[30] F. Selimefendigil and H.F. Oztop, *Int. J. Heat Mass Transfer*, **2014**, 78, 741-754.

[31] A. Barletta and M. Celli, *Int. J. Heat Mass Transfer*, **2008**, 51, 6110-6117.

[32] J. Mao, S. Aleksandrova and S. Molokov, *Int. J. Heat Mass Transfer*, **2008**, 51, 4392-9.

[33] S. Parvin and N. F. Hossain, *J. Adv. Sci. Eng. Res.*, **2011**, 1, 210-23.

[34] S. Ray and D. Chatterjee, *Int. Comm. Heat Mass Transfer*, **2014**, 57, 200-207.

[35] A. K. Azad, M. M. Rahman and H. F. Oztop, *Procedia Eng.*, **2014**, 90, 389-396.

[36] K. V. S. Raju, T. S. Reddy, M. C. Raju, P. V. S. Narayana and S. Venkataramana, *Ain Shams Eng. J.*, **2014**, 5, 543-551.

An Introduction to Locally Convex Cones

Walter Roth*

Department of Mathematics, Faculty of Science, Universiti Brunei Darussalam, Jalan Tungku Link, Gadong, BE 1410, Brunei Darussalam

*corresponding author email: wroth@mathematik.tu-darmstadt.de

Abstract

This survey introduces and motivates the foundations of the theory of locally convex cones which aims to generalize the well-established theory of locally convex topological vector spaces. We explain the main concepts, provide definitions, principal results, examples and applications. For details and proofs we generally refer to the literature.

Index Terms: cone-valued functions, locally convex cones, Korovkin type approximation

1. Introduction

Endowed with suitable topologies, vector spaces yield rich and well-considered structures. Locally convex topological vector spaces in particular permit an effective duality theory whose study provides valuable insight into the spaces themselves. Some important mathematical settings, however – while close to the structure of vector spaces – do not allow subtraction of their elements or multiplication by negative scalars. Examples are certain classes of functions that may take infinite values or are characterized through inequalities rather than equalities. They arise naturally in integration and in potential theory. Likewise, families of convex subsets of vector spaces which are of interest in various contexts do not form vector spaces. If the cancellation law fails, domains of this type may not even be embedded into larger vector spaces in order to apply results and techniques from classical functional analysis. They merit the investigation of a more general structure.

The theory of locally convex cones as developed in [7] admits most of these settings. A topological structure on a cone is introduced using order-theoretical concepts. Staying reasonably close to the theory of locally convex spaces, this approach yields a sufficiently rich duality theory including Hahn-Banach type extension and separation theorems for linear functionals. In this article we shall give an outline of the principal concepts of this emerging theory. We survey the main results including some yet unpublished ones and provide primary examples and applications. However, we shall generally refrain from supplying technical details and proofs but refer to different sources instead.

2. Ordered cones and monotone linear functionals

A *cone* is a set P endowed with an addition

$$(a, b) \to a + b$$

and a scalar multiplication

$$(\alpha, a) \to \alpha a$$

for $a \in P$ and real numbers $\alpha \geq 0$. The addition is supposed to be associative and commutative, and there is a neutral element $0 \in P$, that is:

$$(a + b) + c = a + (b + c) \quad \text{for all } a, b, c \in P$$
$$a + b = b + a \quad \text{for all } a, b \in P$$
$$0 + a = a \quad \text{for all } a \in P$$

For the scalar multiplication the usual associative and distributive properties hold, that is:

$$\alpha(\beta a) = (\alpha\beta)a \quad \text{for all } \alpha, \beta \geq 0 \text{ and } a \in P$$

$(\alpha + \beta)a = \alpha a + \beta a$ for all $\alpha, \beta \geq 0$ and $a \in P$

$\alpha(a + b) = \alpha a + \alpha b$ for all $\alpha \geq 0$ and $a, b \in P$

$1a = a$ for all $a \in P$

$0a = 0$ for all $a \in P$

Unlike the situation for vector spaces, the condition $0a = 0$ needs to be stated independently for cones, as it is not a consequence of the preceding requirements (see [6]). The *cancellation law*, stating that

(C) $a + c = b + c$ implies that $a = b$

however, is not required in general. It holds if and only if the cone P can be embedded into a real vector space.

A *subcone Q* of a cone P is a non-empty subset of P that is closed for addition and multiplication by non-negative scalars.

An *ordered cone P* carries additionally a reflexive transitive relation $\leq$ that is compatible with the algebraic operations, that is

$a \leq b$ implies that $a + c \leq b + c$ and $\alpha a \leq \alpha b$

for all $a, b, c \in P$ and $\alpha \geq 0$. As equality in P is obviously such an order, all our results about ordered cones will apply to cones without order structures as well. We provide a few examples:

2.1 Examples. (a) In $\overline{\mathbb{R}} = \mathbb{R} \cup \{+\infty\}$ we consider the usual order and algebraic operations, in particular $\alpha + \infty = +\infty$ for all $\alpha \in \overline{\mathbb{R}}$, $\alpha \cdot (+\infty) = +\infty$ for all $\alpha > 0$ and $0 \cdot (+\infty) = 0$.

(b) Let P be a cone. A subset A of P is called *convex* if

$$\alpha a + (1 - \alpha)b \in A$$

whenever $a, b \in A$ and $0 \leq \alpha \leq 1$.We denote by $Conv(P)$ the set of all non-empty convex subsets of P. With the addition and scalar multiplication defined as usual by

$$A + B = \{a + b | a \in A \text{ and } b \in B\}$$

for $A, B \in Conv(P)$, and

$$aA = \{\alpha a | a \in A\}$$

for $A \in Conv(P)$ and $\alpha \geq 0$, it is easily verified that $Conv(P)$ is again a cone. Convexity is required to show that $(\alpha + \beta)A$ equals $\alpha A + \beta A$. The set inclusion defines a suitable order on $Conv(P)$ that is compatible with these algebraic operations. The cancellation law generally fails for $Conv(P)$.

(c) Let P be an ordered cone, X any non-empty set. For P-valued functions on X the addition, scalar multiplication and order may be defined pointwise. The set $F(X, P)$ of all such functions again becomes an ordered cone for which the cancellation law holds if and only if it holds for P.

A *linear functional* on a cone P is a mapping $\mu: P \to \overline{\mathbb{R}}$ such that

$$\mu(a + b) = \mu(a) + \mu(b) \quad \text{and} \quad \mu(\alpha a) = \alpha \mu(a)$$

holds for all $a, b \in P$ and $\alpha \geq 0$. Note that linear functionals take only finite values in invertible elements of P. If P is ordered, then μ is called *monotone* if

$a \leq b$ implies that $\mu(a) \leq \mu(b)$.

In various places the literature deals with linear functionals on cones that take values in $\mathbb{R} \cup \{-\infty\}$ (see [6]) instead. In vector spaces both approaches coincide, as linear functionals can take only finite values there, but in applications for cones the value $+\infty$ arises more naturally.

The existence of sufficiently many monotone linear functionals on an ordered cone is guaranteed by a Hahn-Banach type sandwich theorem whose proof may be found in [13] or in a rather weaker version in [7]. It is the basis for the duality theory of ordered cones. In this context, a *sublinear functional* on a cone P is a mapping $p : P \to \overline{\mathbb{R}}$ such that

$$p(\alpha a) = \alpha p(a) \quad \text{and} \quad p(a + b) \le p(a) + p(b)$$

holds for all $a, b \in P$ and $\alpha \ge 0$. Likewise, a *superlinear functional* on P is a mapping $q : P \to \overline{\mathbb{R}}$ such that

$$q(\alpha a) = \alpha q(a) \quad \text{and} \quad q(a + b) \ge q(a) + q(b)$$

holds for all $a, b \in P$ and $\alpha \ge 0$. Note that superlinear functionals can assume only finite values in invertible elements of P.

It is convenient to use the pointwise order relation for functions f, g on P; that is we shall write $f \le g$ to abbreviate $f(a) \le g(a)$ for all $a \in P$.

2.2 Sandwich Theorem (algebraic). *Let P be an ordered cone and let $p : P \to \overline{\mathbb{R}}$ be a sublinear and $q : P \to \overline{\mathbb{R}}$ a superlinear functional such that*

$$q(a) \le p(b) \quad \textit{whenever} \quad a \le b \quad \textit{for} \quad a, b \in P.$$

There exists a monotone linear functional $\mu : P \to \overline{\mathbb{R}}$ such that $q \le \mu \le p$.

Note that the above condition for q and p is fulfilled if $q \le p$ and if one of these functionals is monotone. The superlinear functional q may however not be omitted altogether (or equivalently, replaced by one that also allows the value $-\infty$) without further assumptions. (see Example 2.2 in [13].)

3. Locally convex cones

Because subtraction and multiplication by negative scalars are generally not available, a topological structure for a cone should not be expected to be invariant under translation and scalar multiplication. There are various equivalent approaches to *locally convex cones* as outlined in [7]. The use of *convex quasiuniform structures* is motivated by the following features of neighborhoods in a cone: With every $\overline{\mathbb{R}}$-valued monotone linear functional μ on an ordered cone P we may associate a subset

$$v = \{(a, b) \in P^2 \mid \mu(a) \le \mu(b) + 1\}$$

of P^2 with the following properties:

(U1) v is convex.
(U2)   If $a \le b$ for $a, b \in P$, then $(a, b) \in v$.
(U3)   If $(a, b) \in \lambda v$ and $(b, c) \in \rho v$ for $\lambda, \rho > 0$, then $(a, c) \in (\lambda + \rho)v$.
(U4)   For every $b \in P$ there is $\lambda \ge 0$ such that $(0, b) \in \lambda v$.

Any subset v of P^2 with the above properties (U1) to (U4) qualifies as a *uniform neighborhood* for P, and any family V of such neighborhoods fulfilling the usual conditions for a quasiuniform structure, that is:

(U5)   For $u, v \in V$ there is $w \in V$ such that $w \subset u \cap v$.
(U6) $\lambda v \in V$ for all $v \in V$ and $\lambda > 0$.

generates a *locally convex cone* (P, V) as elaborated in [7]. More specifically, V creates three hyperspace topologies on P and every $v \in V$ defines neighborhoods for an element $a \in P$ by

$$v(a) = \{b \in P \mid (b, a) \in \lambda v \text{ for all } \lambda > 1\}$$
in the *upper topology*
$$(a)v = \{b \in P \mid (a, b) \in \lambda v \text{ for all } \lambda > 1\}$$
in the *lower topology*
$$v(a)v = v(a) \cap (a)v$$
in the *symmetric topology*

However, it is convenient to think of a locally convex cone (P, V) as a subcone of a *full locally convex cone* $\tilde{P}$, i.e. a cone that contains the neighborhoods v as positive elements (see [7], Ch. I).

Referring to the order in $\tilde{P}$, the relation $a \in v(b)$ may be reformulated as $a \le b + v$. This leads to a second and equivalent approach to locally convex cones that uses the order structure of a larger full cone in order to describe the topology of P (for relations between order and topology we refer to [9]). Let us indicate how this full cone $\tilde{P}$ may be constructed (for details, see [7], Ch. I.5): For a fixed neighborhood $v \in V$ set

$$\tilde{P} = \{a \oplus \alpha v \mid a \in P, 0 \le a < +\infty\}.$$

We use the obvious algebraic operations on $\tilde{P}$ and the order

$$a \oplus \alpha v \leq b \oplus \beta v$$

if either $\alpha = \beta$ and $a \leq b$, or $\alpha < \beta$ and $(a, b) \in \lambda v$ for all $\lambda > \beta - \alpha$. The embedding $a \to a \oplus 0v$ preserves the algebraic operations and the order of P. The procedure for embedding a locally convex cone (P, V) into a full cone $(\tilde{P}, V)$ that contains a whole system V of neighborhoods as positive elements is similar and elaborated in Ch. I.5 of [7]. The quasiuniform structure of P may then be recovered through the subsets

$$\{(a, b) \in P^2 \mid a \leq b + v\} \subset P^2$$

corresponding to the neighborhoods $v \in V$.

We shall in the following use this order-theoretical approach: We may always assume that a given locally convex cone (P, V) is a subcone of a full locally convex cone $(\tilde{P}, V)$ that contains all neighborhoods as positive elements, and we shall use the order of the latter to describe the topology of P. The above conditions (U1) to (U6) for the quasiuniform structure on P equivalently translate into conditions involving the order relation of $\tilde{P}$ as follows:

(V1) $v \geq 0$ for all $v \in V$.
(V2)   For $u, v \in V$ there is $w \in V$ such that $w \leq u$ and $w \leq v$.
(V3) $\lambda v \in V$ whenever $v \in V$ and $\lambda > 0$.
(V4)   For $v \in V$ and every $a \in P$ there is $\lambda \geq 0$ such that $0 \leq a + \lambda v$.

Condition (V4) states that every element $a \in P$ is *bounded below*.

3.1 Examples. (a) The ordered cone $\overline{\mathbb{R}}$ endowed with the neighborhood system $V = \{\varepsilon \in \mathbb{R} \mid \varepsilon > 0\}$ is a full locally convex cone. For $a \in \mathbb{R}$ the intervals $(-\infty, a + \varepsilon]$ are the upper and the intervals $[a - \varepsilon, +\infty]$ are the lower neighborhoods, while for $a = +\infty$ the entire cone $\overline{\mathbb{R}}$ is the only upper neighborhood, and $\{+\infty\}$ is open in the lower topology. The symmetric topology is the usual topology on $\mathbb{R}$ with $+\infty$ as an isolated point.

(b) For the subcone $\overline{\mathbb{R}}_+ = \{a \in \overline{\mathbb{R}} \mid a \geq 0\}$ of $\overline{\mathbb{R}}$ we may also consider the singleton neighborhood system $V = \{0\}$. The elements of $\overline{\mathbb{R}}_+$ are obviously bounded below even with respect to the neighborhood $v = 0$, hence $\overline{\mathbb{R}}_+$ is a full locally convex cone. For $a \in \overline{\mathbb{R}}$ the intervals $(-\infty, a]$ and $[a, +\infty]$ are the only upper and lower neighborhoods, respectively. The symmetric topology is the discrete topology on $\overline{\mathbb{R}}_+$.

(c) Let $(E, V, \leq)$ be a locally convex ordered topological vector space, where V is a basis of closed, convex, balanced and order convex neighborhoods of the origin in E. Recall that equality is an order relation, hence this example will cover locally convex spaces in general. In order to interpret E as a locally convex cone we shall embed it into a larger full cone. This is done in a canonical way: Let P be the cone of all non-empty convex subsets of E, endowed with the usual addition and multiplication of sets by non-negative scalars, that is

$$\alpha A = \{\alpha a \mid a \in A\} \quad \text{and}$$
$$A + B = \{a + b \mid a \in A \text{ and } b \in B\}$$

for $A, B \in P$ and $\alpha \geq 0$. We define the order on P by

$$A \leq B \quad \text{if} \quad A \subset \downarrow B = B + E_-$$

where $E_- = \{x \in E \mid x \leq 0\}$ is the negative cone in E. The requirements for an ordered cone are easily checked. The neighborhood system in P is given by the neighborhood basis $V \subset P$. We observe that for every $A \in P$ and $v \in V$ there is $\rho > 0$ such that $\rho v \cap A \neq \emptyset$. This yields $0 \in A + \rho v$. Therefore $\{0\} \leq A + \rho v$, and every element $A \in P$ is indeed bounded below. Thus (P, V) is a full locally convex cone. Via the embedding $x \to \{x\} : E \to P$ the space E itself is a subcone of P. This embedding preserves the order structure of E, and on its image the symmetric topology of P coincides with the given vector space topology of E. Thus E is indeed a locally convex cone, but not a full cone.

(d) The preceding procedure can be applied to locally convex cones in general. Let (P,V) be a locally convex cone and let $Conv(P)$ denote the cone of all non-empty convex subsets of P, endowed with the canonical order, that is

$$A \leq B \quad \text{if for every} \quad a \in A \quad \text{there is} \quad b \in B$$
$$\text{such that} \quad a \leq b$$

for $A, B \subset P$. The neighborhood $v \in V$ is defined as a neighborhood for $Conv(P)$ by

$$A \leq B + v \quad \text{if for every} \ a \in A \ \text{there is} \ b \in B$$
$$\text{such that} \quad a \leq b + v$$

The requirements for a locally convex cone are easily checked for $(Conv(P), V)$, and (P,V) is identified with a subcone of $(Conv(P), V)$. Other subcones of $Conv(P)$ that merit further investigation are those of all closed, closed and bounded, or compact convex sets in $Conv(P)$, respectively. Details on these and further related examples may be found in [7] and [17].

(e) Let (P,V) be a locally convex cone, X a set and let $F(X,P)$ be the cone of all P-valued functions on X, endowed with the pointwise operations and order. If $\bar{P}$ is a full cone containing both P and V then we may identify the elements $v \in V$ with the constant functions $x \to v$ for all $x \in X$, hence V is a subset and a neighborhood system for $F(X, \bar{P})$. A function $f \in F(X, \bar{P})$ is uniformly bounded below, if for every $v \in V$ there is $\rho \geq 0$ such that $0 \leq f + \rho v$. These functions form a full locally convex cone $(F_b(X, \bar{P}), V)$, carrying the topology of uniform convergence. As a subcone, $(F_b(X, \bar{P}), V)$ is a locally convex cone. Alternatively, a more general neighborhood system V_Y for $F(X,P)$ may be created using a suitable family Y of subsets y of X, directed downward with respect to set inclusion, and the neighborhoods v_y for $v \in V$ and $y \in Y$, defined for functions $f, g \in F(X,P)$ as

$$f \leq g + v_y \quad \text{if} \quad f(x) \leq g(x) + v$$
$$\text{for all} \ x \in y.$$

In this case we consider the subcone $F_{by}(X,P)$ of all functions in $F(X,P)$ that are uniformly bounded below on the sets in Y. Together with the neighborhood system V_Y, it forms a locally convex cone. $(F_{by}(X,P), V_Y)$ carries the topology of uniform convergence on the sets in Y.

(f) For $x \in \mathbb{R}$ denote $x^+ = \max\{x, 0\}$ and $x^- = \min\{x, 0\}$. For $1 \leq p \leq +\infty$ and a sequence $(x_i)_{i \in \mathbb{N}}$ in $\mathbb{R}$ let $\|x_i\|_p$ denote the usual l^p norm, that is

$$\|(x_i)\|_p = \left(\sum_{i=1}^{\infty} |x_i|^p\right)^{(1/p)} \in \bar{\mathbb{R}}$$

for $p < +\infty$, and

$$\|(x_i)\|_\infty = \sup\{|x_i|| \ i \in \mathbb{N}\} \in \bar{\mathbb{R}}.$$

Now let C^p be the cone of all sequences $(x_i)_{i \in \mathbb{N}}$ in $\bar{\mathbb{R}}$ such that $\|(x_i)\|_p < +\infty$. We use the pointwise order in C^p and the neighborhood system $V_p = \{\rho v_p | \rho > 0\}$, where

$$(x_i)_{i \in \mathbb{N}} \leq (y_i)_{i \in \mathbb{N}} + \rho v_p$$

means that $\|(x_i - y_i)^+\|_p \leq \rho$. (In this expression the l^p norm is evaluated only over the indices $i \in \mathbb{N}$ for which $y_i < +\infty$.) It can be easily verified that (C^p, V_p) is a locally convex cone. In fact (C^p, V_p) can be embedded into a full cone following a procedure analogous to that in 2.1 (c). The case for $p = +\infty$ is of course already covered by Part (d).

4. Continuous linear functionals and Hahn-Banach type theorems
A linear functional μ on a locally convex cone (P,V) is said to be *(uniformly) continuous with respect to a neighborhood $v \in V$* if

$$\mu(a) \leq \mu(b) + 1 \quad \text{whenever} \quad a \leq b + v.$$

Continuity implies that the functional μ is monotone, even with respect to the global preorder $\lesssim$, and takes only finite values in bounded elements $b \in \mathcal{B}$ (see Section 5 below).

The set of all linear functionals μ on P which are continuous with respect to a certain neighborhood v is called the *polar* of v in P and denoted by v_P° (or v° for short). Endowed with the canonical addition and multiplication by non-negative scalars, the union of all polars v° for $v \in V$ forms the *dual cone P^** of P.

We may now formulate a topological version of the sandwich theorem (Theorem 3.1 in [13]) for linear functionals: Generalizing our previous notion we define an *extended superlinear functional* on P as a mapping

$$q: P \to \underline{\overline{\mathbb{R}}} = \mathbb{R} \cup \{+\infty, -\infty\}$$

such that $q(\alpha a) = \alpha q(a)$ holds for all $a \in P$ and $\alpha \geq 0$ and

$$q(a + b) \geq q(a) + q(b) \quad \text{whenever}$$
$$q(a), q(b) > -\infty$$

(We set $\alpha + (-\infty) = -\infty$ for all $\alpha \in \mathbb{R} \cup \{-\infty\}$, $\alpha \cdot (-\infty) = -\infty$ for all $\alpha > 0$ and $0 \cdot (-\infty) = 0$ in this context.)

4.1 Sandwich Theorem (topological). *Let (P, V) be a locally convex cone, and let $v \in V$. For a sublinear functional $p : P \to \overline{\mathbb{R}}$ and an extended superlinear functional $q : P \to \underline{\overline{\mathbb{R}}}$ there exists a linear functional $\mu \in v^\circ$ such that $q \leq \mu \leq p$ if and only if*

$$q(a) \leq p(b) + 1 \quad \text{holds whenever} \quad a \leq b + v$$

Recall that every monotone linear functional μ on an ordered cone P gives rise to a uniform neighborhood $v = \{(a, b) \in P^2 \mid \mu(a) \leq \mu(b) + 1\}$ which in turn may be used to define a locally convex structure on P. Thus, the condition for p and q in Theorem 4.1 for some neighborhood v is necessary and sufficient for the existence of a monotone linear functional μ on P such that $q \leq \mu \leq p$.

Citing from [13] we mention a few corollaries. A set $C \subset P$ is called *increasing* resp. *decreasing*, if $a \in C$ whenever $c \leq a$ resp. $a \leq c$ for $a \in P$ and

some $c \in C$. A convex set $C \subset P$ such that $0 \in C$ is called *left-absorbing* if for every $a \in P$ there are $c \in C$ and $\lambda \geq 0$ such that $\lambda c \leq a$.

4.2 Corollary. *Let P be an ordered cone. For a sublinear functional $p : P \to \overline{\mathbb{R}}$ there exists a monotone linear functional $\mu : P \to \overline{\mathbb{R}}$ such that $\mu \leq p$ if and only if p is bounded below on some increasing left-absorbing convex set $C \subset P$.*

An $\overline{\mathbb{R}}$-valued function f defined on a convex subset C of a cone P is called *convex* if

$$f(\lambda c_1 + (1 - \lambda)c_2) \leq \lambda f(c_1) + (1 - \lambda)f(c_2)$$

holds for all $c_1, c_2 \in C$ and $\lambda \in [0,1]$. Likewise, an $\underline{\overline{\mathbb{R}}}$-valued function g on C is *concave* if

$$g(\lambda c_1 + (1 - \lambda)c_2) \geq \lambda g(c_1) + (1 - \lambda)g(c_2)$$

holds for all $c_1, c_2 \in C$ such that $g(c_1), g(c_2) > -\infty$ and $\lambda \in [0,1]$. An *affine* function $h : C \to \overline{\mathbb{R}}$ is both convex and concave. A variety of extension results for linear functionals may be derived from Theorem 4.1 in [13]. We cite:

4.3 Extension Theorem. *Let (P, V) be a locally convex cone, C and D non-empty convex subsets of P, and let $v \in V$. Let $p : P \to \overline{\mathbb{R}}$ be a sublinear and $q : P \to \underline{\overline{\mathbb{R}}}$ an extended superlinear functional. For a convex function $f : C \to \overline{\mathbb{R}}$ and a concave function $g : D \to \underline{\overline{\mathbb{R}}}$ there exists a monotone linear functional $\mu \in v^\circ$ such that*

$$q \leq \mu \leq p, \quad g \leq \mu \text{ on } D \quad \text{and} \quad \mu \leq f \text{ on } C$$

if and only if

$$q(a) + \rho g(d) \leq p(b) + \sigma f(c) + 1 \quad \text{holds}$$
$$\text{whenever} \quad a + \rho d \leq b + \sigma c + v$$

for $a, b \in P$, $c \in C$, $d \in D$ and $\rho, \sigma > 0$ such that $q(a), \rho g(d) > -\infty$.

The generality of this result allows a wide range of special cases. If $g \equiv -\infty$, for example, we have to consider the condition of Theorem 4.3 only for $\rho = 0$, if $f \equiv +\infty$ only for $\sigma = 0$, and if both $g \equiv$

$-\infty$ and $f \equiv +\infty$, then Theorem 4.3 reduces to the previous Sandwich Theorem 4.1. Another case of particular interest occurs when $C = D$ and $f = g$ is an affine function, resp. a linear functional if C is a subcone of P. The latter, with the choice of $p(a) = +\infty$ and $q(a) = -\infty$ for all $0 \neq a \in P$ yields the Extension Theorem II.2.9 from [7]:

4.4 Corollary. *Let (C, V) be a subcone of the locally convex cone (P, V). Every continuous linear functional on C can be extended to a continuous linear functional on P; more precisely: For every $\mu \in v_C^\circ$ there is $\tilde{\mu} \in v_P^\circ$ such that $\tilde{\mu}$ coincides with μ on C.*

The range of all continuous linear functionals that are sandwiched between a given sublinear and an extended superlinear functional is described in Theorem 5.1 in [13].

4.5 Range Theorem. *Let (P, V) be a locally convex cone. Let p and q be sublinear and extended superlinear functionals on P and suppose that there is at least one linear functional $\mu \in P^*$ satisfying $q \leq \mu \leq p$. Then for all $a \in P$ we have*

$$\sup_{\mu \in P^*, q \leq \mu \leq p} \mu(a)$$
$$= \sup_{v \in V} \inf\{p(b) - q(c) \mid b, c \in P, q(c) \in \mathbb{R}, a + c \leq b + v\}$$

For all $a \in P$ such that $\mu(a)$ is finite for at least one $\mu \in P^*$ satisfying $q \leq \mu \leq p$ we have

$$\inf_{\mu \in P^*, q \leq \mu \leq p} \mu(a)$$
$$= \inf_{v \in V} \sup\{q(c) - p(b) \mid b, c \in P, p(b) \in \mathbb{R}, c \leq a + b + v\}$$

As another consequence of the Extension Theorem 4.3 we obtain the following result (Theorem 4.5 in [13]) about the separation of convex subsets by monotone linear functionals:

4.6 Separation Theorem. *Let C and D be non-empty convex subsets of a locally convex cone (P, V). Let $v \in V$ and $\alpha \in \mathbb{R}$. There exists a monotone linear functional $\mu \in v^\circ$ such that*

$$\mu(c) \leq \alpha \leq \mu(d) \quad \text{for all } c \in C \text{ and } d \in D$$

if and only if

$$\alpha \rho \leq \alpha \sigma + 1 \quad \text{whenever} \quad \rho d \leq \sigma c + v$$

for all $c \in C$, $d \in D$ and $\rho, \sigma \geq 0$.

5. The weak preorder and the relative topologies

We also consider a (topological and linear) closure of the given order on a locally convex cone, called the weak preorder $\preccurlyeq$ which is defined as follows (see I.3 in [17]): We set

$$a \preccurlyeq b + v \quad \text{for } a, b \in P \text{ and } v \in V$$

if for every $\varepsilon > 0$ there is $1 \leq \gamma \leq 1 + \varepsilon$ such that $a \leq \gamma b + (1 + \varepsilon)v$, and set
$$a \preccurlyeq b$$

if $a \preccurlyeq b + v$ for all $v \in V$. This order is clearly weaker than the given order, that is $a \leq b$ or $a \leq b + v$ implies $a \preccurlyeq b$ or $a \preccurlyeq b + v$. Importantly, the weak preorder on a locally convex cone is entirely determined by its dual cone P^*, that is $a \preccurlyeq b$ holds if and only if $\mu(a) \leq \mu(b)$ for all $\mu \in P^*$, and $a \preccurlyeq b + v$ if and only $\mu(a) \leq \mu(b) + 1$ for all $\mu \in v^\circ$ (Corollaries I.4.31 and I.4.34 in [17]). If endowed with the weak preorder (P, V) is again a locally convex cone with the same dual P^*.

While all elements of a locally convex cone are bounded below, they need not be bounded above. An element $a \in P$ is called *bounded (above)* (see [7], I.2.3) if for every $v \in V$ there is $\lambda > 0$ such that $a \leq \lambda v$. By $\mathcal{B}$ we denote the subcone of P containing all bounded elements. $\mathcal{B}$ is indeed a *face* of P, as $a + b \in \mathcal{B}$ for $a, b \in P$ implies that both $a, b \in \mathcal{B}$. Clearly all invertible elements of P are bounded, and bounded elements satisfy a modified version of the cancellation law (see [17], I.4.5), that is

$$(C') \quad a + c \preccurlyeq b + c \text{ for } a, b \in P \text{ and } c \in \mathcal{B}$$
$$\text{implies} \quad a \preccurlyeq b$$

We quote Theorem I.3.3 from [17]:

5.1 Representation Theorem. *A locally convex cone (P,V) endowed with its weak preorder can be represented as a locally convex cone of $\overline{\mathbb{R}}$-valued functions on some set X, or equivalently as a locally convex cone of convex subsets of some locally convex ordered topological vector space.*

The previously introduced upper, lower and symmetric locally convex cone topologies for a locally convex cone (P,V) prove to be too restrictive for the concept of continuity of P-valued functions, since for unbounded elements even the scalar multiplication turns out to be discontinuous (see I.4 in [17]). This is remedied by using the coarser (but somewhat cumbersome) *relative* topologies on P instead. These topologies are defined using the weak preorder on P:

The *upper, lower and symmetric relative topologies* on a locally convex cone (P,V) are generated by the neighborhoods $v_\varepsilon(a)$, $(a)v_\varepsilon$ and $v_\varepsilon^s(a) = v_\varepsilon(a) \cap (a)v_\varepsilon$, respectively, for $a \in P$, $v \in V$ and $\varepsilon > 0$, where

$$v_\varepsilon(a) = \{b \in P|\ b \le \gamma a + \varepsilon v \text{ for some} \\ 1 \le \gamma \le 1 + \varepsilon\}$$
$$(a)v_\varepsilon = \{b \in P|\ a \le \gamma b + \varepsilon v \text{ for some} \\ 1 \le \gamma \le 1 + \varepsilon\}$$

The relative topologies are locally convex but not necessarily locally convex cone topologies in the sense of Section 3 (for details see I.4 in [17]), since the resulting uniformity need not be convex. These topologies are generally coarser, but locally coincide on bounded elements with the given upper, lower and symmetric topologies on P and render the scalar multiplication (with scalars other than zero) continuous. The symmetric relative topology is known to be Hausdorff if and only if the weak preorder on P is antisymmetric (Proposition I.4.8 in [17]). If P is a locally convex topological vector space, then all of the above topologies coincide with the given topology.

6. Boundedness and connectedness components
The details for this section can be found in [16]. Two elements a and b of a locally convex cone

(P,V) are *bounded relative to each other* if for every $v \in V$ there are $\alpha, \beta, \lambda, \rho \ge 0$ such that both

$$a \le \beta b + \lambda v \quad \text{and} \quad b \le \alpha a + \rho v$$

This notion defines an equivalence relation on P and its equivalence classes $\mathcal{B}_s(a)$ are called the *(symmetric) boundedness components* of P. Propositions 5.3, 5.4, 5.6 and 6.1 in [16] state:

6.1 Proposition. *The boundedness components of a locally convex cone (P,V) are closed for addition and multiplication by strictly positive scalars. They satisfy a version of the cancellation law, that is*
$$a + c \leqslant b + c$$

for elements a, b and c of the same boundedness component implies that

$$a \leqslant b.$$

6.2 Proposition. *The boundedness components of a locally convex cone (P,V) furnish a partition of P into disjoint convex subsets that are closed and connected in the symmetric relative topology. They coincide with the connectedness components of P.*

If the neighborhood system V consists of the positive multiples of a single neighborhood, P is locally connected and its connectedness components are also open.

7. Continuous linear operators
For cones P and Q a mapping $T: P \to Q$ is called a *linear operator* if

$$T(a + b) = T(a) + T(b) \quad \text{and} \\ T(\alpha a) = \alpha T(a)$$

hold for all $a, b \in P$ and $\alpha \ge 0$. If both P and Q are ordered, then T is called *monotone* if

$$a \le b \quad \text{implies} \quad T(a) \le T(b).$$

If both (P, V) and (Q, W) are locally convex cones, then T is said to be *(uniformly) continuous* if for every $w \in W$ one can find $v \in V$ such that

$$T(a) \leq T(b) + w \quad \text{whenever} \quad a \leq b + v$$

for $a, b \in P$. A set $\hat{T}$ of linear operators is called *equicontinuous* if the above condition holds for every $w \in W$ with the same $v \in V$ for all $T \in \hat{T}$. Uniform continuity for an operator implies monotonicity with respect to the global preorders on P and on Q that is: if

$$a \leq b + v \text{ for all } v \in V, \quad \text{then}$$
$$T(a) \leq T(b) + w \text{ for all } w \in W$$

In this context, a linear functional is a linear operator $\mu : P \to \overline{\mathbb{R}}$, and the above notion of continuity conforms to the preceding one (see Section 4). Moreover, for two continuous linear operators S and T from P into Q and for $\lambda \geq 0$, the sum $S + T$ and the multiple λT are again linear and continuous. Thus the continuous linear operators from P into Q again form a cone. The *adjoint operator T^** of $T : P \to Q$ is defined by

$$\left(T^*(\nu)\right)(a) = \nu(T(a))$$

for all $\nu \in Q^*$ and $a \in P$. Clearly $T^*(\nu) \in P^*$, and T^* is a linear operator from Q^* to P^*; more precisely: If for $v \in V$ and $w \in W$ we have $T(a) \leq T(b) + w$ whenever $a \leq b + v$, then T^* maps w° into v°.

While some concepts from duality and operator theory of locally convex vector spaces may be readily transferred to the more general context of locally convex cones, others require a new approach and offer insights into a far more elaborate structure. The concept of completeness, for example, does not lend itself to a straightforward transcription. It is adapted to locally convex cones in [12] in order to allow a reformulation of the uniform boundedness principle for Fréchet spaces. The approach uses the notions of *internally bounded* subsets, *weakly cone complete* and *barreled* cones. These definitions turn out to be rather technical and we refrain from supplying the details. We cite the main result, which generalizes the classical uniform boundedness theorem:

7.1 Uniform Boundedness Theorem. *Let (P, V) and (Q, W) be locally convex cones, and let $\hat{T}$ be a family of u-continuous linear operators from P to Q. Suppose that for every $b \in P$ and $w \in W$ there is $v \in V$ such that for every $a \in v(b) \cap (b)v$ there is $\lambda > 0$ such that*

$$T(a) \leq T(b) + \lambda w \quad \text{for all } T \in \hat{T}$$

If (P, V) is barreled and (Q, W) has the strict separation property [that is, (Q, W) satisfies Theorem 4.6)], then for every internally bounded set $\mathcal{B} \subset P$, every $b \in \mathcal{B}$ and $w \in W$ there is $v \in V$ and $\lambda > 0$ such that

$$T(a) \leq T(b) + \lambda w \quad \text{for all } T \in \hat{T}$$

and all $a \in v(b') \cap (b'')v$ for some $b', b'' \in \mathcal{B}$.

8. Duality of cones and inner products

We excerpt and augment the following from Ch.II.3 in [7]: A *dual pair (P, Q)* consists of two ordered cones P and Q together with a bilinear map, i.e. a mapping

$$(a, b) \to \langle a, b \rangle : P \times Q \to \overline{\mathbb{R}}$$

which is linear in both variables and compatible with the order structures on both cones, satisfying

$$\langle a, y \rangle + \langle b, x \rangle \leq \langle a, x \rangle + \langle b, y \rangle \quad \text{whenever}$$
$$a \leq b \text{ and } x \leq y.$$

Let us denote by

$$P^+ = \{a \in P \mid 0 \leq a\} \quad \text{and}$$
$$Q^+ = \{a \in Q \mid 0 \leq a\}$$

the respective subcones of positive elements in P and Q. The above condition guarantees that all elements $x \in Q^+$, via $a \to \langle a, x \rangle$ define monotone linear functionals on P, and vice versa.

If we endow the dual cone P^* of a locally convex cone (P, V) with the canonical order

$$\mu \leq \nu \quad \text{if} \quad \nu = \mu + \sigma \text{ for some } \sigma \in P^*,$$

then all elements $\mu \in P^*$ are positive. With the evaluation as its canonical bilinear form, (P, P^*) forms a dual pair.

Dual pairs give rise to *polar topologies* in the following way: A subset X of Q^+ is said to be σ-*bounded below* if

$$\inf\{\langle a, x\rangle \mid x \in X\} > -\infty$$

for all $a \in P$. Every such subset $X \subset Q^+$ defines a uniform neighborhood $v_X \in P^2$ by

$$v_X = \{(a, b) \in P^2 \mid \langle a, x\rangle \leq \langle b, x\rangle + 1 \text{ for all } x \in X\}$$

and any collection χ of σ-bounded below subsets of Q satisfying:

(P1) $\lambda X \in \chi$ whenever $X \in \chi$ and $\lambda > 0$.
(P2) For all $X, Y \in \chi$ there is some $Z \in \chi$ such that $X \cup Y \subset Z$.

defines a convex quasiuniform structure on P. If we denote the corresponding neighborhood system by $V_\chi = \{v_X \mid X \in \chi\}$, then (P, V_χ) becomes a locally convex cone. The polar v_X° of the neighborhood $v_X \in V_\chi$ consists of all linear functionals μ on P such that for $a, b \in P$

$$\langle a, x\rangle \leq \langle b, x\rangle + 1 \quad \text{for all } x \in X \quad \text{implies that}$$
$$\mu(a) \leq \mu(b) + 1.$$

All elements of $X \subset Q$, considered as linear functionals on P, are therefore contained in v_X°.

8.1 Examples. (a) Let χ be the family of all finite subsets of Q^+. The resulting polar topology on P is called the *weak*-topology* $\sigma(P, Q)$.

(b) Let (P, V) be a locally convex cone with the strict separation property (SP). Consider the dual pair (P, P^*) and the collection χ of the polars

$v^\circ \subset P^*$ of all neighborhoods $v \in V$. The resulting polar topology on P coincides with the original one. This shows in particular that every locally convex cone topology satisfying (SP) may be considered as a polar topology.

Two specific topologies on Q, denoted $w(Q, P)$ and $s(Q, P)$, are of particular interest: Both are topologies of pointwise convergence for the elements of P considered as functions on Q with values in $\bar{\mathbb{R}}$. For $w(Q, P)$, $\bar{\mathbb{R}}$ is considered with its usual (one-point compactification) topology, whereas $+\infty$ is treated as an isolated point for $s(Q, P)$. A typical neighborhood for $x \in Q$, defined via a finite subset $A = \{a_1, \ldots, a_n\}$ of P, is given in the topology $w(Q, P)$ by

$$W_A(x) = \left\{y \in Q \,\middle|\, \begin{array}{ll} |\langle a_i, y\rangle - \langle a_i, x\rangle| \leq 1, & \text{if } \langle a_i, x\rangle < +\infty \\ \langle a_i, y\rangle > 1, & \text{if } \langle a_i, x\rangle = +\infty \end{array}\right\}$$

and in the topology $s(Q, P)$ by

$$S_A(x) = \left\{y \in Q \,\middle|\, \begin{array}{ll} |\langle a_i, y\rangle - \langle a_i, x\rangle| \leq 1, & \text{if } \langle a_i, x\rangle < +\infty \\ \langle a_i, y\rangle = +\infty, & \text{if } \langle a_i, x\rangle = +\infty \end{array}\right\}$$

In general, $s(Q, P)$ is therefore finer than $w(Q, P)$, but both topologies coincide if the bilinear form on $P \times Q$ attains only finite values.

In analogy to the Alaoglu-Bourbaki theorem in locally convex vector spaces (see [18], III.4), we obtain (Proposition 2.4 in [7]):

8.2 Theorem. *Let (P, V) be a locally convex cone. The polar v° of any neighborhood $v \in V$ is a compact convex subset of P^* with respect to the topology $w(P^*, P)$.*

Likewise, a Mackey-Arens type result is available for locally convex cones (Theorem 3.8 in [7]):

8.3 Theorem. *Let (P, Q) be a dual pair of ordered cones, and let $X \subset Q$ be the union of finitely many $s(Q, P)$-compact convex subsets of Q^+. Then for every linear functional $\mu \in v_X^\circ$ on P there is an element $x \in Q$ such that*

$$\mu(a) = \langle a, x \rangle \quad \textit{for all} \ \ a \in P \quad \textit{with}$$
$$\mu(a) < +\infty.$$

The last theorem applies is particular to the weak*-topology $\sigma(P, Q)$ which is generated by the finite subsets of Q.

An *inner product* on an ordered cone P may be defined as a bilinear form on $P \times P$ which is commutative and satisfies

$$2\langle a, b \rangle \leq \langle a, a \rangle + \langle b, b \rangle \quad \text{for all} \ \ a, b \in P$$

Investigations on inner products yield Cauchy-Schwarz and Bessel-type inequalities, concepts for orthogonality and best approximation, as well as an analogy for the Riesz representation theorem for continuous linear functionals. For details we refer to [14].

9. Extended algebraic operations

Example 2.1 (b) suggests that the scalar multiplication in a cone might be canonically extended for all scalars in $\mathbb{R}$ or $\mathbb{C}$, but only a weakened version of the distributive law holds for non-positive scalars. For details of the following we refer to [11]. Let $\mathbb{K}$ denote either the field of the real or the complex numbers, and

$$\Delta = \{\delta \in \mathbb{K} | \ |\delta| \leq 1\},$$
$$\text{resp.} \quad \Gamma = \{\gamma \in \mathbb{K} | \ |\gamma| = 1\}$$

the closed unit disc, resp. unit sphere in $\mathbb{K}$.

An ordered cone P is *linear over* $\mathbb{K}$ if the scalar multiplication is extended to all scalars in $\mathbb{K}$ and in addition to the requirements for an ordered cone satisfies

$$
\begin{array}{ll}
\alpha(\beta a) = (\alpha\beta)a & \text{for all } a \in P \text{ and} \\
& \alpha, \beta \in \mathbb{K} \\
\alpha(a + b) = \alpha a + \alpha b & \text{for all } a, b \in P \text{ and} \\
& \alpha \in \mathbb{K} \\
(\alpha + \beta)a = \alpha a + \beta a & \text{for all } a \in P \text{ and} \\
& \alpha, \beta \in \mathbb{K}
\end{array}
$$

It is necessary in this context to distinguish carefully between the additive inverse $-a$ of an element $a \in P$ which may exist in P, and the element $(-1)a \in P$. Both need not coincide.

We define the *modular order* $\preccurlyeq_m$ for elements $a, b \in P$ by

$$a \preccurlyeq_m b \quad \text{if} \quad \gamma a \leq \gamma b \ \text{ for all } \ \gamma \in \Gamma$$

The basic properties of an order relation are easily checked. Likewise the relation $\preccurlyeq_m$ is seen to be compatible with the extended algebraic operations in P, i.e.

$$
\begin{array}{l}
a \preccurlyeq_m b \quad \text{implies} \quad \lambda a \preccurlyeq_m \lambda b \\
\quad \text{and} \quad a + c \preccurlyeq_m b + c
\end{array}
$$

for all $\lambda \in \mathbb{K}$ and $c \in P$. Obviously

$$a \preccurlyeq_m b \quad \text{implies that} \quad a \leq b.$$

Indeed, our version of the distributive law entails that

$$(\alpha + \beta)a \preccurlyeq_m \alpha a + \beta a$$
$$\text{holds for all} \ \ a \in P \ \text{ and } \ \alpha, \beta \in \mathbb{K}.$$

Using the modular order we define an equivalence relation $\sim_m$ on P by

$$a \sim_m b \quad \text{if} \quad a \preccurlyeq_m b \ \text{ and } \ b \preccurlyeq_m a$$

An element $a \in P$ is called $\tilde{m}$-*invertible* if there is $b \in P$ such that $a + b \sim_m 0$. Any two $\tilde{m}$-inverses of the same element a are equivalent in the above sense. We summarize a few observations (Lemma 2.1 in [11]):

9.1 Lemma. *Let P be an ordered cone that is linear over $\mathbb{K}$. Then*

(a)　$\alpha 0 = 0$ *for all $\alpha \in \mathbb{K}$.*
(b)　$0 \preccurlyeq_m a + (-1)a$ *for all $a \in P$.*
(c)　*If $a \in P$ is $\tilde{m}$-invertible, then*
　　$(\alpha + \beta)a \sim_m \alpha a + \beta a$ *holds for all $\alpha, \beta \in \mathbb{K}$, and $(-1)a \sim_m b$ for all $\tilde{m}$-inverses b of a.*
(d)　*If both $a, b \in P$ are $\tilde{m}$-invertible, then $a \preccurlyeq_m b$ implies $a \sim_m b$.*

If (P, V) is a locally convex cone and P is linear over $\mathbb{K}$, then the neighborhoods $v \in V$ and the modular order on P give rise to corresponding *modular neighborhoods* $v_m \in V_m$ in the following way: For $a, b \in P$ and $v \in V$ we define

$$a \leqslant_m b + v_m$$

if $\gamma a \leqslant_m \gamma b + v$ for all $\gamma \in \Gamma$. Clearly $a \leqslant_m b + v_m$ implies that $\lambda a \leqslant_m \lambda b + |\lambda| v_m$ for all $\lambda \in \mathbb{K}$. We denote the system of modular neighborhoods on P by V_m. If we require that every element $a \in P$ is also bounded below with respect to these modular neighborhoods, i.e. if for every $v \in V$ there is $\lambda > 0$ such that

$$0 \leq \gamma a + \lambda v \quad \text{for all } \gamma \in \Gamma,$$

then (P, V_m) with the modular order is again a locally convex cone. In this case we shall say that (P, V) is a *locally convex cone over* $\mathbb{K}$. The respective (upper, lower and symmetric) modular topologies on P are finer than those resulting from the original neighborhoods in V.

9.2 Examples. (a) Let $P = \bar{\mathbb{K}} = \mathbb{K} \cup \{\infty\}$ be endowed with the usual algebraic operations, in particular $a + \infty = \infty$ for all $a \in \bar{\mathbb{K}}$, $\alpha \cdot \infty = \infty$ for all $0 \neq \alpha \in \mathbb{K}$ and $0 \cdot \infty = 0$. The order on $\bar{\mathbb{K}}$ is defined by

$$a \leq b \quad \text{if } b = \infty \text{ or } \Re(a) \leq \Re(b).$$

With the neighborhood system $V = \{\varepsilon > 0\}$, $\bar{\mathbb{K}}$ is a full locally convex cone. It is easily checked that $\bar{\mathbb{K}}$ is linear over $\mathbb{K}$. The modular order on $\bar{\mathbb{K}}$ is identified as $a \leqslant_m b$ if either $b = \infty$ or $a = b$. For $v = \varepsilon \in V$ we have $a \leqslant_m b + v_m$ if either $b = \infty$ or $|a - b| \leq \varepsilon$.

(b) We augment our Example 3.1 (c) as follows: Let $(E, \leq)$ be a locally convex ordered topological vector space over $\mathbb{K}$. For $A \in P = Conv(E)$ we define the multiplication by *any* scalar $\alpha \in \mathbb{K}$ by

$$\alpha A = \{\alpha a \mid a \in A\}$$

for $\alpha \in \mathbb{K}$ and $A \in P$, and the addition and order as in 3.1 (c), that is

$$A \leq B \quad \text{if} \quad A \subset \, \downarrow B$$

Thus P is linear over $\mathbb{K}$. Considering the modular order on P, for $A \in P$ we denote by

$$\downarrow_m A = \bigcap_{\gamma \in \Gamma} (\bar{\gamma} \downarrow (\gamma A))$$

(for $\mathbb{K} = \mathbb{R}$ this is just the order interval generated by A). Thus

$$A \leqslant_m B \quad \text{if} \quad A \subset \, \downarrow_m B$$

As in 3.1 (c), the abstract neighborhood system in P is given by a basis $V \subset P$ of closed absolutely convex neighborhoods of the origin in E. Every element $A \in P$ is seen to be m-bounded below, thus fulfilling the last requirement for a locally convex cone over $\mathbb{K}$.

The case $E = \mathbb{K}$ with the order from 9.2 (a), i.e. $a \leq b$ if $\Re(a) \leq \Re(b)$, is of particular interest for the investigation of linear functionals: For $A, B \in Conv(\mathbb{K})$ we have $A \leq B$ if $\sup\{\Re(a) \mid a \in A\} \leq \sup\{\Re(b) \mid b \in B\}$ and $A \leqslant_m B$ if $A \subset B$. For $\varepsilon > 0$ the neighborhood $\varepsilon \Delta \in V$ is determined by

$$A \leq B \oplus \varepsilon \Delta$$
$$\text{if } \sup\{\Re(a) \mid a \in A\} \leq \sup\{\Re(b) \mid b \in B\} + \varepsilon,$$

and

$$A \leqslant_m B \oplus \varepsilon \Delta_m \quad \text{if} \quad A \subset B \oplus \varepsilon \Delta$$

(c) Let P consist of all $\bar{\mathbb{R}}$-valued functions f on $[-1, +1]$ that are uniformly bounded below and satisfy $0 \leq f(x) + f(-x)$ for all $x \in [-1, +1]$. Endowed with the pointwise addition and multiplication by non-negative scalars, the order $f \leq g$ if $f(x) \leq g(x)$ for all $0 \leq x \leq 1$, and the neighborhood system V consisting of the (strictly) positive constants, P is a full locally convex cone. We may extend the scalar multiplication to negative reals α and $f \in P$ by

$$(\alpha f)(x) = (-\alpha) f(-x)$$

for all $x \in [-1, +1]$. Thus P is seen to be linear over $\mathbb{R}$. The modular order on P is the pointwise order on the whole interval $[-1, +1]$.

For a locally convex cone over $\mathbb{K}$ we shall denote by $\mathcal{B}_m$ the subcone of all *m-bounded* elements, i.e. those elements $a \in P$ such that for every $v \in V$ there is $\lambda > 0$ such that $a \preccurlyeq_m \lambda v_m$. Clearly $\mathcal{B}_m \subset \mathcal{B}$. We cite Theorem 2.3 from [11]:

9.3 Theorem. *Every locally convex cone (P, V) can be embedded into a locally convex cone $(\tilde{P}, V)$ over $\mathbb{K}$. The embedding is linear, one-to-one and preserves the global preorder and the neighborhoods of P. All bounded elements $a \in P$ are mapped onto m-bounded elements of $\tilde{P}$ and are $\tilde{m}$-invertible in $\tilde{P}$.*

Let (P, V) be a locally convex cone over $\mathbb{K}$. Endowed with the corresponding modular neighborhood system, (P, V_m) is again a locally convex cone. We denote the dual cone of (P, V_m) by P_m^* and refer to it as the *modular dual* of P. As continuity with respect to the given topology implies continuity with respect to the modular topology we have $P^* \subset P_m^*$. By v_m° we denote the (modular) polar of the neighborhood $v_m \in V_m$, i.e. the set of all linear functionals $\mu \in P_m^*$ such that

$$\mu(a) \leq \mu(b) + 1 \text{ holds whenever } a \preccurlyeq_m b + v_m$$

Monotone linear functionals in $\mu : P \to \overline{\mathbb{R}}$ are required to be homogeneous only with respect to the multiplication by positive reals. For negative reals $\alpha < 0$ the relation $\alpha a + (-\alpha)a \geq 0$ yields $\mu(\alpha a) \geq \alpha \mu(a)$. But for complex numbers α in general we fail to recognize any obvious relation between $\mu(\alpha a)$ and $\alpha \mu(a)$. This may be remedied, at least for a large class of functionals in P_m^*, by the following procedure: An element $a \in P$ is called *m-continuous* if the mapping

$$\gamma \to \gamma a : \Gamma \to P$$

is uniformly continuous with respect to the upper topology on P, i.e. if for every $v \in V$ there is $\varepsilon > 0$ such that $\gamma a \leq \gamma' a + v$ holds for all $\gamma, \gamma' \in \Gamma$ satisfying $|\gamma - \gamma'| \leq \varepsilon$. For $\mathbb{K} = \mathbb{R}$ this condition

is obviously void. For $\mathbb{K} = \mathbb{C}$, however, the *m*-continuous elements form a subcone of P which we shall denote by C_m. Obviously $\mathcal{B}_m \subset C_m$. A functional $\mu \in P_m^*$ is called *regular* if

$$\mu(a) = \sup\{\mu(c) | \ c \in C_m, c \preccurlyeq_m a\}$$

holds for all $a \in P$. For $\mathbb{K} = \mathbb{R}$, of course, as all elements $a \in P$ are *m*-continuous, every $\mu \in P_m^*$ is regular. For a regular linear functional $\mu \in P_m^*$ and every $a \in P$ we may define a corresponding set-valued function $\mu_c : P \to Conv(\mathbb{K})$ by

$$\mu_c(a) = \{a \in \mathbb{K} | \ \Re(\gamma \alpha) \leq \mu(\gamma \alpha)$$
$$\text{for all } \ \gamma \in \mathbb{K}\}$$

The regularity of μ entails (see [11]) that $\mu_c(a)$ is non-empty, closed and convex in $\mathbb{K}$, and that

$$\mu(\gamma \alpha) = \sup\{\Re(\gamma \alpha) | \ \alpha \in \mu_c(a)\}$$

holds for all $\gamma \in \mathbb{K}$. The latter shows in particular that the correspondence between μ and μ_c is one-to-one. For $\mathbb{K} = \mathbb{R}$ the values of μ_c are closed intervals in $\mathbb{R}$; more precisely:

$$\mu_c(a) = [-\mu((-1)a), \mu(a)] \cap \mathbb{R}.$$

The mapping $\mu_c : P \to Conv(\mathbb{K})$ is additive and homogeneous with respect to the multiplication by all scalars in $\mathbb{K}$. More precisely:

9.4 Lemma. *Let $\mu : P \to \overline{\mathbb{R}}$ be a regular monotone linear functional. For $\mu_c : P \to Conv(\mathbb{K})$ the following hold:*

(a) *$\mu_c(a)$ is a non-empty closed convex subset of $\mathbb{K}$.*
(b) *$\mu_c(a + b) = \mu_c(a) \oplus \mu_c(b)$ for all $a, b \in P$.*
(c) *$\mu_c(\alpha a) = \alpha \mu_c(a)$ for all $a \in P$ and $\alpha \in \mathbb{K}$.*
(d) *If $a \in P$ is $\tilde{m}$-invertible then $\mu_c(a)$ is a singleton subset of $\mathbb{K}$.*
(e) *μ_c is continuous with respect to the modular topologies on P and $Conv(\mathbb{K})$; more precisely: if $\mu \in v_m^\circ$ then, for $a, b \in P$,*

$$a \preccurlyeq_m b + v_m \quad \text{implies that}$$
$$\mu_c(a) \subset \mu_c(b) \oplus \Delta,$$

where Δ denotes the closed unit disc in $\mathbb{C}$.

9.5 Examples. Reviewing our Example 9.2 (b), i.e. the locally convex cone $P = Conv(E)$ over $\mathbb{K}$, where $(E, \leq)$ denotes a locally convex ordered topological vector space, we realize that for every $\mathbb{K}$-valued continuous linear functional f on E, the mapping $\mu: P \to \bar{\mathbb{R}}$ such that

$$\mu(A) = \sup\{\Re(f(a))| \ a \in A\}$$

is linear, an element of P_m^* and obviously regular. The corresponding set-valued functional $\mu_c : P \to Conv(\mathbb{K})$ is given by

$$\mu_c(A) = f(A) = \{f(a)| \ a \in A\}.$$

However, in the complex case, even for $E = \mathbb{C}$, one can find examples of non-regular linear functionals in P_m^*.

However, in the complex case, even for $E = \mathbb{C}$, one can find examples of non-regular linear functionals in P_m^*.

It is possible to construct a decomposition for regular functionals $\mu \in P_m^*$ into functionals in P^*. In a locally convex ordered topological vector space over $\mathbb{R}$ every continuous linear functional may be expressed as a difference of two positive ones (see [18], IV.3.2). A similar decomposition is available in the complex case. The more general setting of locally convex cones, however, requires the use of Riemann-Stieltjes type integrals instead of sums. In this instance we refrain from supplying the detailed arguments and notations for this rather technical procedure. They may be found in [11]. The main result is:

9.6 Theorem. *Let (P, V) be a locally convex cone over $\mathbb{K}$. For every regular linear functional $\mu \in P_m^*$ there exists a P^*-valued m-integrating family $(\vartheta_E)_{E \in \mathbb{R}}$ on the unit circle Γ in $\mathbb{C}$ such that*

$$\mu = \int_\Gamma \gamma \, d\vartheta$$

In the case of a locally convex cone over $\mathbb{R}$, where $\Gamma = \{-1, +1\}$, this result simplifies considerably. Every linear functional $\mu \in P_m^*$ is regular then, and the integral representation in Theorem 7.6 reduces to a sum of two functionals.

9.7 Corollary. *Let (P, V) be a locally convex cone over $\mathbb{R}$. For every linear functional $\mu \in P_m^*$ there exist $\mu_1, \mu_2 \in P^*$ such that*

$$\mu(a) = \mu_1(a) + \mu_2((-1)a) \ \text{for all } a \in P.$$

10. Application: Korovkin type approximation
Locally convex cones provide a suitable setting for a rather general approach to Korovkin type theorems, an extensively studied field in abstract approximation theory. For a detailed survey on this subject we refer to [2]. Approximation schemes may often be modeled by sequences (or nets) of linear operators. For a sequence $(T_n)_{n \in \mathbb{N}}$ of positive linear operators on $C([0,1])$, Korovkin's theorem (see [8]) states that $T_n(f)$ converges uniformly to f for every $f \in C([0,1])$, whenever $T_n(g)$ converges to g for the three test functions $g = 1, x, x^2$. This result was subsequently generalized for different sets of test functions g and different topological spaces X replacing the interval $[0,1]$. Classical examples include the Bernstein operators and the Fejér sums which provide approximation schemes by polynomials and trigonometric polynomials, respectively. Further generalizations investigate the convergence of certain classes of linear operators on various domains, such as positive operators on topological vector lattices, contractive operators on normed spaces, multiplicative operators on Banach algebras, monotone operators on set-valued functions, monotone operators with certain restricting properties on spaces of stochastic processes, etc. Typically, for a subset M of a domain L one tries to identify all elements $f \in L$ such that

$$T_\alpha(g) \to g \ \text{for all } g \in M \quad \text{implies that}$$
$$T_\alpha(f) \to f,$$

whenever $(T_\alpha)_{\alpha \in A}$ is an equicontinuous net (generalized sequence) in the restricted class of

operators on L. Locally convex cones allow a unified approach to most of the above mentioned cases. Various restrictions on classes of operators may be taken care of by the proper choice of domains and their topologies alone and approximation results may be obtained through the investigation of continuous linear operators between locally convex cones. We proceed to outline a few results that may be found in Chapters III and IV of [7]:

Let Q be a subcone of the locally convex cone (P,V). The element $a \in P$ is said to be Q-superharmonic in $\mu \in P^*$ if $\mu(a)$ is finite and if for all $v \in P^*$,

$$v(b) \le \mu(b) \text{ for all } b \in Q \quad \text{implies that}$$
$$v(a) \le \mu(a)$$

This notation is derived from potential theory. We cite Theorem III.1.3 from [7] which is an immediate corollary to our Range Theorem 4.5 with the following insertions: We choose $q(a) = -\infty$ for all $a \ne 0$ and $p(a) = \mu(a)$ for $a \in Q$, otherwise $p(a) = +\infty$, and obtain:

10.1 Sup-Inf-Theorem. *Let Q be a subcone of the locally convex cone (P,V). Let $a \in P$ and $\mu \in P^*$ such that $\mu(a)$ is finite. Then a is Q-superharmonic in μ if and only if*

$$\mu(a) = \sup_{v \in V} \inf\{\mu(b)| \ b \in Q, a \le b + v\}.$$

We shall cite only a simplified version of the main Convergence Theorem IV.1.13 in [7] for nets of linear operators on a locally convex cone. It is however sufficient to derive the classical results for Korovkin type approximation processes. For a net $(a_\alpha)_{\alpha \in A}$ in P we shall denote $a_\alpha \uparrow b$ if $(a_\alpha)_{\alpha \in A}$ converges towards $b \in P$ with respect to the upper topology, i.e. if for every $v \in V$ there is α_0 such that

$$a_\alpha \le b + v \quad \text{for all } \alpha \ge \alpha_0.$$

10.2 Convergence Theorem. *Let Q be a subcone of the locally convex cone (P,V). Suppose that for every $v \in V$ the element $a \in P$ is Q-*

superharmonic in all functionals of the $w(P^*,P)$-closure of the set of extreme points of v°. Then for every equicontinuous net $(T_\alpha)_{\alpha \in A}$ of linear operators on P

$$T_\alpha(b) \uparrow b \text{ for all } b \in Q \quad \text{implies that}$$
$$T_\alpha(a) \uparrow a.$$

Let us mention just one of the many well-known Korovkin type theorems that may be derived using Theorems 10.1 and 10.2: Let X be a locally compact Hausdorff space, $P = C_0(X)$ the space of all continuous real-valued functions on X that vanish at infinity, and let V consist of all positive constant functions. With the pointwise order and algebraic operations, (P,V) is a locally convex cone. Continuous linear operators on P are monotone and bounded with respect to the norm of uniform convergence on $C_0(X)$. The extreme points of polars of neighborhoods are just the non-negative multiples of point evaluations. Finally, convergence $f_\alpha \to f$ for a net of functions in $C_0(X)$ in the uniform topology means that both $f_\alpha \uparrow f$ and $(-f_\alpha) \uparrow (-f)$. We obtain a result due to Bauer and Donner [4]:

10.3 Theorem. *Let X be a locally compact Hausdorff space, and let M be a subset of $C_0(X)$. For a function $f \in C_0(X)$ the following are equivalent:*

(a) For every equicontinuous net $(T_\alpha)_{\alpha \in A}$ of positive linear operators on $C_0(X)$

$$T_\alpha(g) \to g \text{ for all } g \in M \quad \text{implies that}$$
$$T_\alpha(f) \to f$$

(Convergence is meant with respect to the topology of uniform convergence on X.)

(b) For every $x \in X$

$$f(x) = \sup_{\varepsilon > 0} \inf \left\{ g(x) \middle| \begin{array}{l} g \in \text{span}(M), \\ f \le g + \varepsilon \end{array} \right\}$$
$$= \inf_{\varepsilon > 0} \sup \left\{ g(x) \middle| \begin{array}{l} g \in \text{span}(M), \\ g \le f + \varepsilon \end{array} \right\}$$

(c) For every $x \in X$ and for every bounded positive regular Borel measure μ on X

$$\mu(g) = g(x) \text{ for all } g \in M \quad \text{implies that}$$
$$\mu(f) = f(x)$$

The General Convergence Theorem IV.1.13 in [7] allows a far wider range of applications, including quantitative estimates for the order of convergence for the approximation processes modeled by sequences or nets of linear operators.

11. Application: Topological integration theory

A rather general approach to topological integration theory using locally convex cones is established in [10]. It utilizes techniques originally developed for Choquet theory. Continuous linear functionals on a given locally convex cone P are called *integrals* if they are minimal, resp. maximal with respect to certain subcones of P. Their properties resemble those of Radon measures on locally compact spaces. They satisfy convergence theorems corresponding to Fatou's Lemma and Lebesgue's theorem about bounded convergence. Depending on the choice of the determining subcones of P, one obtains a wide variety of applications, including classical integration theory on locally compact spaces (see [5]), Choquet theory about integral representation (see [1]), H-integrals on H-cones in abstract potential theory and monotone functionals on cones of convex sets. We shall outline some of the main concepts without supplying details and proofs which may be found in [10]:

Let (P, V) be a full locally convex cone, L and U two subcones of P. L is supposed to be a full cone, whereas all elements of U are supposed to be bounded. The following two conditions hold:

(U) *For all $a \in P$, $l \in L$, $u \in U$ such that $u \leq a + l$ and for every $v \in V$ there is $u' \in U$ such that $u' \leq a + v$ and $u \leq u' + l + v$.*

(L) *For all $a \in P$, $l \in L$, $u \in U$ such that $a + u \leq l$ and for every $v \in V$ there is $l' \in L$ such that $a \leq l'$ and $l' + u \leq l + v$.*

For linear functionals $\mu, \nu \in P^*$ we set

$$\mu \preccurlyeq \nu \quad \text{if} \quad \mu(l) \leq \nu(l) \text{ for all } l \in L \quad \text{and}$$
$$\mu(u) \geq \nu(u) \text{ for all } u \in U.$$

We write $\mu \sim \nu$ if both $\mu \preccurlyeq \nu$ and $\nu \preccurlyeq \mu$, i.e. if the functionals μ and ν coincide on U and L. *Integrals on P* are the minimal functionals in this order and (P, L, U) is called an *integration cone*.

11.1 Theorem. *Let (P, L, U) be an integration cone.*

(a) For every continuous linear functional $\mu_0 \in P^*$ there is an integral μ on P such that

$$\mu(l) \leq \mu_0(l) \text{ for all } l \in L \quad \text{and} \quad \mu(u) \geq \mu_0(u) \text{ for all } u \in U.$$

(b) The linear functional $\mu \in P^*$ is an integral if and only if

$$\mu(l) = \inf_{v \in V} \sup\{\mu(u)| \ u \leq l + v, u \in U\}$$
$$\text{for all } l \in L,$$
and

$$\mu(u) = \inf\{\mu(l)| \ u \leq l, l \in L\} \text{ for all } u \in U.$$

An element $a \in P$ is said to be *μ-integrable* with respect to an integral μ if

$$\nu \sim \mu \quad \text{implies that} \quad \nu(a) = \mu(a)$$

for all $\nu \in P^*$. For a given integral μ on P the μ-integrable elements form a subcone of P that contains both L and U.

11.2 Theorem. *Let μ be an integral on P. The element $a \in P$ is μ-integrable if and only if*

$$\inf_{v \in V} \sup\{\mu(u)| \ u \leq a + v, u \in U\} =$$
$$\inf\{\mu(l)| \ a \leq l, l \in L\}.$$

For a Lebesgue-type convergence theorem we require a subset of special integrals that correspond to the point evaluations in classical integration theory. In this vein, for a neighborhood $v \in V$ we define the *integral boundary relative to v* to be the set Δv of all integrals δ on P such that

$\delta(v) < +\infty$, satisfying the following property: If for any two integrals μ_1, μ_2 on P we have

$$\delta(v) = (\mu_1 + \mu_2)(v) \quad \text{and}$$
$$\delta(u) \leq (\mu_1 + \mu_2)(u) \text{ for all } u \in U$$

then there are $\lambda_1, \lambda_2 \geq 0$ such that $\mu_1 \sim \lambda_1 \delta$ and $\mu_2 \sim \lambda_2 \delta$. For a neighborhood $v \in V$ we shall say that a subset A of P is *uniformly v-dominated* if there is $\rho \geq 0$ such that $a \leq \rho v$ for all $a \in A$.

We formulate the main convergence result (Theorem 4.3 in [11]) which is modeled after the Bishop de-Leeuw theorem from Choquet theory.

11.3 Theorem. *Let μ be an integral on the integration cone (P, L, U). For a neighborhood $v \in V$ let $(a_n)_{n \in \mathbb{N}}$ be a uniformly v-dominated sequence of μ-integrable elements in P. If*

$$\lim \sup_{n \in \mathbb{N}} \delta(a_n) \leq \delta(v)$$

for all $\delta \in \Delta v$, then

$$\lim \sup_{n \in \mathbb{N}} \mu(a_n) \leq \mu(v).$$

For detailed arguments in the following examples we refer to Examples 1.1 and 3.13 in [10].

11.4 Examples. (a) This example models topological integration theory on a compact Hausdorff space X as presented in [5]: Let P be the cone of all bounded below $\bar{\mathbb{R}}$-valued functions on X, endowed with the pointwise algebraic operations and order, and let V consist of all strictly positive constant functions on X. Then (P, V) is a full locally convex cone. We choose for L the subcone of all $\bar{\mathbb{R}}$-valued lower semicontinuous functions and for U all real-valued upper semicontinuous functions in P. As required, $V \subset L$, and all functions in U are bounded. For an integral $\mu \in P^*$, condition 11.1 (b) implies that

$$\mu(l) = \sup\{\mu(c)| \ c \leq l, c \in C(X)\}$$
$$\text{for all } l \in L$$

and

$$\mu(u) = \inf\{\mu(c)| \ u \leq c, c \in C(X)\}$$
$$\text{for all } u \in U.$$

Following Theorem 11.2, a function $f \in P$ is μ-integrable if and only if

$$\sup\{\mu(u)| \ u \leq f, u \in U\}$$
$$= \inf\{\mu(l)| \ f \leq l, l \in L\}.$$

The integrals of this theory, therefore are the positive Radon measures on the compact space X, and the above notion of integrability coincides with the usual one (see [5], IV.4, Théorème 3), except for the fact that we allow integrals to take the value $+\infty$. Theorem 11.1 (a) implies that every positive linear functional on $C(X)$ permits an extension to a positive Radon measure on X, which is the result of the Riesz Representation Theorem. For a neighborhood $v \in V$ the integral boundary relative to v consists of positive multiples of point evaluations in X. Thus Theorem 11.3 yields Lebesgue's convergence theorem. The adaptation of this example for a locally compact Hausdorff space X is rather more technical and may be found in [10], Example 3.13 (c).

(b) Let X be a compact convex subset of a locally convex Hausdorff space, and let (P, V) be as in (a). We choose the subcone of all $\bar{\mathbb{R}}$-valued lower semicontinuous concave functions for L and the real-valued upper semicontinuous convex functions for U. As the elements of the dual cone P^* of P when restricted to $C(X)$ are positive Radon measures on X, our integrals on P are just the usual maximal representation measures from classical Choquet theory. The μ-integrable elements of P include all continuous functions on X. Theorem 11.2 yields Mokobodzki's characterization of maximal measures in Choquet theory (Proposition 1.4.5 in [1]). The subspace $U \cap L$ consists of the continuous affine functions on X, and Theorem 11.1 (a) implies that every positive linear functional on this subspace (i.e. a positive multiple of a point evaluation on X) may be represented by such a maximal measure. Moreover, for every neighborhood $v \in V$, the integral boundary Δv consists of positive multiples of evaluations in the extreme points of

X, hence Theorem 11.3 recovers the Bishop de-Leeuw theorem from classical Choquet theory about the support of maximal measures.

(c) Let $(P = Conv(E), V)$ be the full locally convex cone introduced in Example 3.1 (c). We choose $L = P$ and for U the subcone of P of all singleton subsets of the space E. Following Theorem 11.2 every integral μ on P is already determined by its values on the subcone U, that is by a monotone continuous linear functional μ_0 in the usual dual E' of the locally convex ordered topological vector space E; that is

$$\mu(A) = \sup\{\mu_0(a) \mid a \in A\}$$

for every $A \in P$. This describes a one-to-one correspondence between the monotone functionals in E' and the integrals on P. For a neighborhood $v \in V$ the integral boundary relative to v consists of those integrals on P that are induced by positive multiples of the extreme points of the usual polar of v in E'.

References

[1] E. M. Alfsen, "Compact convex sets and boundary integrals," *Ergebnisse der Mathematik und ihrer Grenzgebiete*, **1971**, vol. 57, Springer Verlag, Heidelberg-Berlin-New York.

[2] F. Altomare and M. Campiti, "Korovkin type approximation theory and its applications," *Gruyter Studies in Mathematics*, **1994**, vol. 17, Walter de Gruyter, Berlin-New York.

[3] B. Anger and J. Lembcke, "Hahn-Banach type theorems for hypolinear functionals," *Math. Ann.*, **1974**, 209, 127-151.

[4] H. Bauer and K. Donner, "Korovkin approximation in $C_0(X)$," *Math. Ann.*, **1978**, 236, 225-237.

[5] N. Bourbaki, *Éléments de Mathématique*, Fascicule III, Livre VI, Intégration, **1965**, Hermann, Paris.

[6] B. Fuchssteiner and W. Lusky, "Convex cones," North Holland Math. Studies, **1981**, vol.56.

[7] K. Keimel and W. Roth, "Ordered cones and approximation," Lecture Notes in Mathematics, 1517, **1992**, Springer Verlag, Heidelberg-Berlin-New York.

[8] P.P. Korovkin, "Linear operators and approximation theory," Russian Monographs and Texts on Advanced Mathematics, vol. III, **1960**, Gordon and Breach, New York.

[9] L. Nachbin, *Topology and Order*, **1965**, Van Nostrand, Princeton.

[10] W. Roth, "Integral type linear functionals on ordered cones," *Trans. Amer. Math. Soc.*, **1996**, vol. 348, no. 12, 5065-5085.

[11] W. Roth, "Real and complex linear extensions for locally convex cones," *Journal of Functional Analysis*, **1997**, vol. 151, no. 2, 437-454.

[12] W. Roth, "A uniform boundedness theorem for locally convex cones," *Proc. Amer. Math. Soc.*, **1998**, vol. 126, no. 7, 83-89.

[13] W. Roth, "Hahn-Banach type theorems for locally convex cones," *Journal of the Australian Math. Soc.* (Series A) 68, **2000** no. 1, 104-125.

[14] W. Roth, "Inner products on ordered cones," *New Zealand Journal of Mathematics*, **2001**, 30, 157-175.

[15] W. Roth, "Separation properties for locally convex cones," *Journal of Convex Analysis*, **2002**, vol. 9, No. 1, 301-307.

[16] W. Roth, "Boundedness and connectedness components for locally convex cones," *New Zealand Journal of Mathematics*, **2005**, 34, 143-158.

[17] W. Roth, "Operator-valued measures and integrals for cone-valued functions," Lecture Notes in Mathematics, vol. 1964, **2009**, Springer Verlag, Heidelberg-Berlin-New York.

[18] H.H. Schäfer, "Topological vector spaces," **1980**, Springer Verlag, Heidelberg-Berlin-New York.

Adsorption characteristics of pomelo skin toward toxic Brilliant Green dye

Muhammad Khairud Dahri, Muhammad Raziq Rahimi Kooh and Linda B. L. Lim[*]

Chemical Sciences, Faculty of Science, Universiti Brunei Darussalam, Jalan Tungku Link, Gadong, BE 1410, Brunei Darussalam

[*]corresponding author email: linda.lim@ubd.edu.bn

Abstract

Pomelo skin was investigated for its adsorption ability toward Brilliant Green dye. Experimental conditions used in this study were 2 h contact time; PS dosage = 0.04 g and ambient temperature. No adjustment of medium pH was required throughout the study and pomelo skin was able to maintain good adsorption capability under various ionic strengths. Of the three isotherm models (Langmuir, Freundlich and Sips) used to fit the experimental data, the adsorption was best described by the Freundlich model, indicating multi-layer adsorption onto a heterogeneous surface, followed by the Sips and the Langmuir models. Adsorption was exothermic in nature and kinetics was best described by the pseudo second order and pore diffusion was found to be not the rate determining step. Successful regeneration and reusability of spent pomelo skin, coupled with high maximum adsorption capacity (q_{max}) of 325 mg/g (Langmuir) and 400 mg/g (Sips) at 25 °C compared with many reported adsorbents, make pomelo skin a potential candidate to be considered in real life application of wastewater remediation.

Index Terms: pomelo skin, low-cost adsorbent, adsorption isotherm, brilliant green dye

1. Introduction

Industralisation and exponential growth in the world's population have resulted in severe environmental pollution, thereby causing global concern. Irresponsible dumping of wastes into the water systems has caused severe damage to aquatic organisms and plants. The past couple of decades have seen the emergence of various adsorbents for the remediation of wastewater. These adsorbents ranged from industrial[1-3] to agricultural wastes,[4-8] synthetic materials[9] to natural biosorbents,[10-13] as well as surface modified adsorbents[14] and many others[15, 16].

Brilliant green (BG) dye, also known as malachite green G, belongs to the triarylmethane dyes. It is known to be toxic when ingested and can cause vomiting.[17] This dye has also been reported to cause corneal opacification when 1% of this dye solution came in contact with the eye.[18]

In this study, we report the use of pomelo skin (PS) as a low-cost natural adsorbent for the removal of BG. The skin of the fruit is inedible and often discarded as waste. As such, PS can be obtained easily and at abundance making it an ideal sample to be used as an adsorbent. Reports have shown that PS has been successfully utilised as an adsorbent for the removal of heavy metals such as Cu(II),[19] Pb(II),[20] Cd(II),[21] as well as dyes such as methylene blue,[22] reactive blue 114,[23] and acid blue 15.[24] PS has also been reported to clean up oil spill from simulated seawater.[25] These studies along with the fact that PS is easily available and abundant make it a good low-cost adsorbent. To the best of our knowledge, the use of PS for the removal of BG has not been investigated.

2. Experimental

2.1. Sample preparation and chemicals

Pomelo fruits were purchased from the supermarket and had their skin separated from the

flesh. The skin was dried in an oven at 70 °C until constant mass was obtained. The dried skin was then blended using normal household blender and sieved to obtain particle size of 355-850 μm and was stored in airtight plastic bag.

Brilliant green dye, IUPAC name 4-([4-(diethylamino)phenyl](phenyl)methylene)-N,N-diethyl-2,5-cyclohexadien-1-iminium hydrogen sulfate (molecular formula $C_{27}H_{34}N_2O_4S$ and $M_r =$ 483 g/mol), was purchased from Sigma-Aldrich. Sodium hydroxide (Univar) and nitric acid (AnalaR) were diluted and were used in adjusting the solution's pH. Stock solution of potassium nitrate (Sigma-Aldrich) was prepared and diluted to different concentrations. All reagents were used without further purification and distilled water was used throughout the experiment.

2.2. Experimental setup
The experiment was done using batch experiment method. PS was mixed with BG solution and agitated using Stuart orbital shaker at 250 rpm for predetermined time. The filtrate was collected and analysed using UV–visible (UV-vis) Jenway 6320D spectrophotometer at wavelength 624 nm. The adsorption capacity of PS, q_e (mg/g) and the percentage removal are calculated as follow:

$$q_e (\text{mg/g}) = \frac{(C_i - C_e)V}{m} \tag{1}$$

$$\text{Removal} (\%) = \frac{(C_i - C_e) \times 100\ \%}{C_i} \tag{2}$$

where C_i is the dye concentration initially (mg/L), C_e is the filtrate dye concentration (mg/L), V is the dye volume used (L) and m is the mass of PS (g).

2.2.1. Effect of contact time
PS (0.4 g) was weighed into 13 conical flasks and 100 mg/L BG solution (20.0 mL) was added into each of the flasks. The mixtures were then agitated at 250 rpm at room temperature (25 °C). One flask was taken at the interval of 5, 10, 15, 20, 25, 30, 60, 90, 120, 150, 180, 210 and 240 min. The filtrate was then analysed using UV-vis spectrophotometer.

2.2.2. pH effect
The pH of 10 mg/L BG solution (20.0 mL) was adjusted to 4, 6, 8 and 10 using NaOH and HNO_3 and measured using Thermo-Scientific pH meter. Each of the pH adjusted BG solution was then mixed with PS (0.4 g) and agitated at 250 rpm for 2 h. The filtrate was collected and analysed using UV-vis spectrophotometer.

2.2.3. Point of zero charge
0.1 mol/L KNO_3 solutions (20.0 mL) were prepared and their pH was adjusted to 2, 4, 6, 8 and 10. These solutions were then mixed with PS (0.4 g) and agitated at 250 rpm for 24 h. The final pH was measured and the plot of ΔpH (final pH - initial pH) vs initial pH was used for the determination of PS's point of zero charge.

2.2.4. Effect of ionic strength
10 mg/L BG solutions (20.0 mL) containing various concentration of KNO_3 (0.01, 0.1, 0.2, 0.4, 0.6 and 0.8 mol/L) solutions were prepared and mixed with PS (0.4 g). These mixtures were then agitated at 250 rpm for 2 h and the dye content was analysed.

2.2.5. Adsorption isotherm
A series of BG solution (20.0 mL) ranging from 10 – 1000 mg/L was prepared and mixed with PS (0.4 g). The mixtures were agitated for 2 h at 250 rpm before the filtrate was collected and analysed.

2.2.6. Thermodynamic studies
PS (0.4 g) was mixed with 50 mg/L BG solution and the mixture was agitated at 25, 40, 50, 60 and 70 °C. The filtrate was collected and analysed.

2.2.7. Regeneration
Spent PS was collected from the agitation of PS with 100 mg/L BG solution and washed with distilled water to remove excess dye. It was then divided into three parts where one part was mixed with distilled water (50.0 mL); the other was mixed with 0.1 mol/L HNO_3 (50.0 mL) and the final part was mixed with 0.1 mol/L NaOH (50.0 mL). These mixtures were agitated for 2 h at 250 rpm before they were filtered and further washed using distilled water until the filtrates were near neutral. The treated PSs were then dried in an oven

overnight before mixing them with fresh 100 mg/L BG and the dye content was analysed using UV-vis spectrophotometer. This is considered as one cycle and the regeneration experiment was done for 5 cycles.

3. Results and Discussion
3.1. Adsorption parameters
Parameters such as contact time for the adsorbent-adsorbate system to reach equilibrium, effects of medium pH and ionic strength on BG removal were investigated. As shown in *Figure 1*, rapid removal of BG was observed during the first half an hour which then gradually slowed down to a plateau when full equilibrium is reached. This observation can be attributed to initial presence of a large number of active vacant sites on the surface of PS which allowed rapid adsorption of BG. However, over time as these sites began to be filled by dye molecules, the rate gradually decreased and eventually reached equilibrium. In this study, the best contact time was taken as 2 hours and all subsequent experiments were carried out using this contact time, unless otherwise stated.
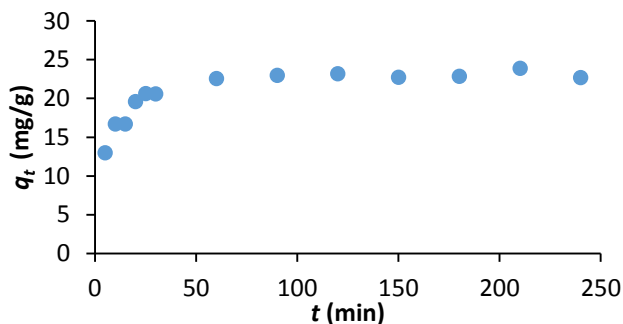
Figure 1. Effect of contact time for the removal of BG onto PS [dye concentration =100 mg/L; dye volume = 20.0 mL; mass of PS = 0.04 g; ambient pH; stirring rate = 250 rpm and room temperature]

When the effect of medium pH was tested over the range of pH 4 to 10, the adsorbent showed a reduction of 40% BG removal at high pH, while at pH 4 a slight reduction of 8% was observed (*Figure 2*).

The point of zero charge (pH$_{pzc}$) of PS was found to be at pH 3.53, as shown in *Figure 3*. Any pH > pH$_{pzc}$ will result in deprotonation of the surface
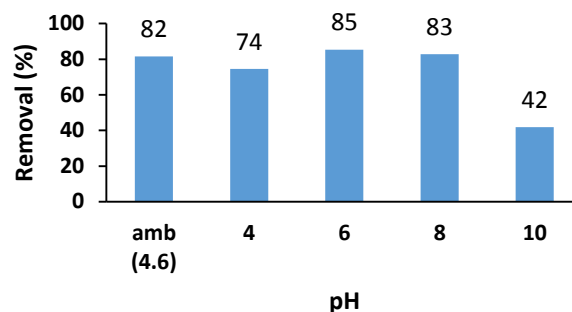
Figure 2. Effect of medium pH on the adsorption of BG onto PS [contact time = 2 h; dye concentration =10 mg/L; dye volume = 20.0 mL; mass of PS = 0.04 g; stirring rate = 250 rpm and room temperature].
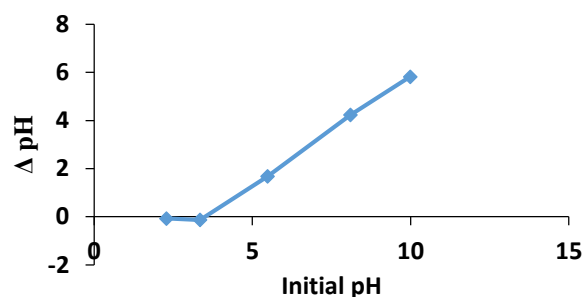
Figure 3. Point of zero charge of PS [contact time = 24 h; salt solution volume = 20.0 mL; mass of PS =0.04 g; stirring rate =250 rpm and room temperature].

functional groups of PS, causing the surface to be predominantly negative in charge. Since BG is a cationic dye, this will enhance attraction between the dye molecules and the negatively charged surface, resulting in higher removal of BG as shown by the increase in percentage removal from pH 4 to 6. From pH 8 to 10, a drastic reduction was observed. Cheing et al[26] reported that BG is unstable at pH < 3 and pH > 10. From their study, it was also shown that the absorbance of BG was greatly reduced at pH 10 due to alkaline fading,[27] which could explain the 40% reduction observed in this study. While at low pH, the formation of BGH^{2+} also causes the fading of the dye colour intensity. Further, when pH < pH$_{PZC}$, both the surface of PS and BG will be positively charged due to protonation taking place and this results in an electrostatic repulsion between the adsorbate and the adsorbent. Hence, a decrease in the dye removal. Similar finding was reported for kaolin.[28]

Since the removal of BG by PS was 82% at untreated (ambient) pH, which was comparable to that of pH 6 with the highest observed percentage removal of 85%, no medium pH adjustment was deemed necessary and the ambient pH was used throughout this study.

The effect on ionic strength using 0 to 0.8 mol/L KNO_3 showed that PS was resilient to change in salt concentration (**Figure 4**). It was able to maintain good adsorption of BG over the range studied with only 9% reduction being observed at 0.1 mol/L KNO_3. Many reported adsorbents such as duckweed,[29] breadnut peel,[29] leaf[11] and stem axis of *Artocarpus odoratissimus*,[30] showed drastic reduction of more than 30% in adsorption capacity towards adsorbates with increasing salt concentration. Since salts are usually present in wastewater, the fact that PS was still able to maintain good adsorption capacity indicates its potential as an adsorbent in wastewater remediation.
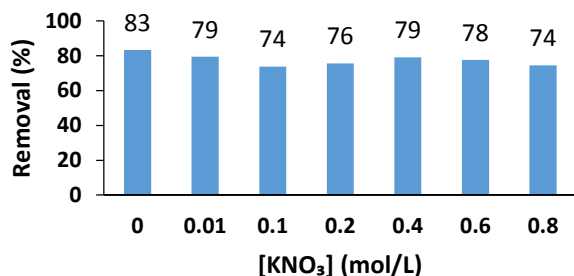
Figure 4. Effect of ionic strength on the adsorption of BG onto PS at different [KNO_3] PS [contact time = 2 h; dye concentration =100 mg/L; dye volume = 20.0 mL; mass of PS =0.04 g; ambient pH; stirring rate =250 rpm and room temperature].

3.2. Adsorption isotherm of BG onto PS
Adsorption isotherm was carried out for BG dye concentrations ranging from $0 - 1000$ mg L^{-1} and the experimental data was fitted to the Langmuir,[31] Freundlich[32] and Sips[33] isotherm models, whose linearised equations are shown below:

Langmuir: $$\frac{C_e}{q_e} = \frac{1}{b \, q_{max}} + \frac{C_e}{q_{max}} \qquad (3)$$

Freundlich: $$\ln q_e = \frac{1}{n_F} \ln C_e + \ln K_F \qquad (4)$$

Sips: $$\ln\left(\frac{q_e}{q_{max} - q_e}\right) = \frac{1}{K_{LF}} \ln C_e + \ln K_S \qquad (5)$$

where q_{max} (mg/g) is the maximum adsorption capacity, K_L (L/mg) is the Langmuir constant, K_F (mg/g(Lmg^{-1})$^{1/n}$) is the adsorption capacity, n_F value (between 1 and 10) indicates favourability of the adsorption process, K_S (L/g) is the Sips constant and K_{LF} is the exponent.

The Langmuir model assumes a monolayer adsorption where once the active sites are being occupied by the dye molecules, no more adsorption will take place. The Freundlich model, on the other hand, assumes that even though the active sites have been occupied by dye molecules, more adsorption is still possible through multi-layer adsorption. Unlike the Langmuir and the Freundlich models which are two parameter models, the Sips model is a three parameter model which is often known as the Langmuir-Freundlich model. As the name implies, the Sips is a combination of the Langmuir and Freundlich models where at high adsorbate concentration, it follows Langmuir model and follows Freundlich model at low adsorbate concentration.[34] Based on the coefficient of determination (R^2), as shown in **Table 1**, the order of best fit model for the adsorption of BG onto PS is Freundlich > Sips > Langmuir. The adsorption is also favorable as indicated by $n_F > 1$, which is further confirmed by $1/n$ lying between 0 and 1 showing adsorption is favorable and heterogeneous. The suitability of the isotherm models was also analysed using two error functions *i.e.* Marquart's percent standard deviation (MPSD) (**Equation 6**) and Chi-test (χ^2) (**Equation 7**). Relying on just the R^2 can be inaccurate as there have been many reports where isotherm models with high R^2 values gave high errors as well. From the error values as shown in **Table 1**, it can be seen that the Freundlich model gave the lowest values, followed by the Sips model, with the Langmuir model giving the highest error values.

MPSD: $$100 \sqrt{\frac{1}{n-2} \sum_{i=1}^{n} (q_{e,meas} - q_{e,calc})^2} \qquad (6)$$

$$\chi^2 : \sum_{i=1}^{m} \frac{(q_{e,meas} - q_{e,calc})^2}{q_{e,meas}} \qquad (7)$$

where $q_{e,meas}$ is the experimental value while $q_{e,calc}$ is the calculated value and n is the number of data in the experiment. Smaller values of these error analysis indicates the better curve fitting.[35]

Table 1. Adsorption isotherm models and their parameters

Models	Parameters	Values
Langmuir	q_{max} (mg/g)	324.98
	b (L/mg)	0.003
	R^2	0.835
	MPSD	20.35
	χ^2	26.21
Freundlich	$K_F[(mg/g)(L/mg)^{1/n}]$	2.988
	n_F	1.472
	$1/n$	0.679
	R^2	0.993
	MPSD	11.55
	χ^2	11.95
Sips	q_{max} (mg/g)	400.00
	K_S (L/g)	0.005
	K_{LF}	1.17
	R^2	0.971
	MPSD	18.78
	χ^2	21.37

The maximum adsorption capacity (q_{max}) of PS for adsorption of BG is 400 mg/g and 325 mg/g based on the Sips and Langmuir isotherm models, respectively. When these values were compared to other reported adsorbents for the removal of BG, PS is indeed a very good low-cost adsorbent as shown by its high q_{max} value in **Table 2**.

Table 2. Maximum adsorption capacity of BG by various adsorbents.

Adsorbent	q_{max} (mg/g)	References
Pomelo skin	400	This work
Peat	266	26
Cempedak durian peel	98	36
Red clay	125	37
Rice straw biochar	111	38
Luffa cylindrical sponge	18	39
Neem leaves	134	40

3.3. Thermodynamics and kinetics studies on the adsorption of BG onto PS

Thermodynamics studies were carried out at temperatures ranging from 298 – 343 K and the data were fitted into Van't Hoff equation shown below:

$$\Delta G° = -RT \ln K \tag{8}$$

$$K = \frac{C_S}{C_e} \tag{9}$$

$$\Delta G° = \Delta H° - T\Delta S° \tag{10}$$

Inserting **Equation 8** into **Equation 10**:

$$\ln K = \frac{\Delta S°}{R} - \frac{\Delta H°}{RT} \tag{11}$$

where K is the distribution coefficient for adsorption, C_S is the dye concentration adsorbed on PS (mg/L), R is the gas constant (J/mol K) and T is the absolute temperature (K).

In **Table 3**, it was found that the amount of BG adsorbed decreases as the temperature is raised, indicating an exothermic nature of the adsorption process. This was confirmed by the negative enthalpy ($\Delta H°$) of -16.42 kJ/mol. Negative entropy ($\Delta S°$) and decreasing negativity of the Gibbs energy ($\Delta G°$) point to the adsorption process showing less freedom of movement of molecules and less spontaneous as the temperature increases.

Table 3. Thermodynamics parameters for the adsorption on BG onto PS.

Temp (K)	$\Delta G°$ (kJ/mol)	$\Delta H°$ (kJ/mol)	$\Delta S°$ (J/mol K)	q_e (mg/g)
298	-1.999			18.41
313	-1.407			16.90
323	-1.038	-16.418	-48.089	15.84
343	0.196			12.89

Kinetics study was carried out using 100 mg/L BG at room temperature. The experimental data was fitted using the Lagergren first order[41] and pseudo second order[42] models, whose equations are as follow:

Lagergren first order:
$$\log (q_{e,expt} - q_t) = \log q_{e,expt} - \frac{t}{2.303} k_1 \tag{12}$$

Pseudo second order:

$$\frac{t}{q_t} = \frac{1}{q_{e,expt}^2 k_2} + \frac{t}{q_{e,expt}} \qquad (13)$$

where t is the time shaken (min), q_t is the adsorbate adsorbed per gram of adsorbent (mg/g) at time t, k_1 is the Lagergren first order rate constant (1/min), k_2 is pseudo second order rate constant (g/mg min).

From *Figure 5* and *Table 4* the data clearly show that of the two kinetics models used, the Lagergren first order model even though has a high R^2 is not the suitable model since the experimental $q_{e,expt}$ of 23.91 mg/g is far from the calculated $q_{e,calc}$ of 8.42 mg/g. On the other hand, the pseudo second order kinetics gave a higher R^2 which is very close to unity. Its $q_{e,calc}$ (23.57 mg/g) is also in good agreement with the $q_{e,expt}$. Hence, it is concluded that the adsorption of BG onto PS follows the pseudo second order kinetics with rate constant k_2 of 0.011 g/mg min.
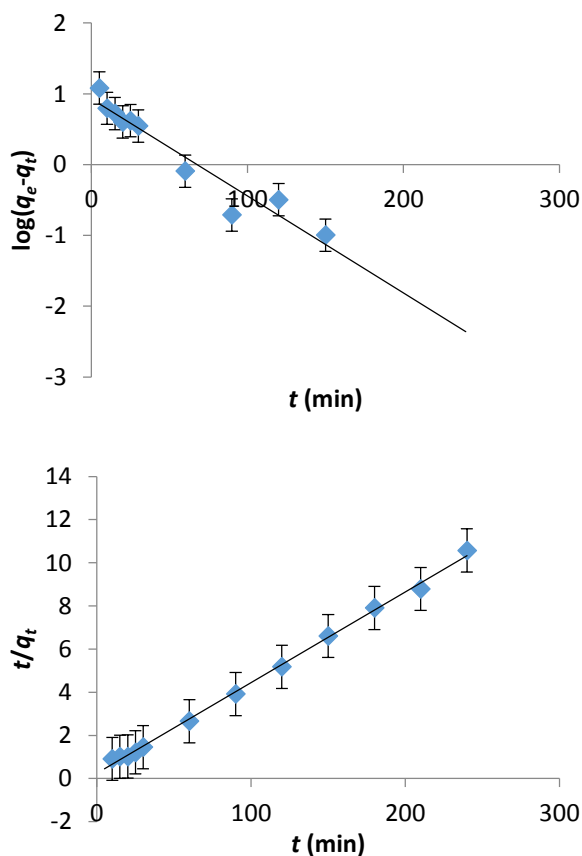
Figure 5. Adsorption kinetics based on the Lagergren first order (top) and the pseudo second order (bottom).

Table 4. Kinetics parameters for the adsorption of BG onto PS.

$q_{e, expt}$ (mg/g)	Lagergren first order		
	$q_{e, calc}$ (mg/g)	k_1 (1/min)	R^2
	8.42	0.032	0.931
	pseudo second order		
23.91	$q_{e, calc}$ (mg/g)	k_2 (g/mg min)	R^2
	23.57	0.011	0.997
	Intra-particle diffusion		
	k_3(mg/g min$^{1/2}$)	C	R^2
Region 1	2.396	8.20	0.934
Region 2	0.055	22.35	0.115

Further investigation of the adsorption kinetics using the Weber Morris intra-particle diffusion[43] (*Equation 14*), showed that pore diffusion was not the rate determining step since the plot did not pass through the origin as shown in *Figure 6*.

Weber Morris intra-particle diffusion:

$$q_t = k_3\, t^{1/2} + C \qquad (14)$$

K_3 is the intraparticle diffusion rate constant (mmol/g min$^{1/2}$) and C is the slope that represents the thickness of the boundary layer.
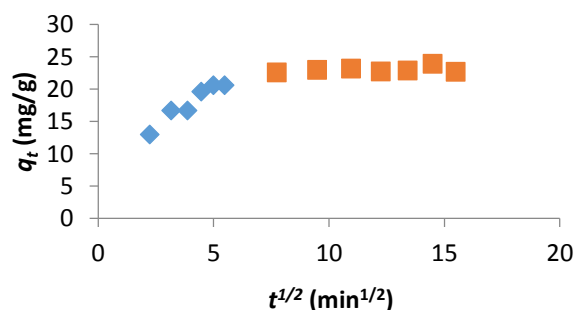
Figure 6. Adsorption kinetics based on the Weber Morris intra-particle diffusion model.

3.4. Regeneration of PS
In order to test the reusability of spent-PS, regeneration studies were carried out using three methods of washing after each adsorption i.e. washing with distilled water, acid and base. Under the experimental conditions used, all three methods gave higher removal of BG even after 4 consecutive cycles (*Figure 7*). However, a

reduction of about 20% in removal of dye was observed for washing with water in the 5th cycle compared to the spent-PS. Nevertheless both acid and base wash were able to maintain high removal of BG even at the 5th cycle, with the base being a more superior method of treatment. The reason could be that base treatment is known to remove the surface fats and waxes[44] thereby exposing the functional groups on the surface which in turn will enhance adsorption with the dye molecules.
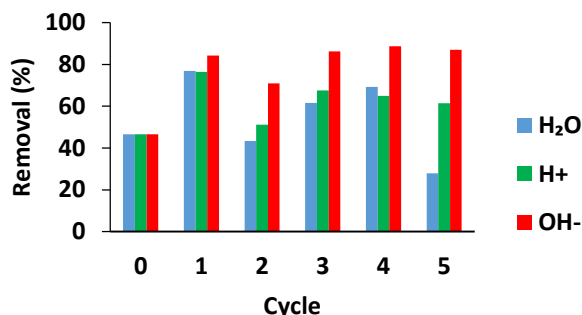
Figure 7. Regeneration of spent PS using water, base and acid treatment PS [contact time = 2 h; dye concentration =100 mg/L; dye volume = 20.0 mL; mass of PS =0.04 g; ambient pH; stirring rate =250 rpm and room temperature].

4. Conclusion

This study has shown that pomelo skin, which is often discarded as waste and of no economic value, can be converted to a valuable adsorbent for the removal of Brilliant green dye. Fast contact time to reach equilibrium, resilient to ionic strength, high maximum adsorption capacity together with the ability to regenerate and reuse the spent pomelo skin make it a potential and attractive low-cost candidate as an adsorbent in real life application for the treatment of wastewater.

Acknowledgements

References

[1] A. Jain, V. Gupta and A. Bhatnagar, *J. Hazard. Mater.*, **2003**, 31-42.

[2] A. Bhatnagar and A. Jain, *J. Colloid Interface Sci.*, **2005**, 49-55.

[3] D. Sarkar, S. K. Das, P. Mukherjee and A. Bandyopadhyay, *Clean–Soil, Air, Water*, **2010**, 764-770.

[4] M. R. R. Kooh, L. B. L. Lim, L. H. Lim and M. K. Dahri, *Environ. Monit. Assess.*, **2016**, 1-15.

[5] M. R. R. Kooh, M. K. Dahri, L. B. L. Lim and L. H. Lim, *Arab. J. Sci. Eng.*, **2016**, 2453–2464.

[6] A. K. Chowdhury, A. D. Sarkar and A. Bandyopadhyay, *Clean–Soil, Air, Water*, **2009**, 581-591.

[7] R. Lafi, A. ben Fradj, A. Hafiane and B. Hameed, *Korean J. Chem. Eng.*, **2014**, 2198-2206.

[8] A. Demirbas, *J. Hazard. Mater.*, **2008**, 220-229.

[9] S. H. Lin and R. S. Juang, *J. Environ. Manag.*, **2009**, 1336-1349.

[10] L. B. L. Lim, N. Priyantha, H. H. Cheng and N. A. Hazirah, *Scientia Bruneiana*, **2016**, 99-106.

[11] M. R. R. Kooh, M. K. Dahri, L. B. L. Lim, L. H. Lim and O. A. Malik, *Environ. Earth Sci.*, **2016**, 783.

[12] L. B. L. Lim, N. Priyantha, T. Zehra, C. W. Then and C. M. Chan, *Desalin. Water Treat.*, **2016**, 10246-10260.

[13] M. Dakiky, M. Khamis, A. Manassra and M. Mer'eb, *Adv. Environ. Res.*, **2002**, 533-540.

[14] K. G. Bhattacharyya and S. S. Gupta, *Adv. Colloid Interface Sci.*, **2008**, 114-131.

[15] K. Vijayaraghavan, M. Sathishkumar and R. Balasubramanian, *Ind. Eng. Chem. Res.*, **2010**, 4405-4411.

[16] K. Vijayaraghavan and U. M. Joshi, *Environ. Eng. Sci.*, **2013**, 67-73.

[17] J. K. Narat, *Annals Surgery*, **1931**, 1007.

[18] W. M. Grant, *Toxicology of the Eye,* Charles C. Thomas Publisher: Springfield, IL. **1986**, 155.

[19] P. Tasaso, *J. Clean Energy Technol.*, **2014**, 154-157.

[20] J. Luo, J.-w. Ge, X.-b. Yang and X.-d. Li, *Food Sci.*, **2010**, 018.

[21] W. Saikaew, P. Kaewsarn and W. Saikaew, *World Acad. Sci. Eng. Technol*, **2009**, 287-291.

[22] B. Hameed, D. Mahmoud and A. Ahmad, *Colloids Surf., A: Physicochem. Eng. Aspects*, **2008**, 78-84.

[23] M. E. Argun, D. Güclü and M. Karatas, *J. Ind. Eng. Chem.*, **2014**, 1079-1084.

[24] K. Foo and B. Hameed, *Chem. Eng. J.*, **2011**, 385-390.

[25] J. Zou, X. Liu, W. Chai, X. Zhang, B. Li, Y. Wang and Y. Ma, *Desalin. Water Treat.*, **2015**, 939-946.

[26] H. I. Chieng, N. Priyantha and L. B. L. Lim, *RSC Adv.*, **2015**, 34603-34615.

[27] O. Olanrewaju, J. Ige, O. Soriyan, O. Grace, O. S. Esan and O. Olanrewaju, *Acta chim. slov.*, **2007**, 370.

[28] B. K. Nandi, A. Goswami and M. K. Purkait, *J. Hazard. Mater.*, **2009**, 387-395.

[29] L. B. L. Lim, N. Priyantha, D. T. B. Tennakoon, H. I. Chieng, M. K. Dahri and M. Suklueng, *Arab. J. Chem.*, **2014**,

[30] M. R. R. Kooh, M. K. Dahri and L. B. L. Lim, *Appl. Water Sci.*, **2016**, 1-9.

[31] I. Langmuir, *J. Am. Chem. Soc.*, **1918**, 1361-1403.

[32] H. M. F. Freundlich, *J. Phy. Chem.*, **1906**, 385-470.

[33] R. Sips, *J. Chem. Phys.*, **1948**, 490-495.

[34] K. Y. Foo and B. H. Hameed, *Chem. Eng. J.*, **2010**, 2-10.

[35] S. C. Tsai and K. W. Juang, *J. Radioanal. Nucl. Chem.*, **2000**, 741-746.

[36] M. K. Dahri, L. B. L. Lim and C. C. Mei, *Environ. Monitor. Assess.*, **2015**, 1-13.

[37] M. S. U. Rehman, M. Munir, M. Ashfaq, N. Rashid, M. F. Nazar, M. Danish and J.-I. Han, *Chem. Eng. J.*, **2013**, 54-62.

[38] M. S. U. Rehman, I. Kim, N. Rashid, M. A. Umer, M. Sajid and J.-I. Han, *CLEAN – Soil, Air, Water*, **2016**, 55-62.

[39] O. Segun Esan, O. Nurudeen Abiola, O. Owoyomi, C. Olumuyiwa Aboluwoye and M. Olubunmi Osundiya, *ISRN Phy. Chem.*, **2014**, 12.

[40] K. G. Bhattacharyya and A. Sarma, *Dyes Pigments*, **2003**, 211-222.

[41] S. Lagergren, *K. Sven. Vetensk. akad. Handl.*, **1898**, 1-39.

[42] Y. S. Ho and G. McKay, *Chem. Eng. J.*, **1998**, 115-124.

[43] W. Weber and J. Morris, *J. Sanit. Eng. Div.*, **1963**, 31-60.

[44] S. Chowdhury, R. Mishra, P. Saha and P. Kushwaha, *Desalination*, **2011**, 159-168.

NOTES TO CONTRIBUTORS

Manuscript Submission and Specifications

Scientia Bruneiana is published twice a year. The deadline for submission of manuscripts is **30th June for the end of year edition** and the **31st December for the May edition**.

Manuscripts should be submitted to the Chief Editor, Dr. Abby Tan Chee Hong, Faculty of Science, UBD (abby.tan@ubd.edu.bn), in Microsoft Office Word (.DOCX) format.

Papers will be refereed prior to acceptance. Authors are welcome to suggest potential international referees.

Articles outlining original research findings as well as mini-review articles are welcomed. There are two special categories: "Brief Communications" and "Research Notes". Contributions to either category should be 300 to 1000 words long (no more than 3 pages in length). The "Research Notes" section is earmarked for summaries of the results and outcomes of projects receiving UBD Science Faculty research grants.

Manuscripts should be written in English (British or American). All manuscripts should be in 12pt Times New Roman, **single-spaced**, **single column** and A4 formatted (2cm margins from the edge).

Title page
The first page should include the title of the article, author's names and addresses of the institutions involved in the work. The paper title is only capitalized on proper nouns and the first letter. Latin, scientific genus and species should be italicized. The authors' affiliations are denoted with a superscripted number and the corresponding author denoted with a * at the end of the author's name. Only the corresponding author's email need to be listed.

Example format of the title page:

First record and conservation value of *Periophthalmus malaccensis* Eggert from Borneo

First Author[1], John H. Smith[2,3], Muhamad Ali Abdullah[2] and Siti Nurul Halimah Hj. Ahmad[1]*

[1]Environmental and Life Sciences, Faculty of Science, Universiti Brunei Darussalam, Jalan Tungku Link, Gadong, BE1410, Brunei Darussalam
[2]Department of Chemical Sciences, Faculty of Science, Universiti Brunei Darussalam, Jalan Tungku Link, Gadong, BE1410, Brunei Darussalam
[3]Department, University, Street Address, Postcode, Country

*corresponding author email: first.author@ubd.edu.bn

Abstract Page and Index Terms
The second page of the manuscript should include the abstract (up to 300 words) and index terms (subject heading, or descriptor, in information retrieval, that captures the essence of the topic of a document).

Example format of the abstract and index terms page:

Abstract
The abstract is a self contained description of the work in one paragraph of up to 300 words. It must include no references or foot notes, but it must describe the key points of the work. This should include

a description of the work that was done and why it was it done. It should include brief conclusions and any significant numerical findings such as derived constants or important parameters.

Index Terms: resolution, spectroscopy, microscopy

Main body of text
For original research articles, the main body of text of the manuscript should include the following appropriately numbered sections: **1. Introduction**, **2. Experimental approach**, **3. Results and Discussions** and **4. Conclusion** followed by **Acknowledgements**, **References** and **Appendices** (if necessary).

Each different numbered section may contain italicised subheadings which are numbered appropriately, e.g. *2.1*, *3.1*, etc.

Review articles will obviously not conform to this format. In the case of other submissions where the above format may be unsuitable, you are advised to contact the editor prior to submitting the article.

Reference to figures, tables and equations
The main body of text should not include figures and/or tables, but should refer to figures and tables. If a certain figure or table was not referred to in the main body of text then it will be considered irrelevant and therefore will not be included in the publication. When referring to the figure or table in the text, the words figure and/or table should be bold and italicized e.g. ***Figure 1*** and ***Table 1***. The words "figure" and "table" should be spelled out in full and not abbreviated. For further instructions on figures and tables (including dimensions, colour schemes and formats), please refer to the figures and tables section.

Equations could be displayed in-line or centred by itself, but must be accompanied by a number and individual terms/symbols explained. When When referring to the equation in the text, the word "Equation" should be bold and italicized e.g. ***Equation 1***. The words "Equation" should be spelled out in full and not abbreviated.

Example format of equation:

An example of an equation is shown for ***Equation 1***, Weber Morris intraparticle diffusion:

$$q_t = k_{id}t^{1/2} + C \qquad\qquad (1)$$

and Boyd model (***Equation 2***):

$$F = 1 - \frac{6}{\pi^2}exp(-B_t) \qquad (2)$$

where $F = q_t / q_e$, F is the fraction of solute adsorbed at any time, t and B_t is mathematical function of F.

In-line citation style
The in-line citation should be in the following format (superscripted numbers):

Various studies have been found to link parameter A to parameter B.[1]

Please note that superscripted numbers should go after punctuation. e.g. "Studies show that A is linked to B.[1-5]" and "Even though studies show this,[3,4] there are others that contradicts this.[6-8]"

References
The reference list should only include references cited in the text and should be listed in the references section in the following format:

Journal article
[1] J. H. Surname and J. E. Doe, *Journal*, **Year**, Vol., Pages.

Textbook/Chapter of a book
[2] J. H. Surname and J.E. Doe, Title of Textbook (and Chapter), **Publication Year**, Pages

Dissertation/Thesis
[3] J.H. Surname, Title of Thesis, *PhD/Master's Thesis*, **Year**, University

Webpages/Online Databases
[4] Website/Database name/body: URL (date accessed 01/01/2016)

Figures and Tables

A list of tables, figures and captions should be given at the end of the manuscript after the reference list. These must be appropriately numbered in the order that they appear in the paper. Each table and figure must be adequately discussed and referenced in the text. It is important that you do not include tables and figures in the main body of text of your submitted manuscript.

Sizing

Please keep tables/figures/images/illustrations to have a **maximum width of either 8.4 cm (single column) or 17.5 cm (double column)**, with enough clarity that the images does not appear blurred, skewed or pixelated (unless the pixelation is unavoidable from the raw data collection).

Text

Texts in figures and tables should be 10pt, using either Times New Roman, Arial or Calibri font, with consistent font size and style throughout the manuscript's figures/tables/artwork/images/illustrations. Please ensure that texts do not fall below 8pt size as this will greatly affect readability of said text.

Colour

Colour images are highly encouraged for the on-line issue, however they should be designed such that the information is still obvious in grey-scale too for the print version.

Graphs

Graphs could either be saved as an embedded graph format in DOCX or as an image (JPEG or TIFF). Graphs should have clearly-labelled axes and lines that can be distinguished in both color for on-line and grey-scale for print version. You can use dotted and dashed lines etc, or you can use different data point types when appropriate to discriminate between data sets.

Tables

Tables could either be saved as an embedded table format in DOCX or as an image (JPEG or TIFF), with appropriate captions/titles.

Captions

All figures and tables should be appropriately captioned. The caption should be sufficiently able to explain the figure/table without the reader having to refer to the main text. The words "figure" and/or "table" should be bold. italicized and spelled out fully (not abbreviated), followed by a full stop (also bold and italicized). The rest of the caption should not be bold and italicized (unless it is a scientific genus or species).

Example format for figure/table caption:

Figure 1. *Periophthalmus malaccensis* collected in Sungai Bunga, Brunei (UBDM MBu081013mal); a. freshly dead specimen, lateral view; b. live specimen; c. freshly dead specimen, ventral view, detail (scale bars are 10 mm long).

Manuscripts that do not conform to the above instructions will be returned without review.

CALL FOR PAPERS

Scientia Bruneiana
A Journal of Natural and Applied Sciences

The *Scientia Bruneiana (SciBru)*, a new online and print publication by the Faculty of Science at Universiti Brunei Darussalam, is seeking submissions of original research and review articles in the field of natural and applied sciences. *SciBru* is dedicated to publishing high quality research and reviews. We would appreciate if you, your colleagues and research students can submit papers in forthcoming edition of *SciBru* in all areas of **Natural and Applied Science**.

Submission Guidelines

Authors please refer to submission rules specified in the "/information/authors" section of the *SciBru* website http://scibru.fos.ubd.edu.bn/ for preparation and submission of their papers.

About Universiti Brunei Darussalam (UBD)

UBD was founded in 1985 and is the premier university of Brunei Darussalam.

Since 2009, UBD has transformed from a traditional teaching university into a university that incorporates both teaching and research. Over the past 7 years, the Sciences has played a significant contribution towards drastic outcomes in research and innovation. Among them, researchers have managed to secure substantive internal and external research grants. This has allowed the advancement of the sciences which in turn has led to the establishment of a global connectivity while maintaining regional identity and the nation's needs.

Contact Details

Chief Editor: Abby Tan Chee Hong

Dean, Faculty of Science,
Universiti Brunei Darussalam,
Jalan Tungku Link, BE 1410,
Brunei Darussalam
Email: abby.tan@ubd.edu.bn